UNIVERSITY OF LEICESTER

Graduate School

Cryogenic cycle power turbines optimised by hub contouring

Thesis submitted for the degree of

Doctor of Philosophy

at the University of Leicester

By

Hayder Mahdi Baqer Obaida MSc (Baghdad)

Department of Engineering

University of Leicester

October 2017

Cryogenic cycle power turbines optimised by hub contouring

by

Hayder Mahdi Baqer Obaida MSc (Baghdad)

ABSTRACT

Improvements in stage isentropic efficiency and reductions in stage total pressure loss are sought in a 1.5 stage axial turbine. This is representative of power generation equipment used in thermal power cycles, in a cryogenic plants, and in aeroderivative engines. The performance of cryogenic installations and of power plants can be enhanced by using turbines with a higher isentropic efficiency, by reducing the secondary flow losses.

Secondary flow loss reduction is achieved by designing a non-axisymmetric end-wall for the turbine inlet stator hub. The approach is to use a novel guide groove to direct the pressure side branch of the horseshoe vortex away from the blade suction side, using a novel parametric end-wall hub surface definition. This delays the onset of the passage vortex and reduces its associated loss. The performance of the novel hub profile is compared with that from contouring the hub using representative industry best practice. For this, a three-dimensional steady RANS model with an axisymmetric hub is first validated against reference experimental measurements from RWTH Aachen. A Kriging surrogate model from the Alstom Process and Optimisation Workbench (APOW) is used to optimise the hub surface. Comparative CFD predictions with an optimised non-axisymmetric hub show a decrease in the stage total pressure loss coefficient and an increase in the stage isentropic efficiency at design and off-design. The potential benefits to a representative Liquefied Natural Gas (LNG) cryogenic cycle is assessed by thermodynamic cycle analysis.

A 1.60 % increase in the axial turbine stage isentropic efficiency is predicted by using a hub contoured by the optimised guide groove compared to a 0.19 % increase by using the industry best practice. The higher turbine stage isentropic efficiency is predicted to enhance the performance of the LNG cryogenic plant by a 3.15 % rise in the Coefficient Of Performance.

ACKNOWLEDGEMENTS

The author wishes to express his gratitude to his supervisor, Associate Professor Dr. Aldo Rona, who has given him continuous learning, advice, motivation, guidance and support in the research topics and software during this study. Many thanks are given to the author's second supervisor, Dr. Katrin Leschke, for her support on the mathematical surface generation in the study. The author is grateful to Emeritus Professor. J. Paul Gostelow, for his advice on loss generation and contouring methods for axial turbines, and to Dr. Audrius Bagdanavicius, for his kind help with the Cycle-Tempo software.

The author wises to express his special thanks to his sponsor, the Ministry of Higher Education and Scientific Research of Iraq, and their representative in the United Kingdom, the Iraqi Cultural Attaché – London, and also to Middle Technical University, Engineering Technical - College, Baghdad, for their financial support during the period of study and for offering the PhD scholarship.

The author wishes to thank Dr. N. Z. Ince, Dr. Mark Willetts, and colleagues from the Tools and Methods Integration Group, GE Power, Rugby, for their advice. The author wishes to acknowledge the insightful guidance on OpenFOAM by Prof. Hrvoje Jasak, Wikki UK Ltd. The author used the ALICE2 high performance computing facility at the University of Leicester. Graphical rendering software licenses were originally acquired with EPSRC support on Grant GR/N23745/01. The supply of experimental data for the 1.5 stage axial flow turbine "Aachen Turbine" under license by RWTH Aachen is gratefully acknowledged.

Thanks also are due to my colleagues in the former Thermofluids research group (Ahmed, Ali, Sherzad, Hakim, Fernando, Basil, and Motoyuki), for their support and discussions that made the author's time as a PhD student enjoyable.

Finally, the author thanks his lovely mother, his dear wife, his brothers and sisters, and his lovely daughters for their kind support during this study, which gave a great drive towards its completion. The author dedicates this research to the memory of his father, Consultant Engineer Mahdi Baqer Obaida.

CONTENTS

NOMENCLATURE

Roman symbols

C_{SKE}	Coefficient of secondary kinetic energy	
$C_{p\ loss\ CFD\ exp}$	Stage total pressure loss coefficient from the Computational Fluid Dynamics (CFD) prediction	
$C_{p\ loss\ kriging}$	Stage total pressure loss coefficient from the Kriging surrogate model	
$C_{p\ loss}$	Stage total pressure loss coefficient	
C_r	Turbine rotor chord	mm
C_s	Turbine stator blade chord	mm
C_x	Turbine stator axial chord	mm
d	Stator 1 hub groove width	mm
d_{le}	Groove width at stator 1 blade leading edge	rad
d_{te}	Groove width at stator 1 passage trailing edge	rad
e_1	Axial start position of the Aachen Turbine stator 1 passage leading edge	mm
e_2	Axial start position of the Aachen Turbine stator 1 blade leading edge	
e_3	Axial end position of the Aachen Turbine stator 1 blade trailing edge	
e_4	Axial end position of the Aachen Turbine stator 1 passage trailing edge	
g	Polynomial function of degree four	
h_o	Maximum groove depth position as fraction of groove length	
h	$r - r_{hub}$	
H	Turbine blade span	mm
L_1	Axial distance from the passage leading edge to the first curve	mm

L_2	Axial distance from the passage leading edge to the second guide curve	mm
L_3	Axial distance from the passage leading edge to the third guide curve	mm
LCV_{fuel}	Low calorific value of fuel	kJ kg^{-1}
$\dot{m}_{fuel}$	Fuel mass flow rate	kg s^{-1}
$\dot{m}_g$	Natural gas fuel mass flow rate	kg s^{-1}
M	Polynomial operator	
n	Number of discrete points in pitch	
n_i	Outward normal unit vector	
N	Number of blades	
p	Pressure	Pa
p_{o_1}	Turbine stator 1 inlet total pressure	Pa
p_d	Polynomial degree	
P	Power	kW
P_i	Turbine stator 1 hub surface points	
P_{ij}	Mesh of surface control points	
P_m	Mechanical power	kW
$q_p(x)$	Cubic spline interpolation across corresponding points on the pressure side blade	
$q_s(x)$	Cubic spline interpolation across corresponding points on the suction side blade	
Q_H	Heat output	kW
r	Three-dimensional (3-D) radial coordinate	
r_c	Vortex radius	mm
r_d	Groove radial depth	mm
r_h	Turbine stator 1 hub radius	mm
r_{hg}	Turbine stator 1 hub groove radius	mm
r_{PS_1}	Radial height of pressure side spline control point	mm
r_{PS_2}	Radial height of pressure side spline control point	mm
r_{SS}	Radial height of suction side spline control point	mm
Δr_1	Bezier axisymmetric radius shift	mm

Δr_2	Bezier phase shift	mm
R	Specific gas constant	kJ $kg^{-1}K^{-1}$
R_d	Maximum groove depth	mm
Re_L	Reynolds number	
s	Normalized pitchwise coordinate	
s_b	Pitchwise position of maximum groove depth	mm
Δs	Bezier groove amplitude	mm
S_r	Turbine rotor pitch	mm
S_s	Turbine stator pitch	mm
T_{o_1}	Turbine stator 1 inlet temperature	K
T_g	Natural gas temperature	°C
ΔT_{high}	High temperature difference	K
ΔT_{low}	Low temperature difference	K
u	Normalized axial coordinate	
u_s	Stator 1 normalized axial coordinate	
U	Turbine rotor blade speed	m s^{-1}
U_k	Knot vector	
v	Normalized pitchwise coordinate	
v_a	Inlet axial velocity	m s^{-1}
v_s	Stator 1 normalized pitchwise coordinate	
x	3-D axial coordinate	
x_i	x-coordinate of the i^{th} point	
y_i	y-coordinate of the i^{th} point	
z_i	z-coordinate of the i^{th} point	

Greek symbols

α	Turbine stator absolute yaw flow angle	degrees
α_s	Shape parameter	
β	Turbine rotor absolute yaw flow angle	degrees
β_s	Scale parameter	
ϵ_1	Pitch angle function across the Aachen Turbine stator 1 pressure side blade	
ϵ_2	Pitch angle function across the Aachen Turbine stator 1 suction side blade	

η	Minimum distance	mm
η_i	Isentropic efficiency	
η_{is}	Stage isentropic efficiency	
θ	3D pitchwise coordinate	
θ_i	3-D pitchwise coordinate of the i^{th} point	
ϑ	Number of degrees of freedom	
$\mu(x)$	Pitchwise position of the groove maximum	mm
ξ	Groove path curve	
σ	Hub groove width	mm
ϕ_m	Refrigerant mass flow rate	kg s^{-1}
φ_p	Cubic spline interpolation function across the Aachen Turbine stator 1 pressure side blade	
φ_s	Cubic spline interpolation function across the Aachen Turbine stator 1 suction side blade	
ψ	Relative difference	
Ω_x	x vorticity component	s^{-1}

Acronyms

$C.O.P.$	Coefficient Of Performance
DoE	Design of Experiment
LNG	Liquefied Natural Gas
NG	Natural Gas
PS	Pressure side
SS	Suction side

1. INTRODUCTION

1.1 Motivation

Axial flow turbines are the main workhorses of conventional power generation, which delivers about 80% of the 20 trillion kWh world-wide electricity, and of cryogenic plants as the power driving component. Component-level improvements are therefore timely and relevant towards achieving CO_2 global emission reduction targets. In 2009, the UK used 378 TWh of electricity, 43% produced by firing 325 TWh of natural gas, in power stations fitted with axial compressors and turbines. The impact of improving the thermal efficiency of electricity production by natural gas alone by 1% in the UK would give an annual reduction of 600 M tons of CO_2 emissions and a cost saving of £58.2 M, based on a reference gas price of 50 pence/therm.

Improvements the isentropic efficiency of gas turbines used in power generation and in cryogenic plants can be achieved by reducing the secondary flow losses. This is achievable by re-designing the turbine end-walls in such a way to improve the three-dimensional flow through the passage, as well as by other means. These changes can increase the turbine aerodynamic efficiency and reduce the natural gas specific fuel consumption.

Changing the end-wall shape of a turbomachine from an axisymmetric to a non-axisymmetric surface is commonly referred to as end-wall contouring. This thesis investigates the use of a new end-wall surface definition applied to the hub of an axial turbine to reduce the secondary flow losses and improve the stage isentropic efficiency. The effectiveness of this novel end-wall contouring technique is investigated on an axial turbine that is representative of both a power generation turbine and of the type of turbine used for driving axial compressors in a cryogenic plant.

This study evaluates whether cryogenic applications can benefit from the new end-wall design technique. This should be achievable by increasing the stage isentropic efficiency of the type of axial gas turbines used for driving axial compressors in a cryogenic plant. The liquefied natural gas LNG plant is taken as an example for this application. It is investigated how the LNG Coefficient Of Performance can be increased by improving the isentropic efficiency of the axial gas turbine, obtained by end-wall contouring.

1.2 End-Wall Contouring for Axial Turbines

This thesis will highlight a polymorphism in the end wall treatments that other authors have developed by either experiment or through computation. This polymorphism suggests that a flow-structure-based approach to the design of contoured end-walls may benefit the effectiveness of the end-wall treatment through an appropriate parameterisation of the end-wall surface. Such an approach may also lead to some convergence in the surface definition framework.

End wall contouring is typically implemented by prescribing a non-axisymmetric shape to the blade row hub and/or to the casing. The wall shape is typically optimised to give a low stage total pressure loss coefficient. This stage total pressure loss reduction typically leads to an increase in the isentropic efficiency of the stage. The increase in stage isentropic efficiency results from the decrease in the heat generated over the blade pressure side. Generally, heat is generated as a result of friction between the flow and the blade, in the boundary layer, and in the mixing flow, in shear layers. The main source of loss is the entropy increase in the flow, in which the entropy sources are viscous effects in boundary layers, viscous effects in mixing processes, shock waves, and heat transfer across temperature differences (Denton, 1993).

Three-dimensional treatments, typically informed by targeted computational fluid dynamic simulations, are applied. These treatments are particularly relevant for minimizing the loss from secondary flows and improve the stage efficiency. A structured programme of experiments in linear and rotary cascades and in multi-stage test rigs provides essential verification and validation of the aerodynamic performance data, ensuring the robustness of the design, both at the component and at the sub-assembly levels.

The end-wall contouring implemented in this thesis is designed to be applicable to axial flow turbines for cryogenic cycles. Such turbines are used in the production of Liquefied Natural Gas (LNG). The main concept driving the geometry of the non-axisymmetric end-wall is the mitigation of the passage corner vortex by the insertion of a single streamwise channelling groove that confines it.

1.3 Aims and Objectives

The main focus of this thesis is on the reduction of the axial flow turbine stage total pressure loss and on the increase of the stage isentropic efficiency, by contouring the hub wall by a computer-driven geometry definition and optimisation procedure. A fundamental objective is to contextualize the end-wall contouring in the full design process of the axial turbine stator hub and to find out how end-wall surfaces can be parametrised mathematically so that these surfaces merge smoothly with the remainder of the blade passage geometry. This study presents a new design technique for parameterising and optimising the turbine stator hub to reduce the secondary flow losses in a 1.5 stage turbine. The non-axisymmetric turbine stator hub is generated by defining a guide groove running from the blade leading edge to the passage trailing edge, exporting it as a group of Non-Uniform Rational B-Spline (NURBS) surfaces, and by joining these surfaces with the rest of the 1.5 stage turbine. This procedure is then compared with an alternative surface parameterisation method used in industry. This is the procedure also followed in Obaida et al. (2016), Obaida et al. (2017), and in Kadhim et al. (2017).

A rigorous programme of tests is run to validate the new surface definition procedure and to build confidence towards its adoption in industry. A computational fluid dynamic model is developed of the Aachen Turbine (Volmar et al., 1998, Walraevens and Gallus, 1997, Gallus, 1995), which is used as the main validation test case for the current work. The geometry and mesh are generated by ANSYS ICEM CFD. The near-wall region is resolved to a suitable value of y^+ on three computational meshes of progressive spatial resolution. Numerical predictions are generated using the computational fluid dynamics (CFD) solver OpenFoam/2.3.0 and OpenFoam 3.2.-extend version. Flow predictions from the Aachen Turbine model are validated using the low steady three-dimensional (3D) stator experimental data from Aachen (Volmar et al., 1998, Walraevens and Gallus, 1997, Gallus, 1995), by comparing the yaw angle and the meridional, circumferential, and absolute velocity distributions with the RWTH measurements. The axisymmetric cylindrical hub of the validation test case is then replaced by a non-axisymmetric turbine stator hub, defined using a parametric surface that depends on three free parameters. A three-parameter optimisation is implemented of the contoured hub using the Alstom Process and Optimisation Workbench (APOW). APOW generates a Kriging surrogate model of the total pressure loss response of the turbine to the hub shape changes. The Kriging model enables the identification of a combination of surface defining parameters that gives low total pressure loss, therefore

providing an optimised hub shape. The turbine with the optimised stator hub is then tested at off-design conditions to investigate the change in the stage total pressure loss coefficient and in the stage isentropic efficiency for off-design operations.

The predicted isentropic efficiency of the axial turbine with the optimised stator 1 hub is used to study the changes in the Coefficient of Performance of the liquefied natural gas (LNG) plant of Section 1.1, as this improved turbine type is run at different conditions along its operating line. This explores the reductions in the natural gas specific fuel consumption and in CO_2 emissions that can be achieved by using axial turbines fitted with the optimised contoured hub in both power generation and in cryogenic applications.

1.4 Thesis Structure

The thesis contains the following chapters:

1. INTRODUCTION – this chapter.
2. BACKGROUND - this chapter gives a brief introduction to cryogenic cycles, with a schematic showing how the turbine-compressor assembly is used in the cycle. The significance of the axial turbine performance on the Coefficient of Performance of the cycle is highlighted. This motivates studying ways of enhancing the performance of representative axial turbines by reducing their loss. Next, this chapter presents a review of turbomachinery loss generation mechanisms, of the methods for loss reduction by passage shaping, and of published end-wall contour designs, which highlights a lack of applications of axial turbines with contoured hubs to cryogenic processes.

3. PARAMETERISATION OF THE END WALLS - this chapter presents different surface parameterisation approaches for the hub of an axial turbine. The chapter starts by reviewing what is available from the literature. It considers the use of the Bezier curve, of bumps from an array of control points, of a guide curve defined by the Gauss distribution, by the Gamma distribution, by the Chi-square distribution, and by the Beta distribution. All these surface definition methods are then implemented in MATLAB and their advantages and shortcomings are compared.

4. PARAMETERISATION OF THE PASSAGE - this chapter explains the generation of 1.5 stage turbine geometry, the parameterisation of the upstream hub using both the bumps and the guide groove techniques, and the fully parameterised passage description. It then explains how the new parameterised surface is joined to the rest of the 1.5 stage turbine geometry. This surface parameterisation and definition process is implemented in MATLAB.

5. MODELLING END-WALL CONTOURED PASSAGES BY CFD – this process describes how the output from the surface definition process of the previous chapter is used to obtain a numerical model of the flow through a 1.5 stage axial turbine with a contoured hub. This is achieved by generating a numerical mesh in ICEMCFD, exporting the mesh in OpenFOAM, setting the model boundary conditions, solving for the flow, and using the predictions to adapt the contoured hub parameters by workflow automation in APOW. Finally, this chapter explains how Cycle Tempo software can be used gain an insight of the potential of end-wall contoured passages for improving the thermal cycle performance in cryogenic applications.

6. RESULTS AND DISCUSSION – by implementing the procedure described in Chapter five, this chapter presents and discusses a set of results that show the performance of a representative 1.5 stage turbine obtained by contouring the upstream stator hub. It then shows how this performance can be further improved by the automatic computer-based optimisation of the surface-defining parameters of Chapter four. After that, a comparison is made between the optimised results and results obtained from using the surface with bumps hub contouring reference technique from the literature. Chapter six then presents the performance of the 1.5 stage turbine contoured by a guide groove at off-design conditions and quantifies the potential for improving the cycle performance of cryogenic applications, specifically, for a liquefied natural gas cycle.

7. CONCLUSIONS - this chapter reflects upon the outcome of this study, specifically on how an appropriate parametrisation of the non-axisymmetric hub surface, which is compatible with automatic computer-based optimisation, advances the current state of the art in designing axial turbine passages to improve the stage isentropic efficiency. It then considers the implications on the design of turbines for power

generation and for powering cryogenic applications. Finally, it presents some recommendations for further work.

The parameterisation and optimisation software programs including the scripts in MATLAB, ANSYS ICEM CFD reply file, OpenFoam script commands, and running script files inside the APOW were written by the author.

2. BACKGROUND

2.1 Introduction

This chapter provides the relevant background to the work presented in the remainder of the thesis. Three main areas are covered, which are industrial cryogenic cycles, the axial turbines used within these cycles, and methods for improving the turbine stage performance by controlling the hub secondary flows. A brief introduction to the cryogenic cycles is first given, supported by a schematic diagram of a Liquefied Natural Gas plant. The turbine-compressor assembly used in the cryogenic cycle is identified as an improvement opportunity area. A literature review is presented of the loss mechanisms in turbomachines, in which attention is drawn towards the importance of the contribution to loss by secondary flows over the hub. The methods for mitigating such loss are reviewed, based on modifications of the hub passage wall. Three main approaches are presented, which are the suction and blowing technique, the use of a fence, and the end-wall contouring technique. The outcome of this review is the selection of the end-wall contouring approach for reducing the turbine loss at design point operations that in turns aims to increase the Coefficient Of Performance (C.O.P.) of a representative cryogenic cycle.

2.2 Cryogenic Cycles

A cryogenic cycle is defined as the process of extracting heat to reduce the temperature of warm gases below the condensation temperature. This process is used for the production of Liquefied of Natural Gas (LNG), as well as in other cryogenic applications. Improving the LNG process is the target application of the current research. According to both Mokhatab and Wood (2007) and Mokhatab et al. (2013), three main refrigeration cycles are used for the liquefaction of natural gas. These are the optimised cascade cycle, the mixed-refrigerant cycle, and the turbo-expander cycle. More details on all three cycle types are given in in Remeljej and Hoadley (2006), Mokhatab and Wood (2007), Meher-Homji et al. (2008), Bukholdin et al. (2007), Lin et al. (2010), Alabdulkarem et al. (2011), Mafi et al. (2014), and Taher and Meher-Homji (2016). The LNG refrigeration cycle used in this thesis is the optimised cascade cycle. The specific optimised cascade cycle that is studied herein was developed by Conoco-Philips (Mokhatab et al., 2013). The schematic diagram of the Conoco-Philips Optimised cascade cycle is shown in Figure 2-1. This cascade cycle consists of three main refrigeration cycles, which are the Propane refrigeration cycle, the Ethylene refrigeration cycle, and the Methane refrigeration cycle. Each refrigeration cycle compressor

is driven by a separate gas turbine. According to Meher-Homji et al. (2008), the coefficient of performance of the complete LNG cycle is dependent on two main factors. The first one is the efficiency of its heat exchangers. The second one is the isentropic efficiency of its gas turbines. Therefore, improving the turbine that drives the LNG cycles increases the LNG coefficient of performance. The increase in isentropic thermal efficiency of the LNG turbine can be achieved by reducing the turbine secondary flow losses. This thesis aims to reduce the secondary flow losses by end-wall contouring, drawing from the turbine hub wall design techniques that are reviewed in the next sections.

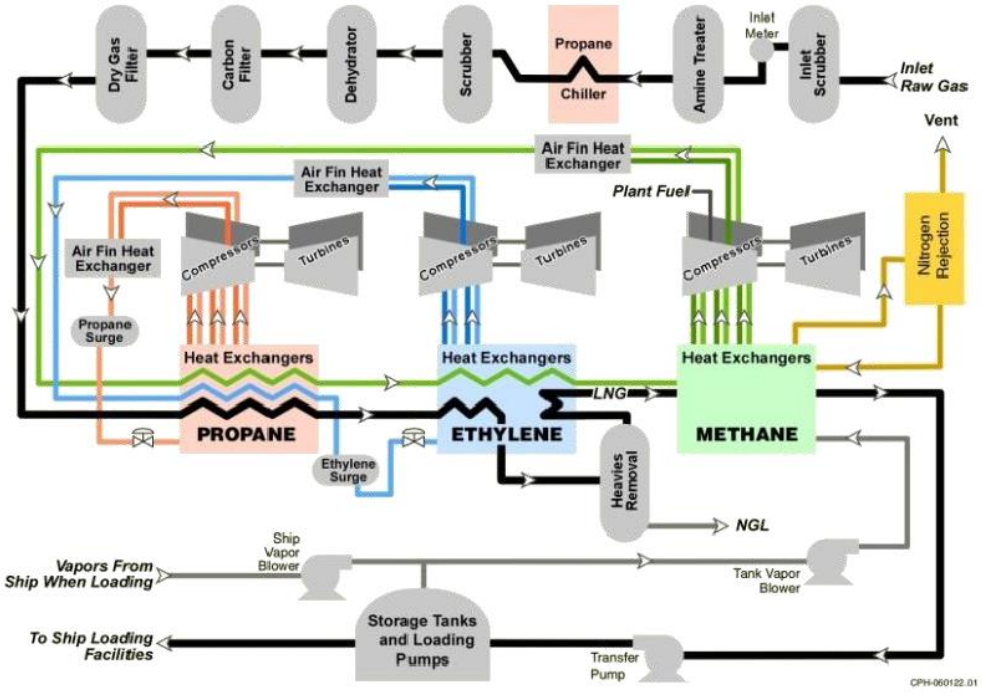

Figure 2-1: Simplified flow diagram of the optimised cascade process (Meher-Homji et al., 2008).

2.3 Loss Generation Mechanisms in Axial Turbines

Loss in axial turbines arises from a variety of flow mechanisms that increase the flow entropy. Viscous effects in boundary layers and in mixing processes, shock waves, windage, and heat transfer across temperature differences are some of the mechanisms reviewed in Denton (1993), Paniagua et al. (2004), Yoon et al. (2016), Palmer et al. (2016), and in Talnikar et al. (2016). They can be manifest in separating corner flows between the blade and the end-walls, flow ingress and ejection through stator-rotor wheel gaps, over-shroud leakage flows in shrouded rotors, tip leakage flows in unshrouded rotors, windage vortices,

passage vortices, horseshoe vortices, laminar separation bubbles, trailing edge vortex shedding, trailing edge wake mixing, and by other mechanisms. Changes in the static pressure field upstream and downstream of the blade rows may generate significant fluctuations in the pressure field around the blades (Kachel and Denton, 2006). Off-design operations may see significant shock-boundary layer interaction on the blades, with shock-induced boundary layer separation and partial shock refractions through the blade trailing edge wakes (Rona et al., 2006). This rich and complex variety of entropy-generating mechanisms stimulates both fundamental research and the development of new loss reduction concepts and techniques.

According to Denton (1993), Snedden et al. (2009), Philipp (2012), and Yoon et al. (2016), turbine losses are typically classified into blade profile losses, end wall losses, and leakage losses. Denton (1993) argues that the profile losses generate in the blade boundary layers and move away from the end walls, while the end-wall losses are classified as secondary losses because they arise from the secondary flows that are generated by the main passage flow through a blade row. Finally, the tip leakage flow loss arises from the flow leakage over of rotor blade tip clearance and the stator blade hub clearance (Denton, 1993). The leakage flow aerodynamic performance of the axial turbine was studied numerically and experimentally by Barmpalias (2011), Huang et al. (2013), and by Chen et al. (2016). The profile losses arise from the potential flow interaction, the vortex flow interaction, and the wake blade flow interaction (Peter, 2009, Philipp, 2012). Fuller descriptions of the profile losses are presented by Hodson and Dawes (1996), Rose and Harvey (1999), Chaluvadi et al. (2004), Behr et al. (2006), Kachel and Denton (2006), Matsunuma (2007), and Canepa et al. (2007).

The interaction between the main passage flow and a blade row generates secondary flows, which are typically prominent over the hub and the casing walls. The losses associated with these secondary flows are typically referred to as secondary flow losses or as end-wall losses (Denton and Pullan, 2012, Cui and Tucker, 2016). 30% to 50% of the turbomachinery stage loss is caused by secondary flow losses in the end-wall region (Sharma and Butler, 1986). Nice and Hooper (1977), Sieverding (1984), and Langston (2001) give an extensive survey on the generation of the secondary flow losses in axial turbines. An insightful diagram of the secondary flow vortex system in a turbine cascade with prismatic blades is reproduced from Moon and Koh (2001) in Figure 2-2. Figure 2-2 shows the separation of the inlet boundary layer at the blade leading edge into a horseshoe vortex. The blade pressure side vortex arm

is denoted as H_p and the blade suction side vortex arm is labelled H_s in Figure 2-2. The combination of H_p and H_s with the end-wall cross-flow that is directed from the blade pressure side towards the blade suction side generates a larger vortex structure, which is named as the passage vortex. Part of the boundary layer that separates at the turbine blade leading edge is rotated in the opposite direction to the passage vortex and this vortex type runs along the blade root down the pressure side and the suction side corners, as described by Langston (2001) and Coull (2017) and shown in Figure 2-2. This vortex type is known as the corner vortex.

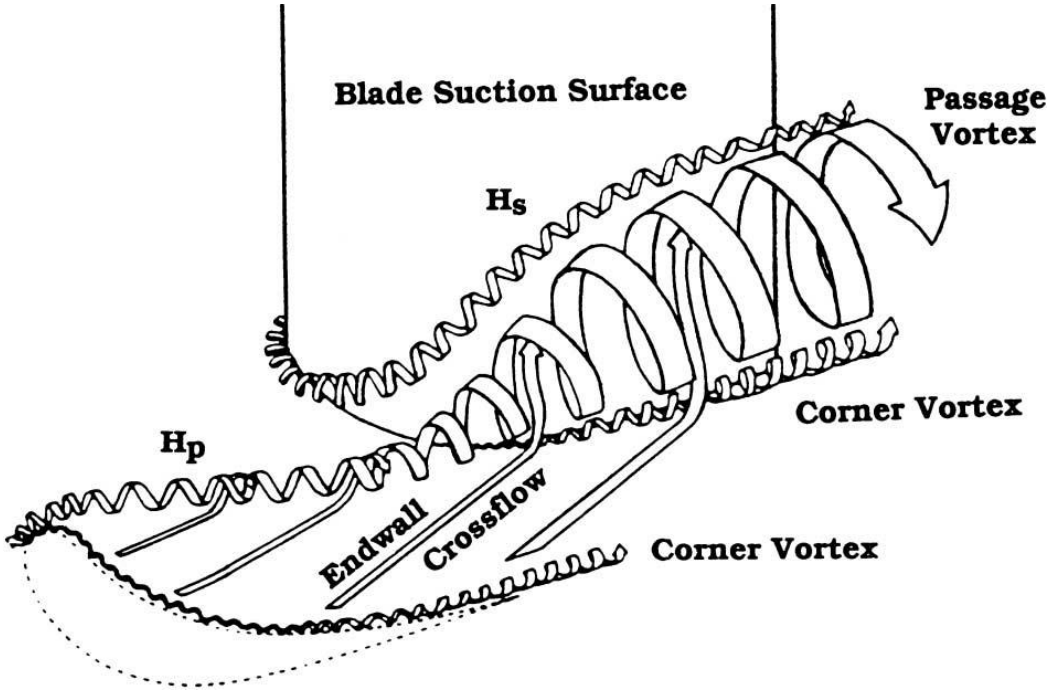

Figure 2-2: Secondary flow vortex system in a turbine cascade of prismatic blades (Moon and Koh, 2001).

Different techniques for measuring the secondary flow losses are given in Goldstein and Spores (1988), Ma et al. (2002), Lin et al. (2002), Praisner and Smith (2006a), Praisner and Smith (2006b), Matsunuma (2007), Rezasoltani et al. (2014), and Wang et al. (2014). The cost of measuring the loss differs from one author to another for full scale experiments. Pichler et al. (2016) state that the design of the next generation of turbomachines will rely on accurate numerical Computational Fluid Dynamics (CFD) predictions. CFD can predict the aerodynamic losses in turbines using three-dimensional Reynolds Averaged Navier-Stokes (RANS) equations (Turgut and Camci, 2016). In turbines, the end wall flow in the rotor is rather different from that in the stator. This was investigated on identical stator and rotor blade profiles using both unsteady calculations and steady calculations with mixing

planes by Denton and Pullan (2012). Therefore, this thesis has elected to examine end-wall modifications over the stator, following the notion that a mitigated secondary flow outflow from the stator may also benefit the subsequent rotor blade row. The next sections present a survey of the loss reduction techniques for axial turbomachines.

2.4 Loss Reduction Techniques

2.4.1 Suction and blowing

The main aim of secondary flow control is to reduce the loss that results from the separation of the flow over the end wall. Secondary flow control approaches can be classed as either active or passive (Philipp, 2012). Both active and passive control technique reduce the turbine profile and end-wall losses (Bloxham and Bons, 2014). Injection of air tangentially in the opposite direction to the secondary flow using slots leads to a reduction in the mixed out losses, but with no reduction in the net loss (Biesinger, 1993). Secondary flow losses can be reduced by sucking the working fluid from the end wall (Funazaki et al., 1996). Different flow visualization techniques, such as oil flow surface visualization, confirmed this in Funazaki et al. (1996). Changes in the flow led to a high value of stage efficiency.

In a high work turbine, the rotor tip leakage flow was actively controlled by Behr et al. (2006) using cooling injection holes from the turbine casing. Active flow control was tested experimentally by suction side blowing near the end wall of a highly loaded stator cascade with a pitch to chord ratio of 0.6 (Hecklau et al., 2011, Nerger et al., 2012). Five-hole-probe measurements in the spanwise and pitchwise direction were taken in addition to performing end-wall oil flow visualization. The data allowed the authors to identify changes in the flow that led to an increase in the stage efficiency.

2.4.2 Blade Lean

An alternative approach to reducing the secondary flow losses through a turbine stator is by changing the degree of reaction of the stage along the blade span. This can improve the rotor inflow at part-load operations, in low hub/tip ratio turbines (Harrison, 1990, Han et al., 1993, Zhongqi et al., 1991). This technique is also referred to as blade lean. Denton and Xu (1998) used both straight and compound blade lean to change the radial distribution of the whirl velocity. The compound blade lean decreased the blade row static pressure drop at the hub and at the casing compared to the mid-span. The use of the compound blade lean increased the blade load at the mid-span and decreased it at the stator hub and tip. This approach is

particularly suitable to obtain good stage performance at part-load, as it tends to enable the further expansion of the working fluid near the hub and casing of the rotor, therefore preventing flow separation at part-load. For this, it is known as a positive compound lean. Reverse compound lean is also available for controlling the passage flow. With reverse compound lean, the suction side of the blade generates an acute angle with the end wall (Snedden, 2011). Reverse compound blade lean was tested experimentally by Bagshaw et al. (2005) in a linear turbine cascade to achieve a reduction in the secondary flow losses. Their results show a reduction in the stage loss by 11% due to the reduction in the mixing losses by a more consistent turning angle of the stator outflows.

2.4.3 Blade twist

The turbine stage specific work output at the mid-span can be increased by twisting axial turbine blades along their span. Blade twist allows to reduce the turbine blade loading. By reducing the blade loading at the turbine hub and at the tip, Snedden (2011) reports that end-wall losses can be reduced. Schiegel et al. (1976) document early work on the effects of blade twist in a low aspect ratio axial turbine, by which they changed the radial work distribution. Their results show a 1% improvement in efficiency over a broad range of load. Both blade lean and blade twist were used by Lampart et al. (1999) in a turbine stage in order to decelerate the flow at the end-walls. According to Lampart et al. (1999), the stage isentropic efficiency was improved by only 0.4%, probably due to an increase in the profile loss. A 2.0% improvement in the stage isentropic efficiency was predicted in a turbine nozzle by changing the stacking angle by Watanabe and Harada (1999), who used a 3D inverse design method developed by Zangeneh (1991). Their flow analysis showed a reduction in the end-wall cross-flow and a suppression of the pressure side horseshoe vortex that forms at the turbine blade leading edge.

2.4.4 Fences

Secondary flow losses were reduced in a linear turbine rotor cascade by changing the end wall conditions, using an arrangement of fences, in the form of flow guide vanes erected on the end walls, to avoid the corner flow separation (Kawai et al., 1989, Kawai et al., 1990, Moon and Koh, 2001). By optimising the fence height, the pitchwise extension of the passage vortex is reduced and its interaction with the blade suction side is removed. A reduction in the total pressure loss coefficient of 8% in experiments was tested by Hergt et

al. (2011) using fences in a linear compressor cascade at the DLR with an inlet Mach number of 0.67.

2.4.5 End wall contouring

Contouring the end walls of turbine flow passages has become a relatively well-established technique for reducing the secondary flow losses. Example applications are given by Rose (1994), Hartland et al. (1998), Harvey et al. (1999), Bagshaw et al. (2008), Schuepbach et al. (2010), Dunn et al. (2010), Dunn and Von Backström (2011), Rose et al. (2003), Rose et al. (2001), and in Harvey et al. (2002) on a model rig of the Rolls-Royce Trent 500 engine. Contouring is implemented by parameterising the non-axisymmetric end walls between blades using different surface definition methods. The reduced losses lead to a decrease in the total pressure loss across the turbine stages and to an increase in the turbine isentropic efficiency.

Several authors applied non-axisymmetric end walls to reduce the extent of secondary flows, with the aim of reducing their associated loss. A reduction in the end-wall cross-flow can be achieved by modifying the end wall design to affect the radial pressure gradient (Snedden et al., 2009, Snedden, 2011). This approach was tested on a 1.5 stage low speed turbine and its performance was compared to that from an axisymmetric cascade at Durham (Snedden, 2011). A 1.5% improvement in the mixed-out stage efficiency was achieved at the design condition. With increasing load, the rotor flow is shown to be more uniform in the presence of the profiled end walls. The overall effectiveness of contoured end walls was tested experimentally by Mensch and Thole (2016) on turbine blades using a large-scale, low-speed, closed loop wind tunnel. The details of the wind-tunnel are given in Lynch et al. (2011). Mensch and Thole (2016) took flow field measurements on the contoured end walls. Their experimental results show a delay in the development of the passage vortex and in other passage secondary flow losses. These improvements reduced the area-averaged heat transfer coefficient and improved the film cooling effectiveness.

These early successes prompted the scaling up of end-wall contouring towards full engine applications. Non-axisymmetric end walls were tested on a linear cascade of turbine vanes by Nagel and Baier (2005). They used a transitional Navier-Stokes flow solver to perform a three-dimensional optimisation procedure on the turbine blades and on the end walls. The secondary flow losses in both an axial compressor and in a turbine were reduced by the end wall contouring using an adjoint Navier-Stokes solver. The adjoint was developed in terms

of the circumferential Fourier transform of axisymmetric and non-axisymmetric end walls at the inlet Mach number of 0.59 (Corral and Gisbert, 2008, Roque and Fernando, 2005). The adjoint end-wall contouring method was also used by Luo et al. (2011a), Luo et al. (2011b) on low aspect-ratio turbine blades. Their contoured design produced both loss reduction and an increase in the overall turning flow angle.

Several types of turbine hub and casing end-wall shapes were studied experimentally and numerically, defined by a variety design shape parameters. Inter-platform steps were added at the hub and shroud of the 1.5 stage Aachen Turbine by Kluxen et al. (2017). The separation of the inlet boundary layer of the stator was redirected by the steps. The steps generated sharp edges on all platform borders that reduced the combination of the separated boundary layers with the end-wall cross-flow. The URANS simulation by Kluxen et al. (2017) predicted a decrease in the hub entropy production rate from varying the platform geometry, which reduced the level of vortex formation at appropriate combinations of step shape and height.

Many researchers used turbine casing and hub curved walls to control the static pressure distribution. Various parameterisation methods were used to define these end-walls. End walls with bumps were designed and optimised using B-spline curves through a set of radially adjustable control points by Tang et al. (2016), Bezier curves were used by Hu and Luo (2014), cubic splines by Lynch et al. (2011), Praisner et al. (2013), Schobeiri and Lu (2014), Lynch and Thole (2016), and Kim et al. (2016), trigonometric functions by Sun et al. (2014a) and by Sun et al. (2014b), a cosine function at different axial positions by Li et al. (2015), optimised bumps with 28 free control points by Chen et al. (2012), a concavity in the the blade leading edge region by Inozemtsev et al. (2012), and a concavity near the blade suction and a convexity at the blade pressure side by Ingram (2003). Germain et al. (2010), Schuepbach et al. (2010), Taremi et al. (2013), Turgut and Camcı (2011), Dunn et al. (2014), and Turgut and Camci (2015) parametrised their end walls using the procedure detailed in Harvey et al. (1999). The streamwise bumps redirected the separation of the inlet boundary layer flow at the turbine blade leading edge and the endwall cross flow. In Ingram (2003), the corner separation was suppressed resulting in a more spanwise uniform exit flow. Loss reduction was obtained at large flow turning angles and the stage isentropic efficiency was improved due to the reduction in the static pressure that results from the flow acceleration through the concavity.

Other researchers tested geometrically sharper features on the end walls with some success. A sudden-jump groove near the blade pressure side was experimentally tested by Schwab et al. (2013) and Zimmermann et al. (2017) on the hub and shroud of a two-stage turbine. The maximum groove depth position was located at 0.5 axial chords from the blade leading edge. Their results show that the isentropic efficiency was improved by 0.34 % at the design conditions. A turbine blade with variable height fillets was designed and tested by Sangston et al. (2016). The turbine blade was designed with a high stagger angle at the mid-span transitioning to a low stagger angle near the end walls. The resulting end-wall flow structure combined with the good low Reynolds number blade profile performance at the mid-span to reduce the total pressure loss. Finally, an optimisation methodology based on an adjoint sensitivity analysis and a multipoint approximation method by Polynkin et al. (2010) was used by Shahpar et al. (2017) to design non-axisymmetric hub and tip end walls of a modern high-pressure (HP) turbine stage. The results showed that the stage efficiency was significantly increased by the reduction in the sealing flow required by the turbine.

2.5 Summary

The coefficient of performance of a liquefied natural gas cycle can be increased by increasing the thermal efficiency of the gas turbines that drive the cycle axial compressors. The thermal efficiency of an axial flow turbine can be increased by decreasing the stage total pressure loss. The turbine stage total pressure loss can be decreased by reducing the secondary flow losses. The secondary flow losses can be reduced by hub modifications including fences, slots, fillets, and grooves. Specifically, non-axisymmetric contoured end-walls reduce the flow separation in the pitchwise direction. From the literature review, the groove approach was found to be attractive because it does not require additional gas passages, unlike with wall slots. The fences redirect the separated boundary layer at the passage inlet but generate two passage vortices, whereas an end-wall groove sinks the separated flow and mitigates its interaction with the main passage flow. Another disadvantage of fences as compared to a groove is that they increase the shear stress of the flow boundary layers due to the fence sharp edges, unlike the smooth edges of a groove. This increases the flow disturbance and generates the second passage vortex, unlike the groove smooth edge. The procedure by Praisner et al. (2013) and Kim et al. (2016) is in current use in industry for designing parametrised contoured end-walls. This is used in this thesis as the reference

parameterisation for comparing its results against the author's own from a novel end-wall contouring technique, which is introduced in the next chapter.

3. CONTOURED HUB DESIGN BY PARAMETRIC SURFACES

3.1 Introduction

This chapter presents a new surface parameterisation approach for designing a contoured axial turbine hub. In general, the hub shape can be regarded as a composite geometrical surface $f(r, s, x) = 0$ depending upon the hub radius r, the pitch fraction s between two blades in a passage, and the axial coordinate x. End-wall surface definitions for $f(r, s, x) = 0$ from past axial turbomachinery studies are reviewed. This provides the contextual background for presenting the author's new surface parametrisation approach. Overall, the surface definition methods considered in this study are the Bezier curves, two-dimensional cubic splines from an array of control points, to form a hub with 'bumps', and continuous and discrete statistical distributions surfaces, to form a hub with a 'groove'. These parametric surface definitions all feature free parameters that are typically determined by a computer-based optimisation process, like the one described in Chapter Five, Section 5.4. In this work, the surfaces $f(r, s, x) = 0$ are coded and rendered graphically by MATLAB. The review of published end-wall surface definition and the author's new parametric hub definition described in this chapter are published in Obaida et al. (2016).

3.2 Survey of Contoured End Wall Surface Definitions

Reutter et al. (2009) performed a study with a 4-stage axial compressor in which the shape of the end wall hub was reshaped to minimize the secondary flow losses using an automated optimisation in terms of fillets and grooves for the fourth stage, by which a non-axisymmetric hub shape was obtained. The fillets and groove shapes were parameterised by 14 and 13 parameters, respectively, using Gauss probability density function curves. To contain the computational cost, they considered only the optimisation of the stator 3, rotor 4, and stator 4. In the optimisation, they monitored two performance indicators: the aerodynamic design point (ADP) and the operating point near the surge limits (OPSL). Due this end wall design, a significant reduction in entropy and corner flow separation led to a decrease in the total pressure loss. According to Reutter et al. (2009), there was no adverse effect on the total pressure characteristics of the stage due to the non-axisymmetric shaping of the rotor hub, which led to highly efficient blading.

Heinichen et al. (2011) studied a two-stage low speed axial compressor with a shrouded stator. They parameterised a non-axisymmetric end wall for the stator hub to reduce the hub

corner stall that was caused by the separation of the end wall boundary layer. Two sets of results were compared for qualifying the improvement in the stator performance. The first set used an axisymmetric end-wall and the second set a non-axisymmetric end-wall. The parameterisation details are reported in Section 3.3. According to Heinichen et al. (2011), a polytropic efficiency increase of 0.9% was gained by hub contouring.

Dorfner et al. (2011) parameterised the geometry of an axial compressor contoured hub and casing over the area from blade row entry to the exit, between the suction and pressure side of two adjacent blades. This parameterisation is defined by a matrix of control points that implement a groove between the blades. These control points are adjusted in the circumferential direction. This surface definition has 33 free parameters that require optimisation. The main features of this surface definition are a separation edge upstream of the leading edge and a groove running streamwise through the passage. In Dorfner et al. (2011), only the flow near the hub is reported to be influenced by the separation edge.

Schwab et al. (2013) designed and tested a tangential end-wall contouring (TEWC) in a two-stage steam turbine. TEWC is a rather complex geometry and needs a lot of care during the manufacturing process. TEWC is defined as a groove at the pressure side blade root. Both the hub and shroud of the stator and rotor turbine are contoured with TEWC. This groove is defined by a parabolic curve in the axial direction starting from the blade leading edge and ending at the blade trailing edge. In the pitchwise direction, the groove profile displays a monotonic depth increase followed by a sharp jump to zero depth, which forms a sharp edge or ridge. The groove width increases monotonically in the positive axial direction. TWEC was reported to increase the stage isentropic efficiency by 0.34% at the turbine design point.

Reutter et al. (2014) considered a different approach to contouring the hub of a two-stage turbine by first adding variable radius fillets to an axisymmetric hub and then by varying the remainder of the hub surface shape using interpolated splines. This method was implemented using non-rational B-spline surfaces (NURBS) in which the fillets are defined using 12 free parameter. Reutter et al. (2014) take six splines, one at the passage leading edge, one at the blade leading edge, two in the passage between two pitchwise consecutive baldes, one at the blade trailing edge and the last one at the passage trailing edge. Each spline is defined by five control points in the circumferential dirction. Their results showed a more homogenous flow structure and a reduction in the total pressure loss with the contoured hub.

Sun et al. (2014a) and Sun et al. (2014b) parameterised and optimised non-axisymmetric turbine end-walls. The non-axisymmetric design was applied to the stator and rotor hub and shroud surfaces. In the circumferential direction, the shroud was contoured by a sine curve and the hub surface by a cosine curve of half-period. In the axial direction, the amplitude of the cosine curve was changed from zero to its maximum and back to zero by a non-uniform B-spline curve. This B-spline curve was defined by 7 control points in the axial direction starting from the blade leading edge axial coordinate and ending at the blade trailing edge axial coordinate. With these contoured end-walls, the CFD and experimental results showed a reduction in the stage total pressure loss coefficient of 0.21%.

A key aspect of effective end wall design is in the use of computer-based optimisation, for compressing the design time-scales. An optimisation methodology based on an adjoint sensitivity analysis and a multipoint approximation method by Polynkin et al. (2010) was used by Shahpar et al. (2017). The parameterisation of the end walls are defined by Harvey et al. (1999). The countoured surface is defined by B-spline curve with six control points in the circumferential dirction. The amplitude of the B-spline curve at the axial dirction is defined by the first three terms in the Fourier series. This technique reduced the losses of a modern high-pressure (HP) turbine stage through the use of non-axisymmetric hub and casing walls. Shahpar et al. (2017) showed that the stage efficiency was significantly increased by the reduction in the sealing flow through the turbine rotor.

Finally, Praisner et al. (2013) and Kim et al. (2016) parameterised and optimised the non-axisymmetric nozzle hub and shroud of a single-stage high-pressure transonic turbine. Their parameterisation is based on cubic spline curves with a matrix of control points. Further details of this parametrisation are given in Section 3.4. They drove the surface definition using Kriging. This design improved the stage efficiency by 0.39%.

3.3 Bezier Curves

The Bezier surface is formulated following the approach reported in Heinichen et al. (2011). The shroud platform edges at the rotor-stator axial plane interfaces define the start and end positions of the 3-D contours. Pitchwise periodicity defines the lateral extent of the 3-D contours. Three main parameters are used to control the Bezier surface shape. These parameters are the axisymmetric radius shift Δr_1, the groove amplitude Δs, and the phase shift of the first order perturbation Δr_2. The Bezier surface is defined according to Piegl and Tiller (1997). Specifically, the n^{th} degree Bezier curve is defined by

$$R(u) = \sum_{i=0}^{n} B_{i,n}(u) P_i \qquad 0 \le u \le 1 \tag{3.1}$$

where, for a unit square,

$$B_{i,n}(u) = \binom{n}{i} u^i (1-u)^{n-i} \tag{3.2}$$

in which the Bernstein polynomial

$$\binom{n}{i} = \frac{n!}{i!\,(n-i)!} \tag{3.3}$$

The Bezier surface is defined as the product of two Bezier functions, starting from zero to one:

$$S(u,v) = \sum_{i=0}^{n} \sum_{j=0}^{m} B_{i,n}(u) B_{j,m}(v) P_{i,j} \qquad 0 \le (u,v) \le 1 \tag{3.4}$$

For $u = x$ (the axial coordinate) and $v = s$ (the pitchwise coordinate), equation (3.4) becomes:

$$S(x,\mathrm{s}) = \sum_{i=0}^{n} \sum_{j=0}^{m} B_{i,n}(x) B_{j,m}(\mathrm{s}) P_{i,j} \quad 0 \le (x,\mathrm{s}) \le 1 \tag{3.5}$$

Expression (3.5) can be re-cast in the matrix form:

$$S(x,\mathrm{s}) = \begin{bmatrix} 1 \\ x \\ x^2 \\ \vdots \\ x^n \end{bmatrix}^T \begin{bmatrix} a_{0,0} & a_{0,1} & a_{0,2} & \dots & \dots & a_{0,m} \\ a_{1,0} & a_{1,1} & a_{1,2} & \dots & \dots & a_{1,m} \\ a_{2,0} & a_{2,1} & a_{2,2} & \dots & \dots & a_{2,m} \\ \vdots & \vdots & \vdots & \vdots & \vdots & \vdots \\ \vdots & \vdots & \vdots & \vdots & \vdots & \vdots \\ a_{n,0} & a_{n,1} & a_{n,2} & \dots & \dots & a_{n,m} \end{bmatrix} \begin{bmatrix} 1 \\ s \\ s^2 \\ \vdots \\ s^m \end{bmatrix} \tag{3.6}$$

which can be also stated using a more compact notation as

$$S(x,\mathrm{s}) = \left[x^i\right]^T [A_1] \left[s^j\right] \tag{3.7}$$

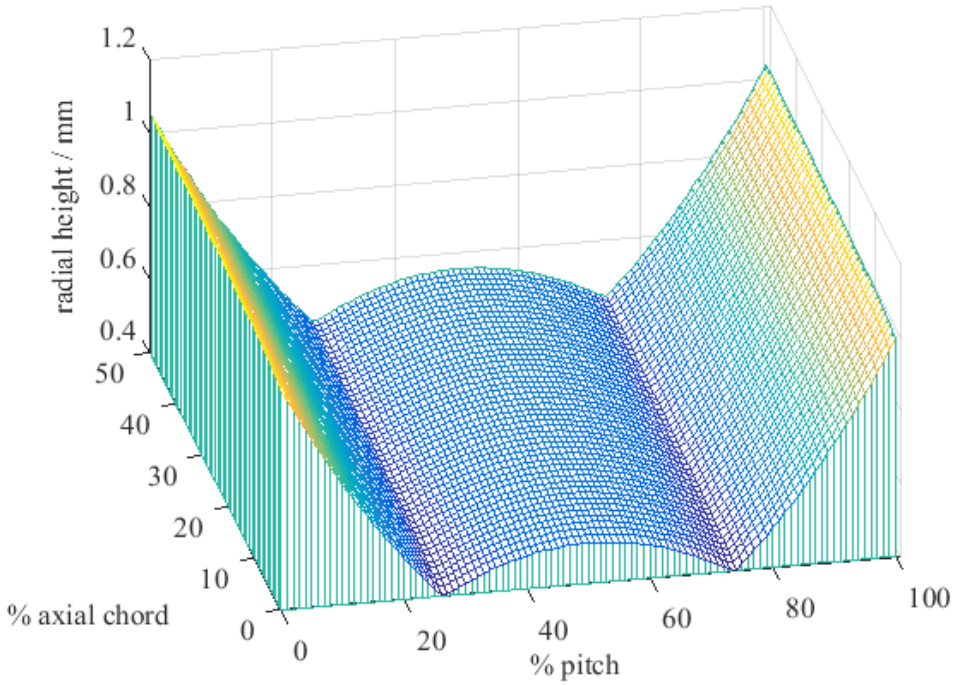

Figure 3-1: Bezier surface.

Figure 3-1 shows a sample Bezier surface obtained by evaluating expression (3.7) using MATLAB for the input parameters ($\Delta r_1 = 1.05,\ \Delta r_2 = 0.55, \Delta s = 0.42$). This example highlights some of the limitations of the Bezier surface technique. Pitchwise periodicity is achieved in terms of the radial height whereas pitchwise symmetry, rather than periodicity, is obtained for the radial height gradient. At the pitchwise boundaries, the radial gradient is non-zero in pitch and this requires some consideration where the Bezier surface interfaces with the blade root fillets, which may flare locally to a zero radial gradient surface.

3.4 Surface with Bumps from Cubic Splines by an Array of Control Points

An alternative to the use of the Bezier surface for defining a contoured end wall is to use the hub geometry definition method in Praisner et al. (2013) and in Kim et al. (2016). The end-wall shape is defined by two-dimensional cubic splines in the axial and pitchwise coordinates. A set of control points are used for the definition of the cubic spline curves. The control points are distributed between the camber lines of two pitchwise consecutive blades as shown in Figure 3-2. Five cubic splines ($P_1 - P_5$) are set at equal pitchwise distances between the blade camber lines. Each cubic spline is defined by five control points ($R_1 - R_5$) spaced evenly one-quarter axial chords apart. The P_1 and P_5 control points on the two blade camber lines are set as fixed points. The middle cubic splines have two fixed points

and three variable points each. Therefore, nine variable control points are available to modify the hub surface. The nine control points are restricted to vary in the radial direction to within $\pm$ 3 mm of the radial height of the corresponding fixed points on each spline.

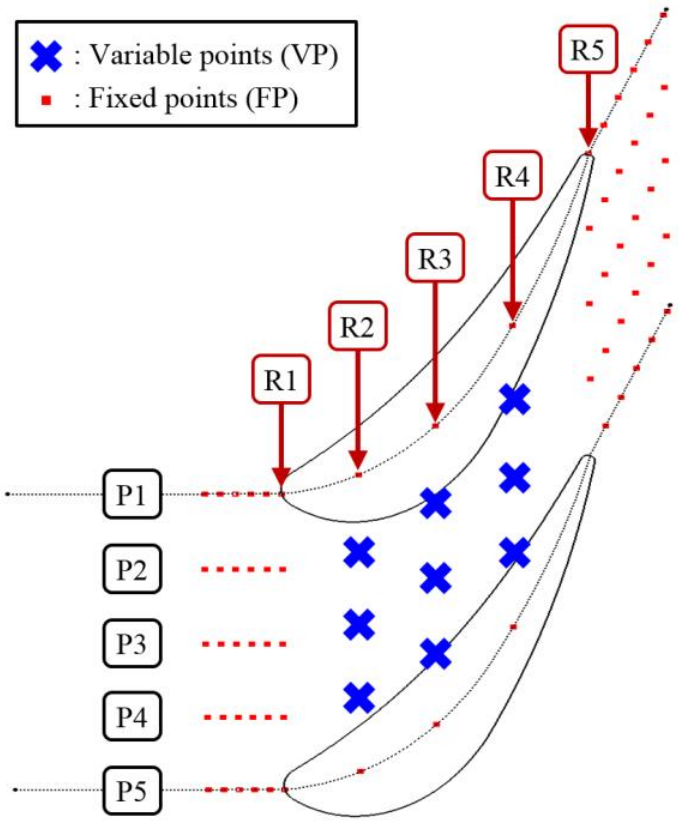

Figure 3-2: Schematic of end-wall control points (Kim et al., 2016).

Figure 3-3 shows the cubic spline curves between 5 control points. The first and end control points are kept constant while the remaining three middle points are displaced radially. The maximum height of the cubic spline is shown to occur between two control points. Kim et al. (2016) shows that the cubic splines P_4 and P_2 are the most significant splines for generating a performing hub surface with bumps, from the locations of the hub surface extrema determined by the optimisation process reported in Kim et al. (2016). On the basis of this observation, in this thesis, the variation of the nine control points was further restricted. On P_4, two points out of the three variable control points are constrained to having the same radial height, as shown in Figure 3-3. This gives a two-dimensional parameterisation of P_4. On P_2, only the middle control point is kept as a free parameter. Therefore, in this work, the stator hub surface definition of Kim et al. (2016) is constrained to three free parameters.

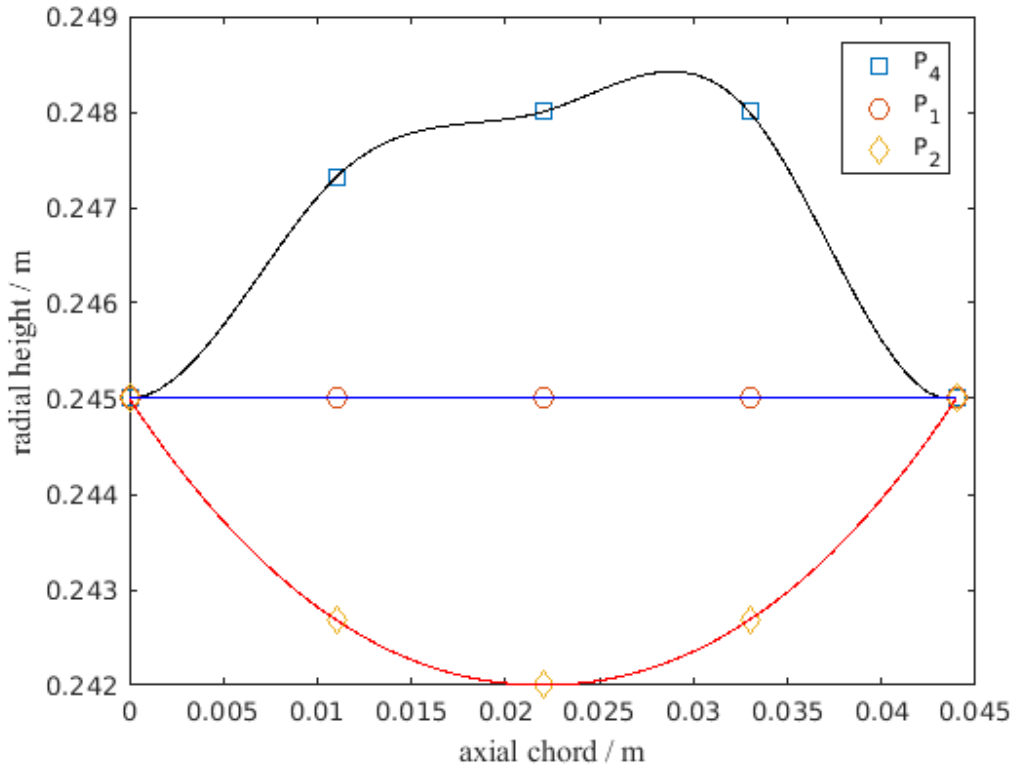

Figure 3-3: Cubic spline curves between five control points.

Using the MATLAB function 'spline', a cubic spline was fit between the selected control points. The change in the stator hub radius is obtained by interpolation between the five cubic splines ($P_1 - P_5$) as shown in Figure 3-4. By adding the radial height changes of Figure 3-4 to the reference axisymmetric hub, the contoured stator hub surface is obtained between the camber lines of two pitchwise consecutive blades, as shown in Figure 3-5.

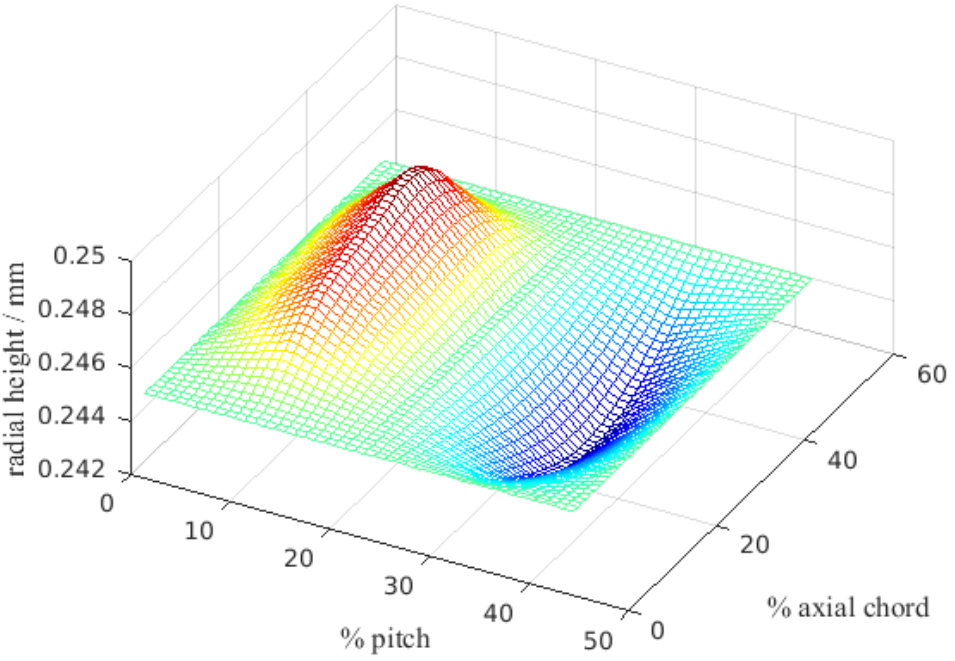

Figure 3-4: Changes in stator hub radius

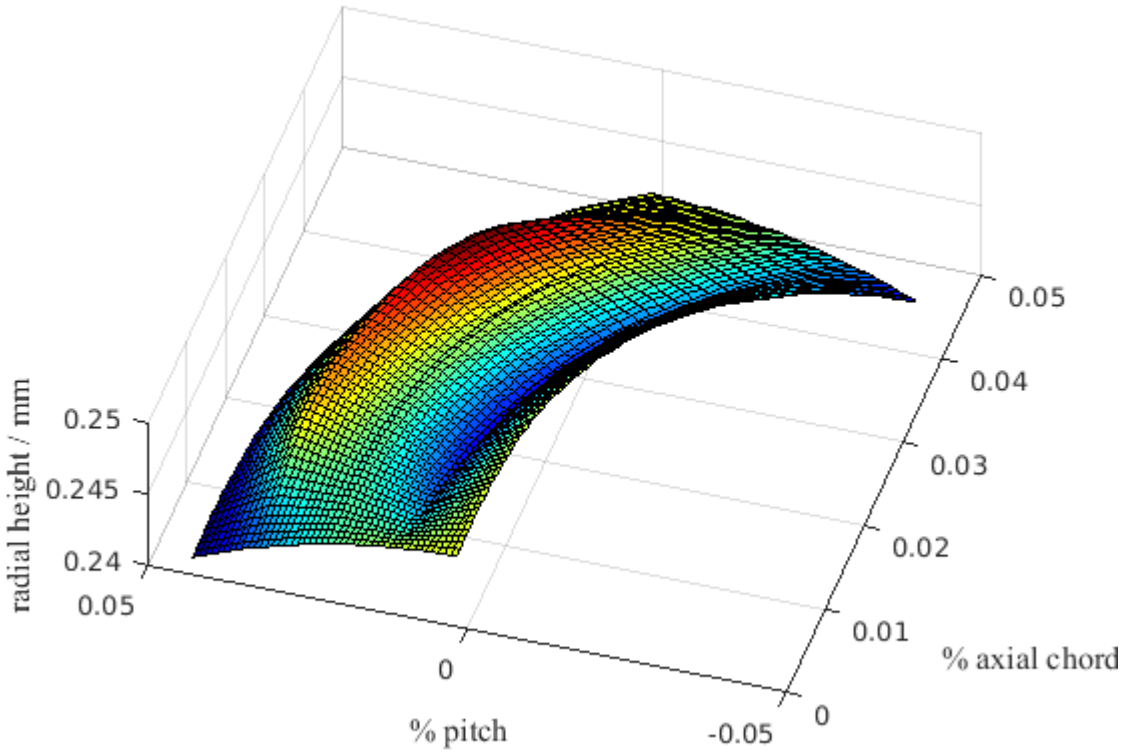

Figure 3-5: Stator hub surface using reference bump parameterisation by Kim et al. (2016).

3.5 Surface Generated by the Guiding Curve Technique

The guiding curve technique generates an end wall surface between two pitchwise consecutive stator blades with a groove that runs across the passage. The groove starts from the pressure side blade leading edge and ends at the suction side passage trailing edge. Six conditions are specified to obtain a smooth and performing non-axisymmetric end wall. These conditions are:

1. A groove is to be made over a sector of a cylinder of stator hub radius r_h and axial chord x.
2. The groove radial depth is small compared to r_h. The extent of the groove is further limited both in the axial direction and in the pitchwise direction. The axial limits are the passage leading edge and the passage trailing edge. The pitchwise limits are the suction and pressure sides of the blades. With N blades, the geometry in n periodic in pitch.
3. The groove should be a continuous analytical function $r_d = f(x, s)$ so that it can be arbitrary sampled at any position between two consecutive blades.
4. The groove depth should be a real number, subject to the constraint of $r_d \ll r_h$ and in practice $h \cong 3$ mm. It should not be an integer number or otherwise step-varying number. The machining tolerance in specifying the groove is 10^{-4} mm.
5. The groove radial depth r_d has to be zero at both the hub blade leading edge and the hub passage trailing edge over the full blade pitch. The groove radial depth slope has to be zero at the passage leading edge and it should be smooth up to the blade trailing edge.
6. The pitchwise maximum groove depth $h_0 = \max(R_d)$ in s_b. $R_d = f(x)$ increases monotonically from the pressure side blade leading edge to the suction side blade trailing edge and then it needs to meet the passage trailing edge end constraint stated in condition 5.

The following surface parametrization defines an end wall satisfying conditions 1 to 6. The end wall surface with a groove is designed with a set of free parameters using three guiding curves as shown in Figure 3-6. The first curve is located between the passage leading edge and the blade leading edge. The second curve is located in the middle of the end wall surface. The third curve is located between the passage trailing edge and the blade trailing edge. The first surface groove parameter L_1 is the axial distance from the passage leading edge to the

first curve. The second surface groove parameter L_2 is the axial distance from the passage leading edge to the second curve. The third parameter L_3 locates the third guiding curve from the passage leading edge. Each guiding curve is parameterised using two further parameters as shown in Figure 3-7.

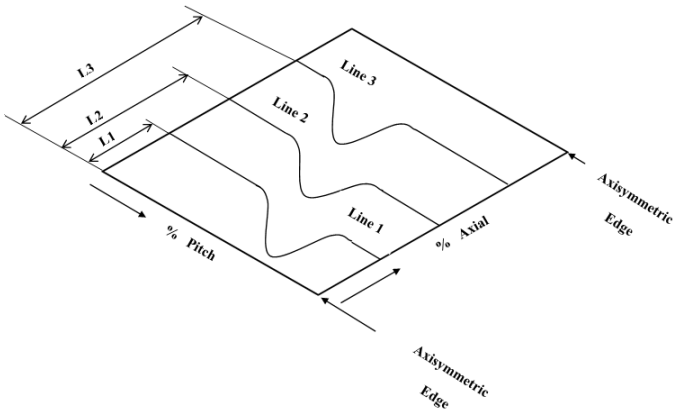

Figure 3-6: End wall design using three guiding curves.

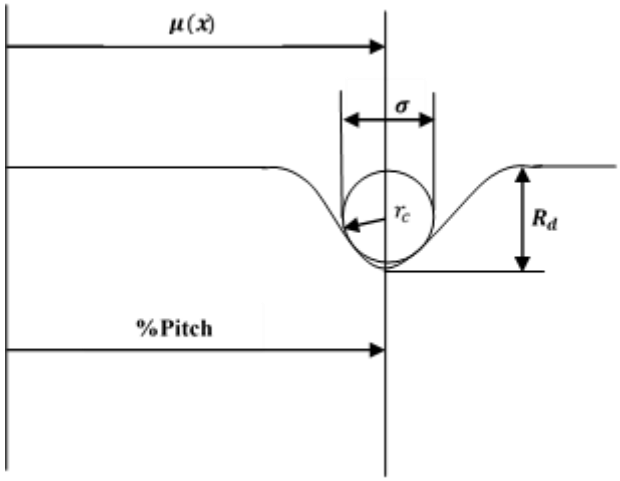

Figure 3-7: Guiding curve parameters.

These two parameters are the pitchwise position of the groove maximum $\mu(x)$ and the groove maximum depth R_d. At the upstream bulkhead and at the downstream bulkhead, the groove depth is zero so that the stator-rotor abutting hubs are axisymmetric.

The pitchwise position of the groove maximum $\mu(x)$ increases gradually from the pressure side blade leading edge towards the suction side passage trailing edge as a polynomial function in x, where x is the axial coordinate. The groove depth starts as zero at the pressure side blade leading edge, it gradually increases to a maximum value < 3 mm at the suction

blade trailing edge, and then gradually decreases to zero at the passage trailing edge. The groove is symmetric about $\mu(x)$ and its width $\sigma = f(r_c) = g(R_d)$. σ could be determined, for instance, as the inscribed circle of radius r_c. r_c represents the idealised axial cross-section of the pressure side branch of the horseshoe vortex over the hub accommodating itself into the guide groove. In this section, the graphical rendering of $r_d = f(x, s)$ uses a constant value for $\mu(x)$, for simplicity.

The hub surface contour, stated as $r_d = f(x, s)$, is determined using polynomial curve fitting. The three guiding curves are interpolated along the axial distance x, starting from the passage leading edge and ending at the passage trailing edge, at constant pitch fraction s. This is done using the MATLAB functions polyfit and polyval, which fit polynomial curves through discrete points. According to Adrian and Moshe (1996), the ployfit function in MATLAB determines the coefficients of the polynomial running through a given set of points, which, in this application, are (r_d, x) points at constant s. The polyval function evaluates this polynomial at x values located between the three guiding curves, based on these coefficients. The polynomial curve fitting equation is defined as:

$$f(x) = a_o\, x^M + a_1\, x^{M-1} + a_2\, x^{M-2} + \cdots + a_{M-1}\, x + a_M, \text{ on } s \text{ planes} \quad (3.8)$$

The value M of the polynomial degree is equal to the number of data points minus one. In this case, five data points (r_d, x) are used at constant s and M = 4. These points are $r_d = 0$ at the passage leading edge, the three guiding curves evaluated at constant s, and $r_d = 0$ at the passage trailing edge.

To produce the three guiding curves, two different analytical representations were considered. These were continuous and discrete statistical probability density functions. The discrete functions were the Binomial and the Poisson probability density functions. The continuous functions were the Gauss, Gamma, Chi-squared, and the Beta curves. It is to be noted that, in this work, the statistical probability density functions are not used to express any stochastic variable but just as analytical functions, or curves, describing r_d as function of s at constant x. Three parameters define each guiding curve: the pitchwise position of the groove maximum $\mu(x)$, the groove maximum depth R_d, and the groove width σ.

3.5.1 Discrete statistical distribution functions

The discrete probability density functions represented by both the Binomial and the Poisson distributions have the ability of generating a zero value at both tail ends of the curve. This is an advantage for joining up the groove surface and the blades edges. However, in this work, the parameterisation of the axial turbine by discrete statistical distributions is not used. The discrete points of these probability density functions are not evenly distributed, as shown in Figure 3-8. The curve sampling points are not arbitrary and this constrains the spatial discretization of the surface, with an adverse impact on the generation of any computational mesh for the numerical modelling of the flow. According to this, the parameterisation using the Binomial and the Poisson curves have been considered but then discarded in favour of using continuous analytical functions.

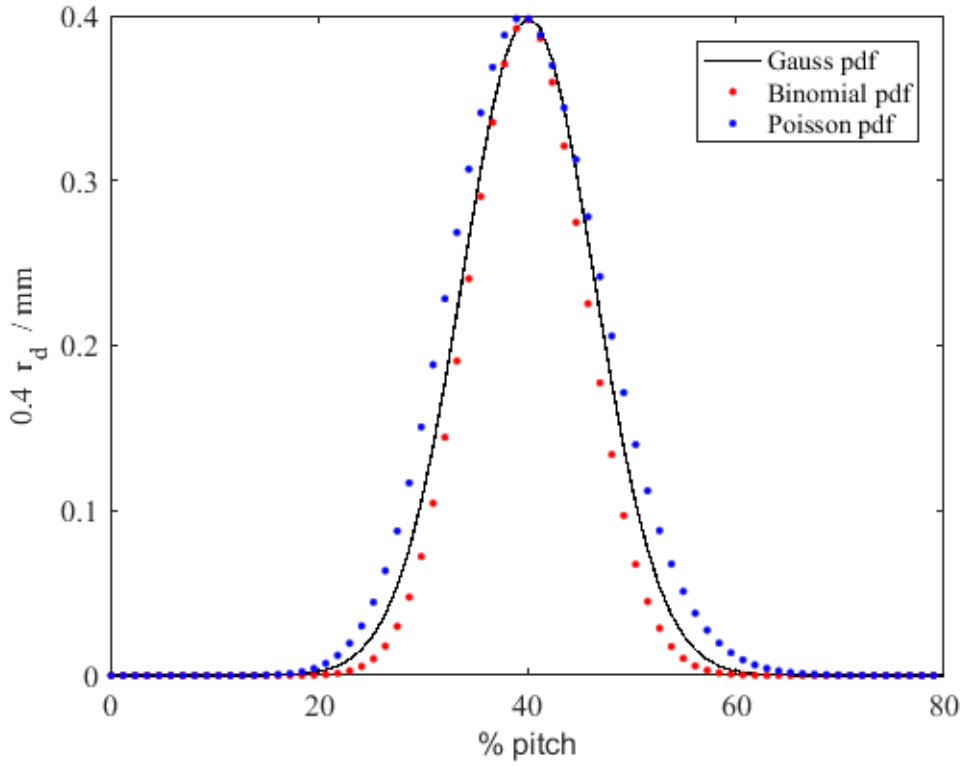

Figure 3-8: Comparison between continuous and discrete distributions.

3.5.2 Continuous statistical distributions

3.5.2.1 The Gauss distribution

The Gauss probability density function, or Normal distribution, is a popular statistical distribution used in many applications (Ma, 2011). Following the procedure in Reutter et al. (2009), the three guiding grooves are defined using the general equation of the Gauss probability density function:

$$f_2(s) = (2\pi\sigma)^{-1/2}\, e^{-\frac{(s-\mu)^2}{2\sigma^2}} \tag{3.9}$$

where σ represents the pitchwise width of each groove and μ the pitchwise position of the groove maximum depth on the axial plane. Equation (3.9**)** defines the groove depth, that is, the change in the hub surface radius with respect to the non-contoured axisymmetric hub in the (x, s) plane along each of the three guiding grooves, along s at constant x. The parametric form of equation (3.9**)** used in this work is:

$$f_2(s; x, \mu, \sigma, R_d) = R_d \left[\frac{e^{-\frac{(s-\mu(x))^2}{2\sigma^2/\sqrt{n}}}}{0.4} \right] \tag{3.10}$$

where $\mu(x), \sigma$, and R_d are the parameters of each guiding groove, x is the axial plane of each groove, and n is an arbitrary number of equispaced points in pitch at which $f_2(s)$ is evaluated, as shown in Figure 3-8. Once the three guiding grooves are defined as $f_2(s)$ parametric functions, the groove depth in the (x, s) plane is obtained by performing the axial interpolation among the three guiding curves according to the procedure in section 3.5. This gives the depth distribution of a smooth groove starting from the passage leading edge to the passage trailing edge, as shown by Figure 3-9.

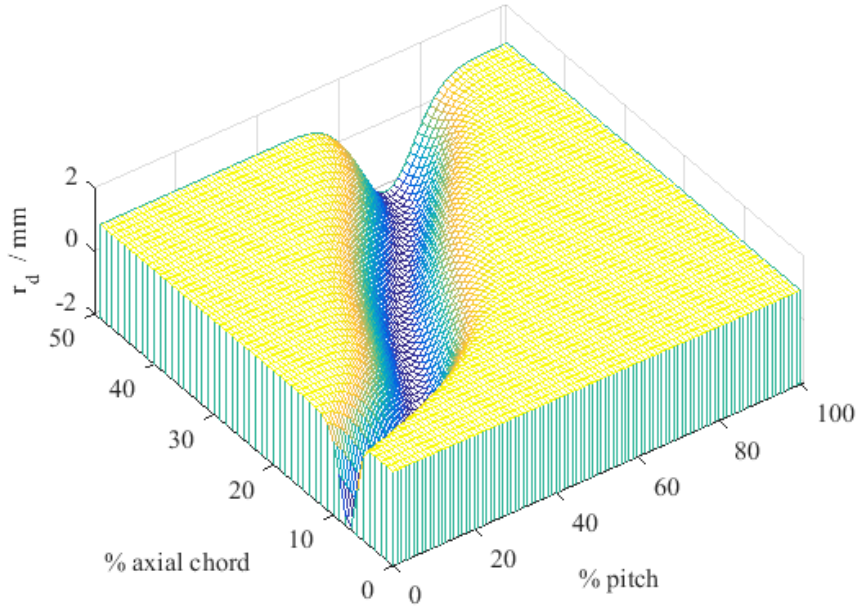

Figure 3-9: Depth distribution of hub groove generated by three Gauss guiding curves.

3.5.2.2 The Gamma distribution

According to Devore (2015), the general form of the Gamma distribution is defined as:

$$f_2(s) = \frac{1}{\beta_s^{\alpha_s}\Gamma(\alpha_s)} s^{\alpha_s - 1} e^{-\frac{s}{\beta_s}} \qquad s \geq 0 \tag{3.11}$$

where: $\Gamma(\alpha_s) = (\alpha_s - 1)!$ (3.12)

The Gamma distribution depends on two main factors, the shape factor α_s and the scale parameter β_s. $\beta_s > 1$ either stretches or compresses the Gamma probability density function in the s-direction. Equation (3.11**)** can be used for generating a groove guide curve:

$$f_2(s, \alpha_s, \beta_s) = R_d \left[\frac{\frac{1}{\beta_s^{\alpha_s}\Gamma(\alpha_s)} s^{\alpha_s - 1} e^{-\frac{s}{\beta_s}} * \sigma}{0.4} \right] \qquad s \geq 0 \tag{3.13}$$

$$\alpha_s = \mu^2\sigma^{-2} \tag{3.14}$$

$$\beta_s = \sigma^2\mu^{-1} \tag{3.15}$$

where $\mu(x), \sigma$, and R_d are the groove parameters on a given axial plane. This leads to an approximate match between the Gamma distribution and the Gauss distribution for $\sigma = \mu$ only. The Gamma distribution has the ability to get to zero at one bounded tail (the left tail) which means that $f_2(0, \alpha_s, \beta_s)$ equals to zero. Equation (3.13**)** includes the multiplying factor σ, which is the variance of the Gamma probability density function. This scaling factor gives the same normalized maximum groove depth of 0.4 as with a Gauss probability density function (Figure 3-8), as shown in Figure 3-10.

3.5.2.3 The Chi-square distribution

The Chi-square distribution is a special case of the Gamma distribution. The Chi-square shape depends on the number of degrees of freedom ϑ that is equal to the double of the shape parameter α_s of the Gamma distribution. In the Chi-square distribution, ϑ is integer and $\beta_s = 2$. These produce the curve shown in Figure 3-10.

In both the Gamma and the Chi-squared probability density functions, the number of degrees of freedom and the shape parameter cannot be varied independently from one another. This restricts the choice of spatial discretization available for a given shape. Due to this restriction, both the Gamma probability density function and the Chi-squared probability density function are not used.

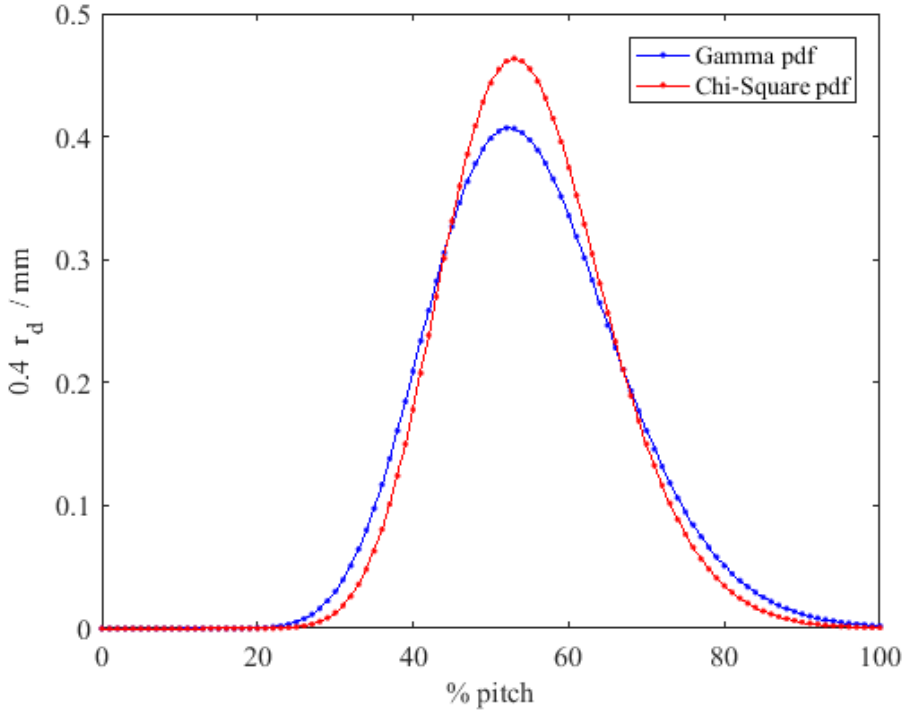

Figure 3-10: Gamma and Chi-squared probability density functions.

3.5.2.4 The Beta distribution

Devore (2015) defines the standard Beta distribution as a function of the shape factor ($\alpha_s > 0$) and of the scale factor ($\beta_s > 0$) over the finite range ($0 < s < 1$). The general standard formula of the Beta distribution is:

$$f_2(s) = \frac{\Gamma(\alpha_s + \beta_s)}{\Gamma(\beta_s).\Gamma(\alpha_s)} s^{\alpha_s - 1} (1 - s)^{\beta_s - 1} \qquad 0 < s < 1 \qquad (3.16)$$

By scaling equation (3.16**)**, the parametrised groove curve

$$f_2(s; \alpha_s, \beta_s, R_d) = R_d \left[\frac{\sigma * \frac{\Gamma(\alpha_s + \beta_s)}{\Gamma(\beta_s).\Gamma(\alpha_s)} s^{\alpha_s - 1} (1 - s)^{\beta_s - 1}}{0.4} \right] \qquad 0 < s < 1 \qquad (3.17)$$

is obtained, where the shape factor α_s and the scale factor β_s,

$$\alpha_s(\mu, \sigma) = \frac{(1 - \mu - \sigma^2 \mu^{-1})}{\sigma^2 \mu^{-2}} \qquad (3.18)$$

$$\beta_s(\mu, \sigma) = \frac{\alpha_s\,(1-\mu\,)}{\mu} \tag{3.19}$$

are related to the pitchwise position of the groove bottom, μ, and to the groove pitchwise width, σ, as defined in Figure 3-7. For $\alpha_s = \beta_s$, the Beta distribution approximates the normal distribution. The Beta distribution generates zero values of groove height at the left and right bounds $f_2(0, \alpha_s, \beta_s) = 0$ and $f_2(1, \alpha_s, \beta_s) = 0$. The maximum groove depth is $0.4\,R_d$ at $\mu(x)$ and this matches the maximum groove depth obtained with either the Gauss or the Gamma curves, in Figure 3-8 and Figure 3-10. Figure 3-11 can be calculated by multiplying equation (3.17) by the variance of the Beta distribution.

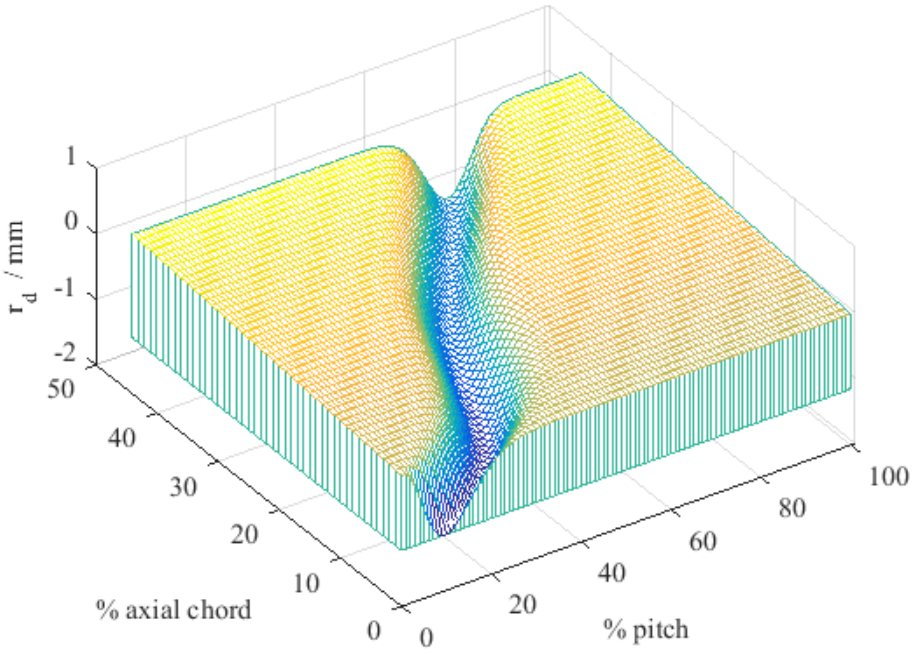

Figure 3-11: Depth distribution of hub groove generated by the Beta function.

Figure 3-11 shows a sample end wall surface generated using the Beta probability density function for the parameters $\alpha_s = 12,\ \beta_s = 47,\ R_d = 1$. From the perspective of their use as guide curve for end-wall contouring in axial turbines, an important difference between the normal probability density function and the Beta probability density function is the support, or domain, of these functions. The normal probability density function is defined over the interval $(-\infty, \infty)$ whereas the Beta probability density function is defined over the finite interval $(0,1)$. As an axial turbine row of N blades is n-periodic in pitch, the interval

$(-\infty, \infty)$ is less amenable to be folded into a finite n-periodic pattern than the finite interval $(0,1)$.

The support of the Beta probability density function $(0,1)$ appears to be a more natural fit for an n-periodic geometry, as it can be scaled to match one period exactly, without resorting to truncating the tails of the distribution function. Furthermore, the Beta probability density function generates zero values of groove height at the left and right bounds, $f_2(0, \alpha_s, \beta_s) = 0$ and $f_2(1, \alpha_s, \beta_s) = 0$. This enables mating with either the blade surface at the blade root, on the hub, and at the blade tip, on the casing, without the aid of additional geometry patches.

The parametrisation of the contoured end-walls using the Beta probability density function appears to offer some attractive advantages over other analytical formulations considered in this thesis, including the normal probability density function that was used in previous work. This analysis provides the foundations for experimenting with end walls contoured using the Beta probability density function and testing this end wall treatment, for instance by computational fluid dynamics, for its effect on the stage total pressure loss and the flow structures. The end goal is to obtain an increased stage isentropic efficiency.

3.6 Summary

This chapter reviewed surface definition techniques used by past authors for designing turbomachinery passages with contoured end-walls. Three main surface definition approaches were studied in detail. The first approach used a Bezier surface. This approach was found to have the drawback of not generating a zero radial gradient slope at the perimeter of the contoured surface, to provide a smooth transition with the remainder of the passage geometry. The second approach was the use of cubic splines for generating surface "bumps" through an array of control points. The third method used three pitchwise guiding curves that were interpolated axially by fourth-order polynomials. The three guiding curves were defined using both discrete and continuous probability density functions. After considering the advantages and disadvantages of the different surface definition methods, two surface parametrisation methods are retained for application and testing in the forthcoming chapters. These are the method of cubic splines, which can be argued represents the state of the art in use in current turbomachines, and the guiding curve technique that uses a Beta probability density function, which represents a novel application of the Beta probability density function to end wall contouring. Both methods produce parametric surfaces of type $r_d =$

$f(x, s)$ with no restriction in spatial resolution. Both methods have been coded in MATLAB and their surfaces rendered graphically, for selected parameter values.

4. TURBINE FLOW PASSAGE WITH PARAMETRISED HUB

4.1 Introduction

This chapter describes the implementation of the parametrised hub surface from Chapter 3 to the 1.5 stage Aachen Turbine. The change to hub surface is applied to stator 1. The design of the contoured hub is implemented by specifying a guide groove between pitchwise consecutive stator 1 blades. This groove starts from the stator 1 blade leading edge and ends at the stator 1 passage trailing edge. The groove path is defined by interpolation between the blade root suction side and the blade root pressure side profiles, offset from the blade surface. The groove depth is defined by using the Beta probability density function. Three user-defined parameters define the parametrised guide groove. The contoured hub is exported as a NURBS surface and mated with the remainder of the 1.5 stage Aachen Turbine geometry. The hub surface parameterisation is implemented in MATLAB. A second parametrised geometry of the 1.5 stage Aachen Turbine is generated using the hub contouring surface definition by Praisner et al. (2013) and Kim et al. (2016). This second parametrisation, which uses a more conventional technique involving a set of control points and cubic splines, provides a state of the art contoured hub definition, for turbine performance comparison purposes. This reference contoured hub surface is also exported as a NURBS surface.

4.2 1.5 Stage Turbine Geometry Test Case

The main validation test case "Aachen Turbine" was provided by the Rheinisch-Westfälische Technische Hochschule (RWTH) Aachen (Volmar et al., 1998), (Walraevens and Gallus, 1997), and (Gallus, 1995). The measurements on the test case "Aachen Turbine" were carried out at the Institute of Jet Propulsion and Turbomachinery at RWTH Aachen, Germany. These low steady three-dimensional (3D) stator experimental data were used to validate the numerical flow predictions in the current work.

The turbine stator and rotor blade profiles are given by Gallus et al. (1990) and by Walraevens and Gallus (2000) as a cloud of points of the pressure and suction sides. Both the stator and the rotor consist of untwisted blades. The stator and rotor blade points are imported as x, y, and z coordinates in ANSYS ICEM CFD, where x is the axis of rotation of the turbine in the direction of the flow expansion. The 1.5 stage has cylindrical end walls with hub and tip radii of 245 mm and 300 mm respectively. The stator blades are pitchwise stacked at the trailing edge while the rotor blades are pitchwise stacked at their centroid,

which is located at x = 25.265 mm and y = 13.456 mm from the rotor blade leading edge. The stator blade chord c_s is 62 mm, the stator axial chord c_x is 44.25 mm, and the pitch to chord ratio s_s/c_s is 0.77, which gives 36 blades around the cascade. The rotor chord c_r is 60 mm and the pitch to chord ratio s_r/c_r is 0.67, which gives 41 blades around the cascade, as shown in Figure 4-1 and Table 4-1. The passage leading edge extends axially 486 mm upstream of the stator leading edge in order to develop the boundary layers on the passage end-walls as shown later on Section 5.3.2. The turbine blade span H is 55 mm. The inlet flow angle α_1 is 90° relative to the axial plane, so that the inflow is axial. The downstream row of stator blades is clocked by 3° in the positive direction of rotation of the rotor, with respect to the upstream row of stator blades.

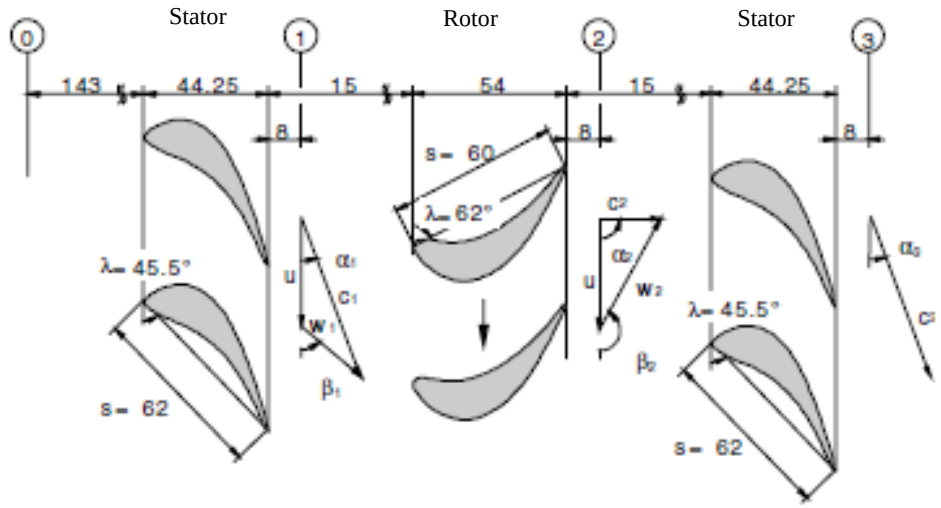

Figure 4-1: Schematic of turbine stage on the cascade plane (Gallus et al., 1990).

Table 4-1: Turbine stage design data.

	Cascade	Stator	Rotor
Aspect ratio, H/s	variable	0.887	0.917
Pitch (midspan), s	50 mm	47.6 mm	41.8 mm
Blade number, N	7	36	41
Reynolds number, based on chord and exit velocity	6.8×10^5	6.8×10^5	4.9×10^5
Mean radius	-	272.5 mm	272.5 mm
Rotational speed	-	-	3500 rpm
Working fluid	air	air	air

4.3 Design of a Contoured Hub with a Guide Groove

A procedure for designing contoured end-walls was created using the Alstom Process and Optimisation Workbench (APOW) software. This required representing the end-wall geometry by a small set of parameters, so that the optimisation becomes treatable. To accomplish this goal, four main activities were undertaken.

The first activity consisted in identifying a surface definition approach from classical analytical surface theory that could represent the contoured end wall of a turbomachine stage. The generalized surface definition as parametrisation $s(u, v)$ was selected as it can describe a continuous function in $\mathbb{R}3$. The second activity consisted in constraining the parametrisation $s(u, v)$ so that it satisfies a range of desirable characteristics, such as matching the passage perimeter along the passage leading and trailing edges, at the blade pressure and suction sides, and at a pitchwise periodic plane. At a later stage, the function will be including non-axisymmetric flow features. At this stage, the $s(u, v)$ parametrised surface is constrained to be axisymmetric, so that the process of surface definition and surface rendering in combination with computational fluid dynamics can be tested in its entirety. The third activity is to import the $s(u, v)$ parametrised surface in a computational fluid dynamics mesh generator, which only recognizes a finite set of input geometries, such as points, facets, and non-uniform rational B-splines (NURBS). The fourth and the final stage is to check the difference between the hub surface generalized by this process against a benchmark surface that is not imported but is generated directly inside ICEM CFD using current best computer aided design (CAD) drawing practices.

To maximize the compatibility of the optimisation workflow, surfaces are defined analytically and parametrically in MATLAB, imported in the CFD mesh generator ANSYS ICEM CFD, and the flow model is solved by OpenFOAM. APOW is used to automate this process by executing this workflow in batch mode.

4.4 Application of the Guide Groove Design to the Upstream Stator Hub

The upstream stator hub surface forms the floor of one of the hexahedral computational domain blocks inside the structured multi-block domain of Figure 4-1, which models one flow passage through the 1.5 stage turbine from RWTH Aachen. 16 points define the vertices of the multi-block domain structure. Eight of these points are the vertices of the stator hub block. The geometry, including these vertices, is defined in the RWTH Aachen dataset with respect to the cylindrical reference system (x, r, θ), where the x axis coincides

with the axis of rotation of the rotor, pointing towards the outlet, r is the radial distance from this axis, and $\theta = 0$ is through the prismatic stator blade trailing edge. Four of the eight vertices define the stator 1 passage leading edge and the remaining four define the stator 1 passage trailing edge. As ANSYS ICEM CFD uses a 3D Cartesian reference system, each turbine stator 1 passage vertex P_i on the hub is translated in 3D Cartesian coordinates as:

$$P_i = (x_i, r_h \cos\theta_i, r_h \sin\theta_i) \tag{4-1}$$

where: x_i is the $x-$coordinate of the i^{th} point. The resulting coordinates of point P_i are shown in Table 4-2. The azimuthal angle θ is defined as positive from A to B.

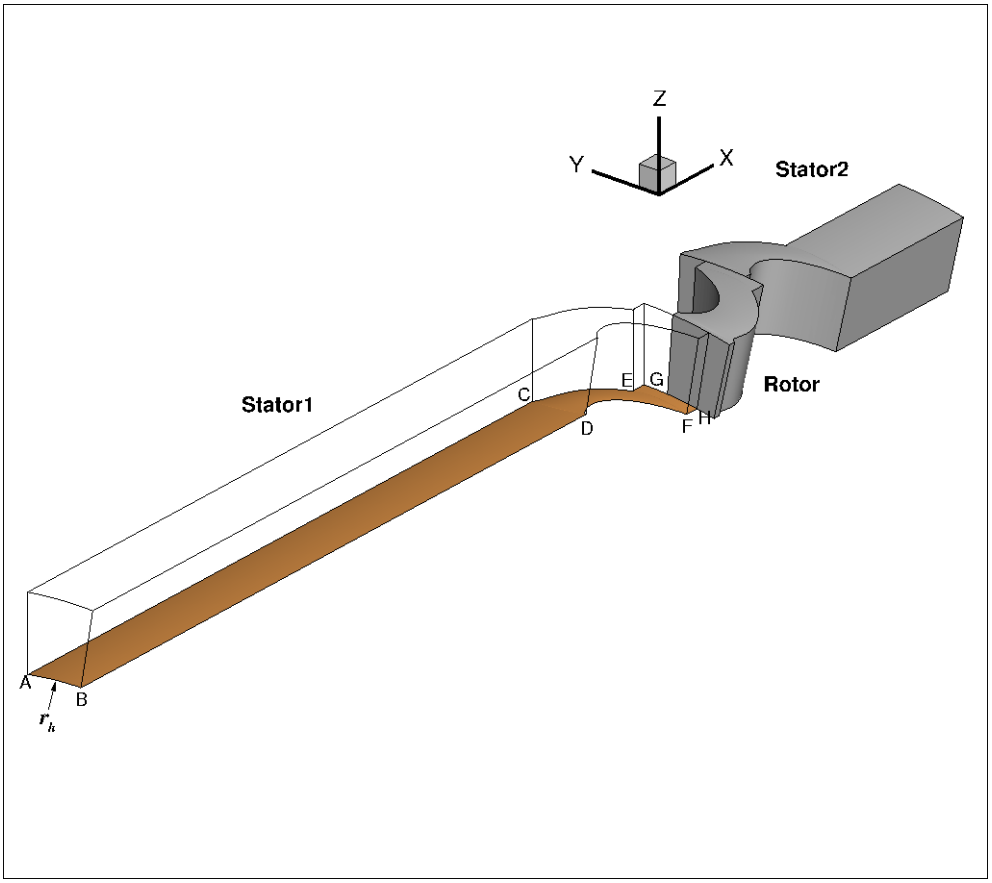

Figure 4-2: Aachen Turbine stator geometry created using ANSYS ICEM CFD showing the stator 1 hub vertices.

Table 4-2: Coordinates of the Aachen Turbine stator 1 hub vertices.

points	r_h (m)	θ (rads)	x-coordinate (m)	y-coordinate (m)	z-coordinate (m)
A	0.245	1.3947	-0.486	0.04292951	0.2412096
B	0.245	1.5645	-0.486	0.001547395	0.2449951
C	0.245	1.3947	0	0.04292951	0.2412096
D	0.245	1.5645	0	0.001547395	0.2449951
E	0.245	1.5708	0.04397504	0	0.245
F	0.245	1.7406	0.04397504	-0.0414052	0.2414759
G	0.245	1.5708	0.155575	0	0.245
H	0.245	1.7406	0.155575	-0.0414052	0.2414759

The turbine stator 1 blade profile in the $x-y$ plane is defined as a tabulated set of 116 points in Walraevens and Gallus (2000). The stator blade pressure side edge, denoted by CE in Figure 4-9, is defined by 65 points, while the suction side edge, denoted by DF, is defined by 47 points, on the $x-y$ plane. These points are projected on the cascade plane by a prismatic extrusion in z. Specifically, the vertices CDEF delimiting the hub of one flow passage between the suction and the pressure sides of two pitchwise consecutive blades were projected on the cascade plane by:

$$P_i = \left(x_i, \frac{\pi}{2} - \arctan\left(\frac{y_i}{z_i}\right)\right) \tag{4-2}$$

The projected points that define the pressure side edge of stator 1 were interpolated using a smoothing cubic spline, as shown in Figure 4-3. The coefficients of the smoothing cubic spline φ_p were obtained by the MATLAB functions csaps and ppval. The same procedure was repeated for the stator 1 suction side edge, to obtain the smoothing cubic spline φ_s shown in Figure 4-4.

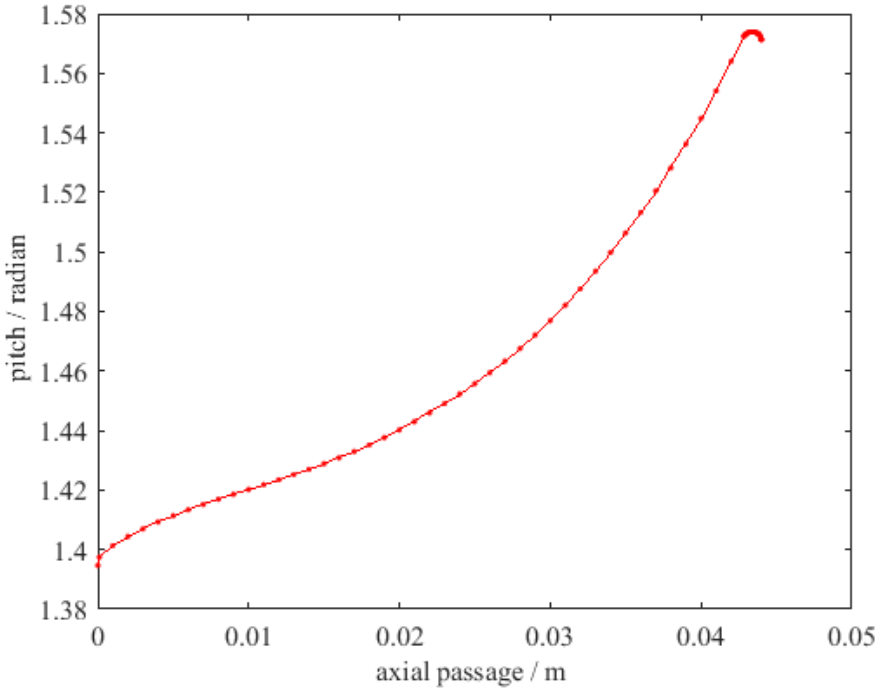

Figure 4-3: Interpolation function φ_p across the Aachen Turbine stator pressure side blade coordinates.

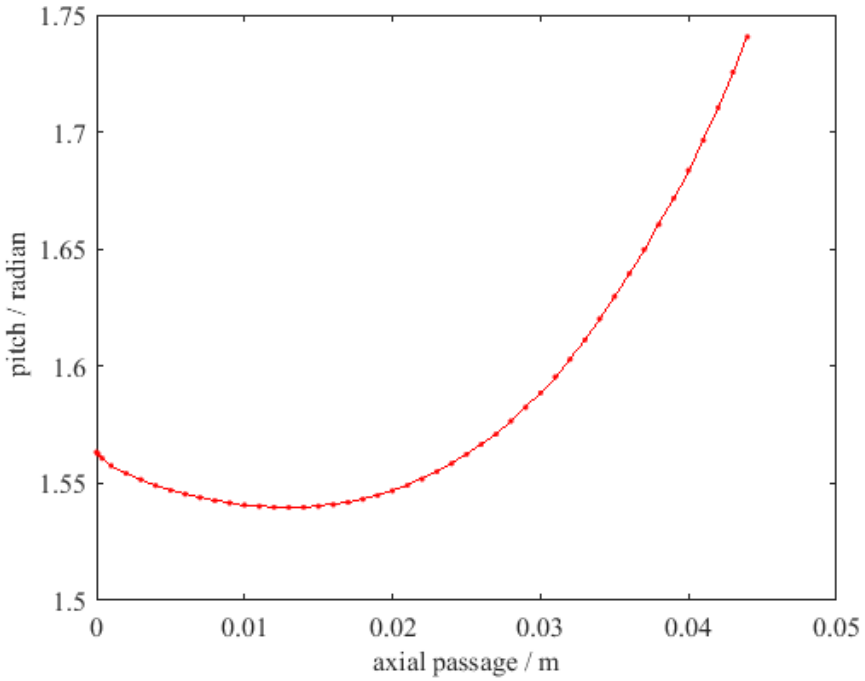

Figure 4-4: Interpolation function φ_s across the Aachen Turbine stator suction side blade coordinates.

The axisymmetric Aachen Turbine stator cylindrical hub surface was defined by the points ABCD, CDEF, and EFGH as:

For ABCD:

$$s_1(u,v) = \begin{pmatrix} (1-u)e_1 \\ r_h \cos[\theta_1(1-v) + \theta_2 v] \\ r_h \sin[\theta_1(1-v) + \theta_2 v] \end{pmatrix} \tag{4.3}$$

For EFGH:

$$s_2(u,v) = \begin{pmatrix} (1-u)e_3 + ue_4 \\ r_h \cos[\theta_3(1-v) + \theta_4 v] \\ r_h \sin[\theta_3(1-v) + \theta_4 v] \end{pmatrix} \tag{4.4}$$

For the blade passage, the pitch angle functions were defined by the interpolation functions φ_p and φ_s as:

$$\epsilon_1(u) = \varphi_p(ue_3) \tag{4.5}$$

$$\epsilon_2(u) = \varphi_s(ue_3) \tag{4.6}$$

The blade passage surface defined by points CDEF is

$$s_3(u,v) = \begin{pmatrix} ue_3 \\ r_h \cos[\epsilon_1(u)(1-v) + \epsilon_2(u)v] \\ r_h \sin[\epsilon_1(u)(1-v) + \epsilon_2(u)v] \end{pmatrix} \tag{4.7}$$

The parametric surfaces generated by MATLAB for the passage leading edge, the blade passage, and the passage trailing edge are shown in Figure 4-5, Figure 4-6, and Figure 4-7 respectively. The complete Aachen Turbine axisymmetric cylindrical hub is shown in Figure 4-8.

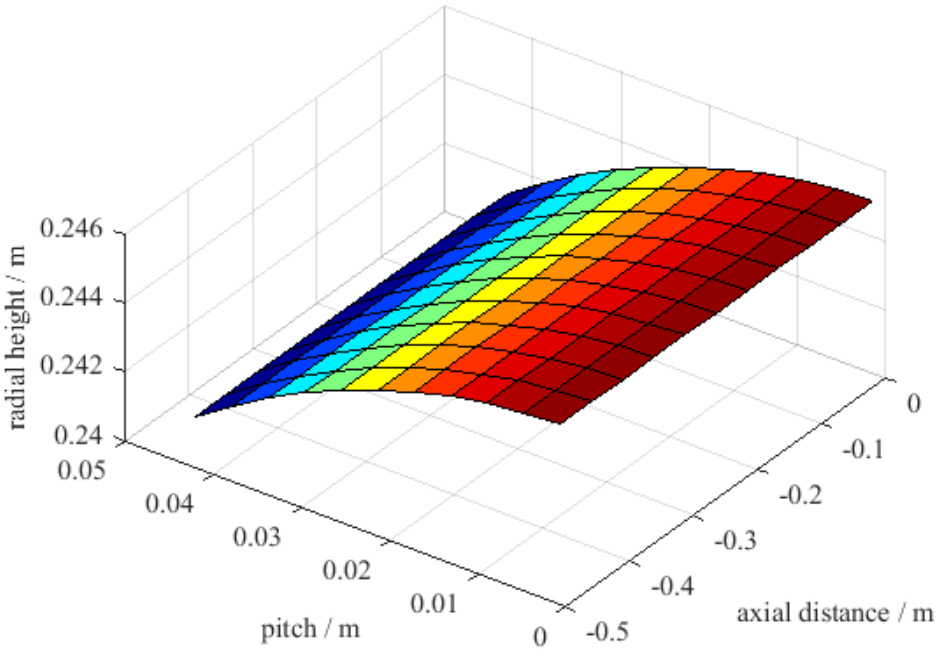

Figure 4-5: Aachen Turbine passage leading edge.

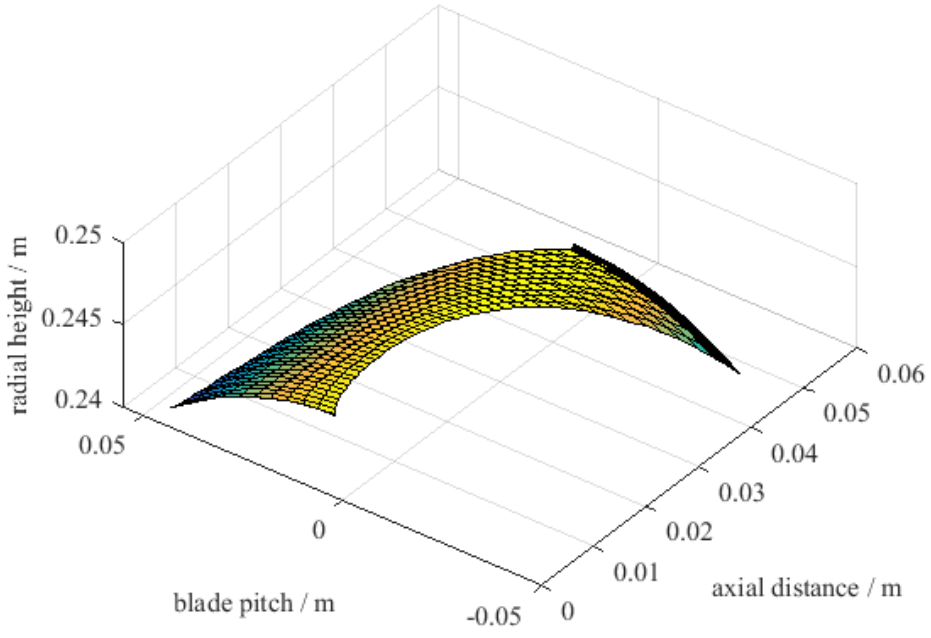

Figure 4-6: Aachen Turbine stator 1 blade passage.

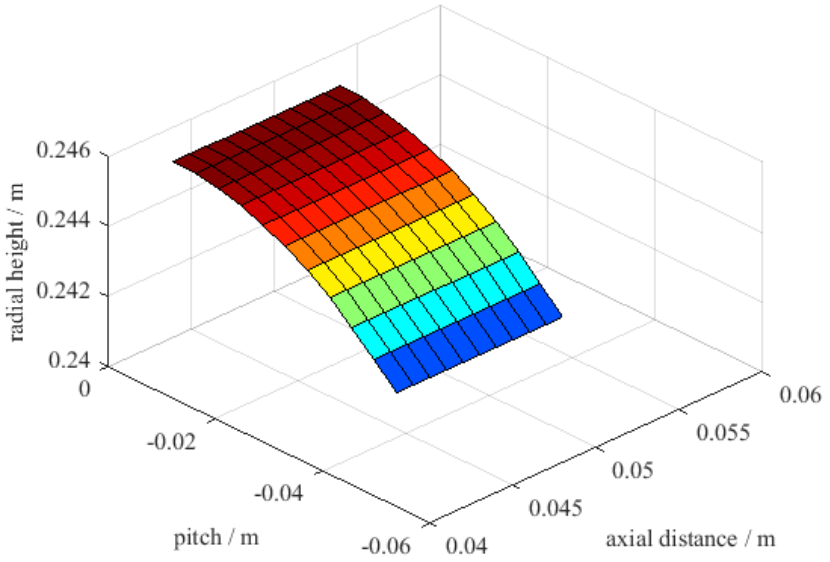

Figure 4-7: Aachen Turbine passage trailing edge.

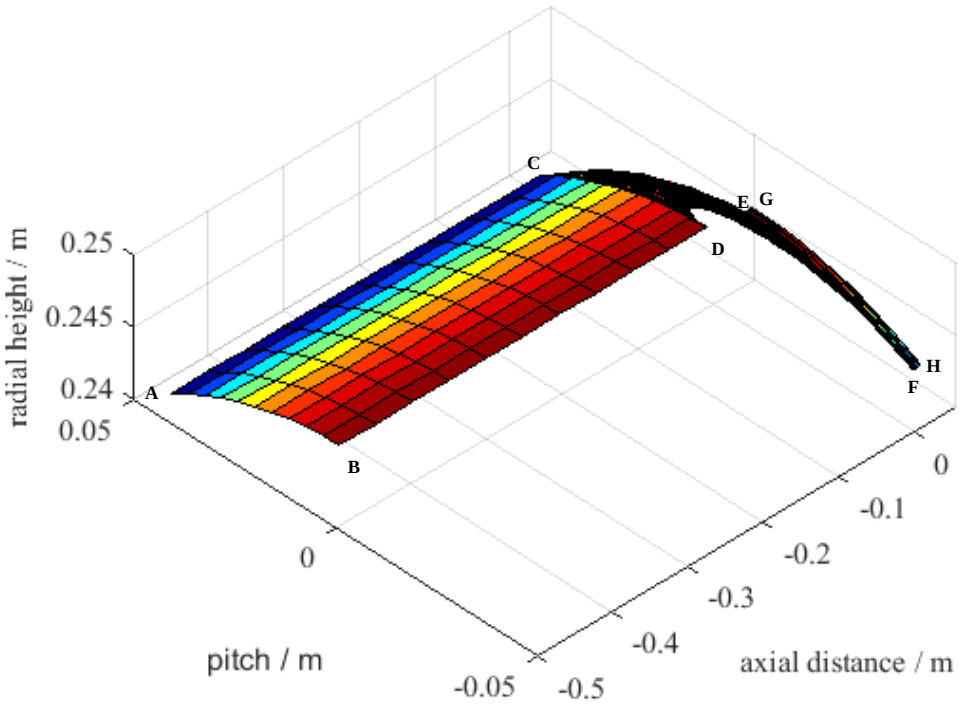

Figure 4-8 Axisymmetric hub surface of the Aachen Turbine stator passage half-stage rendered as a composite of three $s(u, v) = 0$ parametrical surfaces.

The three $s(u,v)$ parametrised surfaces were exported from MATLAB into ANSYS ICEM CFD. Three different approaches were tested for exporting each $s(u,v)$ parametrised surface from MATLAB. The first approach was to export each surface as a sampled cloud of points in Cartesian coordinates (x,y,z). ANSYS ICEM CFD imported these points and built the hub surface by interpolating through them. The second approach was to export each surface as a sampled carpet of triangles, using the Standard Triangle Language (.stl) format. An STL file describes a surface by the unit normal and vertices ordered by the right-hand rule of the triangles in the 3D Cartesian coordinate system. This type of file format is supported by ANSYS ICEM CFD. The cylindrical hub surface saved in the .stl file format was imported in ANSYS ICEM CFD as a faceted surface covering the full hub and was connected to the passage leading and trailing edges, to the pitchwise periodic boundaries, and to the blade roots without any geometry mismatch error.

The third approach was to use a NURBS surface for exporting the $s(u,v)$ parametrised cylindrical hub by rendering it in a format ANSYS ICEM CFD can read as input. Each of the three parametrised surfaces are exported as separate NURBS surfaces in ANSYS ICEM CFD. To export the $s(u,v)$ parametrised hub as a composite of three NURBS surfaces, the knots and control points of each NURBS surface were defined from the corresponding $s(u,v)$. For these NURBS surfaces, non-periodic knot vectors were used. The number of knots and of the control points on a NURBS surface are related as:

$$m = n + p_d + 1 \tag{4-8}$$

where $m+1$ are the number of knots, $n+1$ are the number of control points, and p_d is the polynomial degree of the NURBS surface which, in ANSYS ICEM CFD, is restricted to $p_d = 2$. The knot vector is defined as:

$$U_k = \{a_1, \dots, a_{p_d+1}, u_{p_d+2}, \dots, u_{m-p_d-1}, b_{m-p_d}, \dots, b_m\} \tag{4-9}$$

where $(a_1, \dots a_{p_d+1}) = 0$ and $(b_{m-p_d}, \dots, b_m) = 1$. One of the advantages of rendering the stator 1 hub by a composite of three NURBS surfaces is the ability of representing a conic section and circles exactly. To obtain a conical surface, the control points u_i, with $(p_d +$

$2) \leq i \leq (m - p_d - 1)$, are defined according to Piegl and Tiller (2012) using the parametrisation weight $w_1 = \cos(2\pi/N)$. This is a necessary and sufficient condition for the resulting surface to be geometrically an arc in the u direction of $s(u, v)$. The NURBS surfaces were exported as an IGES file, which is a supported input file format of ANSYS ICEM CFD. Each NURBS surface was saved in the IGES format as four main points, four curves, and one smooth surface. Figure 4-9 shows the top view of the stator 1 surface imported in ANSYS ICEM CFD, mated with the passage inlet hub and the passage outlet hub that were also imported as NURBS surfaces. A good contiguity between the three surfaces is shown in Figure 4-9, with no discernible gap at the stator 1 leading edge and at the stator 1 trailing edge, where the NURBS surfaces join.

The ability of using a NURBS surface to represent exactly a conical or a cylindrical surface makes this third approach attractive for turbomachinery applications in which the hub and casing are typically axisymmetric, like for the 1.5 turbine stage from RWTH Aachen. This avoids introducing uncertainties in the geometry by the application of surface interpolation techniques as it is ported from MATLAB to ANSYS ICEM CFD. For this reason, this third approach is used for the remainder of the work.

Figure 4-9: Cylindrical hub surface of the stator 1 half-stage rendered as a composite of three $s(u, v)$ parametrised surfaces imported in ICEM CFD as a composite of three NURBS surfaces.

The next step in the modelling process is to develop a variant of the stator 1 hub surfaces $s(u, v)$ that is contoured. Contouring is herein obtained by adding a groove, as shown by Figure 4-12.

The groove path is constrained to be mainly dependent on the blade profile, on the assumption that the horseshoe vortex may find easier accommodating itself into a groove with such a path and running along it. The groove path is defined with respect to the profiles of turbine blades 'inflated' in the cascade plane. This 'inflation' process consists in offsetting the blade perimeter by a set distance, normal to the blade perimeter, which is varied linearly from the stator blade leading edge, where this distance is minimum, to the stator blade trailing edge, where this distance is maximum. A linear interpolation between the 'inflated' profiles of two pitchwise consecutive blades defines the groove path as shown in Figure 4-10.

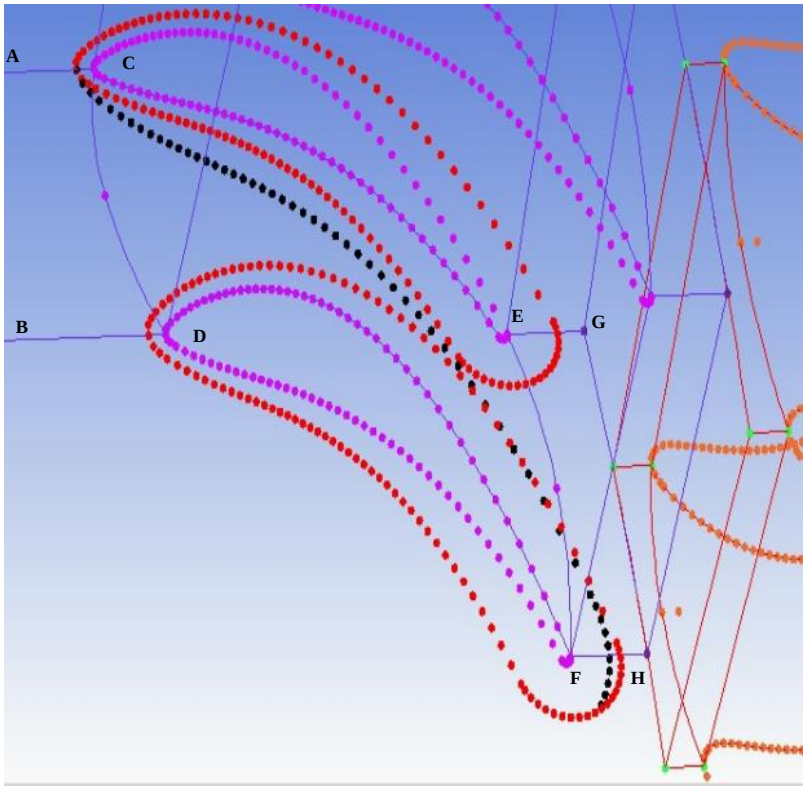

Figure 4-10: 'Inflating' the upstream stator blade profile to generate the groove path line.

The salient analytical steps of this curve path definition process are as follows: Recall that the blade profile on the cascade plane is defined by 116 points P_i. Each point P_i is allocated a corresponding point Q_i on the cascade plane offset by a user-defined offset distance b and located at:

$$Q_i = P_i + n_i b \tag{4-10}$$

where n_i is the outward normal vector to the blade perimeter. n_i is evaluated by the secant between the lines defined by (P_{i-1}, P_i) and (P_i, P_{i+1}). Two smoothing cubic splines $q_s(x)$ and $q_p(x)$ on the $r = r_h$ plane then interpolate the subset of Q_i points lying respectively on the suction side and on the pressure side of the blade. The curve path $\xi^a(x)$ is defined as the arithmetic mean of $q_s(x)$ and $q_p(x)$ from the suction side and pressure side of two pitchwise consecutive blades. For each point $P(x, \theta)$ on the $r = r_h$ plane, its normal distance to the groove path is determined as:

$$\eta(x, \theta) = FindMinValue(\| \xi^a(x) - P(x, \theta) \|) \tag{4-11}$$

The groove width d is a user-defined free parameter. The groove depth $g(d, \eta)$ is determined as

$$g(d, \eta) = -h_o \frac{(\eta^2 - d^2)^2}{d^4} \tag{4-12}$$

on the (x, θ) plane, in the area delimited by $|\eta| \leq d$. The groove depth h_o along the groove path $\xi^a(x)$ is defined using a Beta distribution function, as explained in Section 3.5.2.4. The change in the groove depth along the groove path follows one of the Beta probability density functions shown in Figure 4-11, selected by the user.

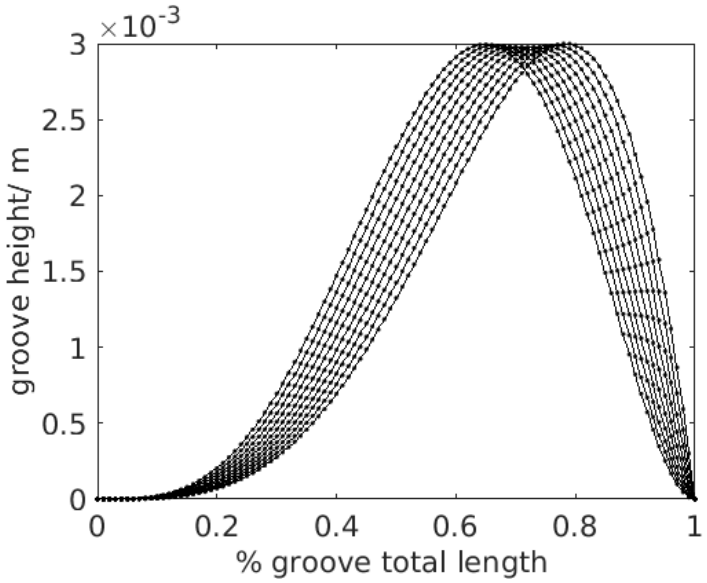

Figure 4-11: Family of Beta probability density functions obtained by prescribing the maximum groove depth position between 60% and 80% of the total groove length.

From the above, the stator 1 hub radius with groove is defined as:

$$r_{hg}(x,\theta) = \begin{Bmatrix} r_h & |\eta| > d \\ r_h + g[d,\eta(x,\theta)] & |\eta| \le d \end{Bmatrix} \tag{4-13}$$

The turbine stator 1 hub surface with groove is defined as:

$$s_c(u_s,v_s) = \left[u_s, r_{shg}(u_s,v_s)\cos(v_s), r_{shg}(u_s,v_s)\sin(v_s)\right] \tag{4-14}$$

This generalized surface is exported as a NURBS surface from MATLAB to ANSYS ICEM CFD, by an IGES file, where it is mated to the remainder of the 1.5 stage turbine domain as shown by Figure 4-12.

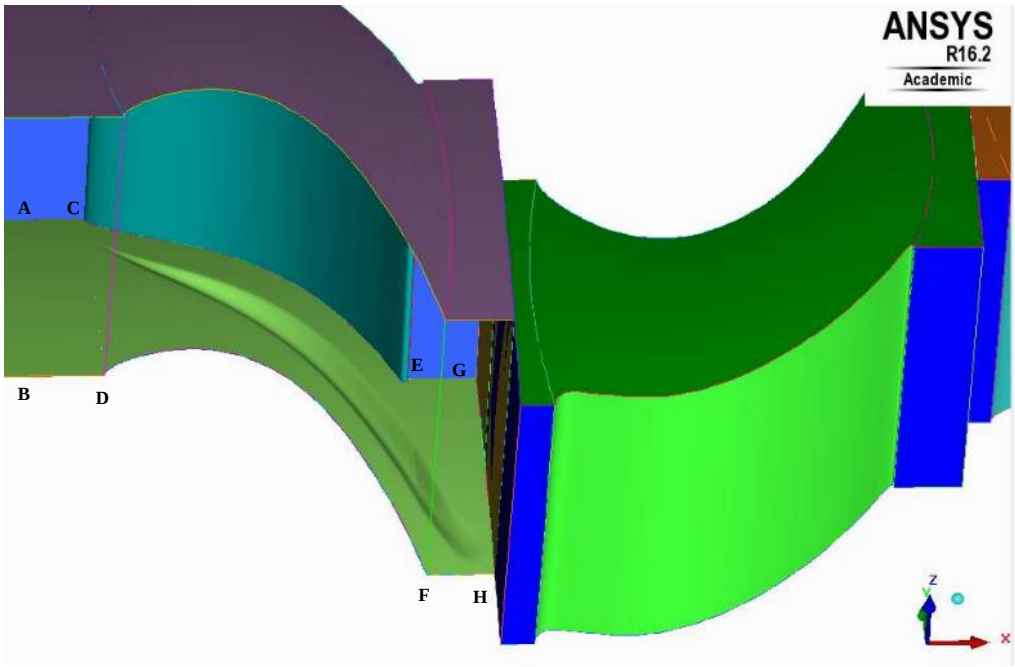

Figure 4-12: Non-axisymmetric stator 1 hub surface imported in ANSYS ICEM CFD as a NURBS surface.

4.5 Application of the Hub Contouring Technique by Praisner et al. (2013) and Kim et al. (2016) to the Upstream Hub

The contoured hub surface from Praisner et al. (2013) and Kim et al. (2016), obtained by MATLAB, is imported in ANSYS ICEM CFD as a NURBS surface. This contoured surface spans between the camber lines of two pitchwise consecutive stator 1 blades, as shown in Figure 4-13. It therefore requires trimming to confine it between the blade suction and pressure sides, so it can be mated with the remainder of the 1.5 Aachen Turbine geometry. The stator 1 blade profile is projected prismatically onto the contoured hub surface as shown in Figure 4-13. The hub surface between the blades is then trimmed along the intersection between the projected blade profile and the contoured surface, using the Segment Trim/Surface function in ANSYS ICEM CFD. This produces a hub surface spanning from the blade pressure side to the blade suction side, as shown in yellow in Figure 4-14.

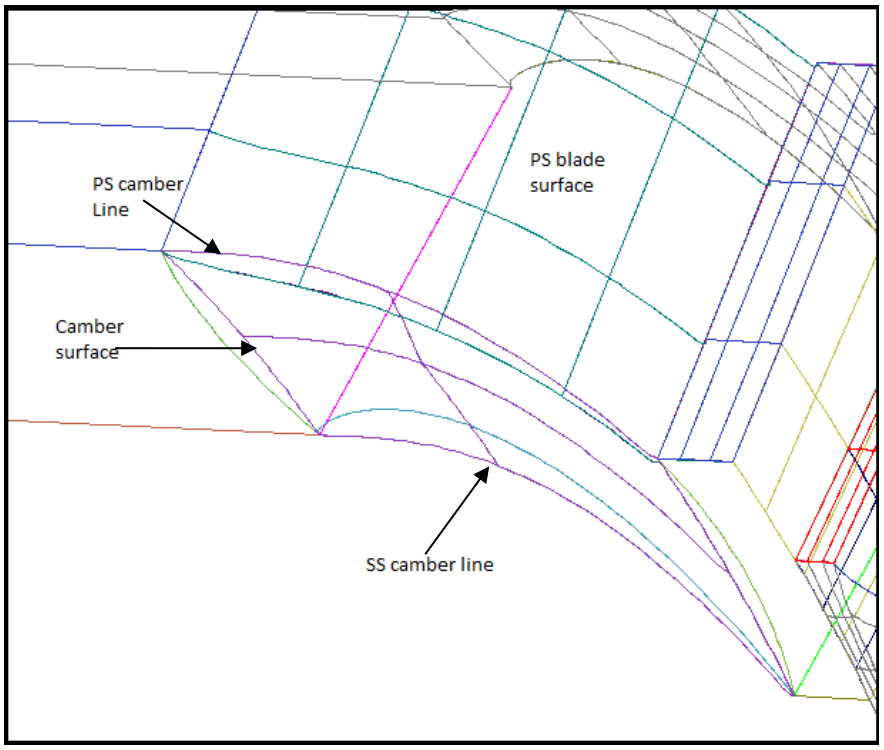

Figure 4-13: The contoured hub surface from Praisner et al. (2013) and from Kim et al. (2016) imported in ANSYS ICEM CFD as a NURBS surface.

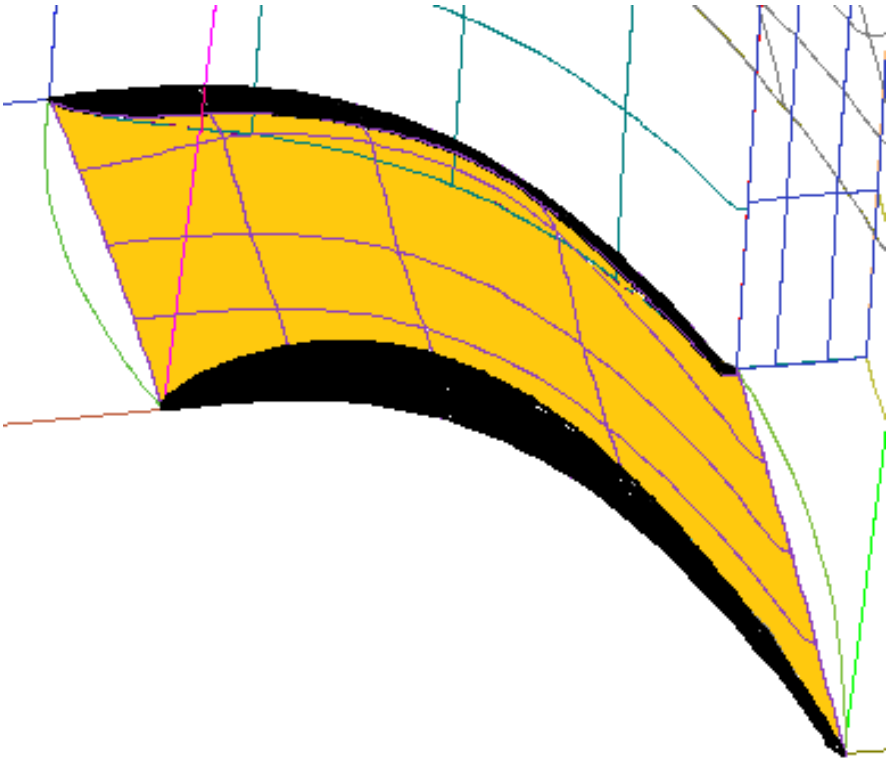

Figure 4-14: Contoured hub surface from Praisner et al. (2013) and from Kim et al. (2016) trimmed by the blade pressure side surface and the blade suction side surface.

Then, the passage leading edge hub surface and the passage trailing edge hub surface are imported as axisymmetric NURBS surfaces and are joined to the contoured hub surface between the blades. The resulting stator 1 hub with the contouring from Praisner et al. (2013) and from Kim et al. (2016) is shown in Figure 4-15.

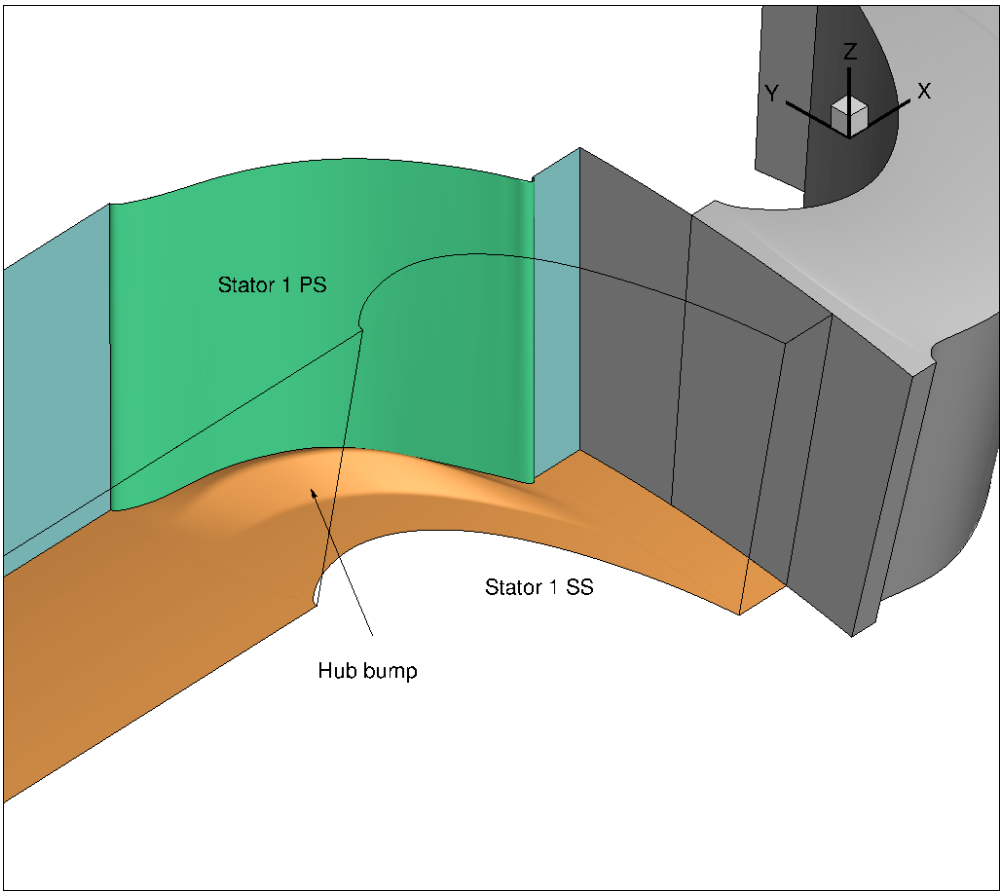

Figure 4-15: Aachen Turbine geometry with stator 1 contoured according to Praisner et al. (2013) and Kim et al. (2016).

4.6 Summary

This chapter described the process for generating a digital geometry of the 1.5 stage Aachen Turbine suitable for the computational fluid dynamics pre-processor ANSYS ICEM CFD. The first geometry that was created was that of the Aachen Turbine with an axisymmetric hub. Then, the digital geometry was altered by contouring the stator 1 hub. A contoured hub with a parametrised guide groove was defined. The guided groove parameters were the groove width at the stator 1 blade leading edge, the grove width at the stator 1 passage trailing edge, and the groove maximum depth position. The groove path was defined using an

‘inflation’ process. A second contoured hub surface was produced by implementing the method of Praisner et al. (2013) and Kim et al. (2016), for turbine performance comparison purposes. The both surfaces were created in MATLAB and exported as NURBS surfaces. These were imported in ANSYS ICEM CFD as IGES files and mated with the remainder of the Aachen Turbine geometry.

5. MODELLING END-WALL CONTOURED PASSAGES BY CFD

5.1 Introduction

This chapter describes the software chain that is used for modelling and optimising end-wall contoured passages. A CFD base flow with axisymmetric end-walls is first computed to validate the CFD component of this chain. This is obtained by discretising the geometry into an unstructured computational mesh using the commercial CFD pre-processor ANSYS ICEM CFD 18. The mesh is then exported to OpenFOAM, which solves the flow for a set of boundary conditions. Four validation cases are considered. The first one is the Aachen Turbine first stator that is modelled by OpenFOAM/2.3.0. The second, third, and fourth validation cases are the 1.5 stage Aachen Turbine tested at three different inflow/outflow conditions. The 1.5 stage Aachen Turbine is modelled by OpenFOAM/3.2-extend. This OpenFOAM version allows the use of mixing planes between the first stator and the rotor, and the rotor and the second stator. Grid independence tests are performed to determine sensitivity of the solution on the level of the computational mesh spatial refinement. Having validated the CFD model in the software tool chain, the optimisation of the hub by wall contouring is pursued. This optimisation is performed using APOW, which seeks to improve the turbine stage isentropic efficiency. The commercial software Cycle – Tempo is finally used to predict the effect of the improved turbine stage efficiency on the Coefficient Of Performance of a representative Liquefied Natural Gas (LNG) cryogenic cycle.

5.2 Computational Mesh Generation

To reduce the computational modelling effort, the flow is assumed pitchwise periodic so that only one blade pitch around the annulus is modelled, using mixing planes at the rotor-stator interfaces. This results in the flow passage geometry shown schematically in Figure 5-1 and Figure 5-2, which is decomposed in an assembly of contiguous hexahedral blocks for ease of meshing. Each block is discretized by a structured hexahedral mesh using the commercial mesh generator ANSYS ICEM CFD 18. The upstream stator near-wall mesh is designed to give a first interior cell size of $y^+ \approx 30$ in the wall-normal direction, from which the mesh is inflated using a stretching ratio of 1.05. The $y^+ \approx 30$ near-wall mesh spacing makes the process of optimising the non-axisymmetric hub surface treatable using the available computational resources. In the optimisation process, it is sufficient to determine the gradient of the penalty function rather than predicting its accurate value, for which a relatively coarse near-wall mesh is used. The mesh is first saved as an unstructured mesh in ANSYS FLUENT

format, then converted to OpenFOAM format, and finally it is imported in OpenFOAM, where it is used for obtaining a converged RANS solution of the baseline flow pattern. Details of the turbulence closure model, of the differentiation and of the numerical integration schemes used in the RANS solver are given in Section 5.3.1.

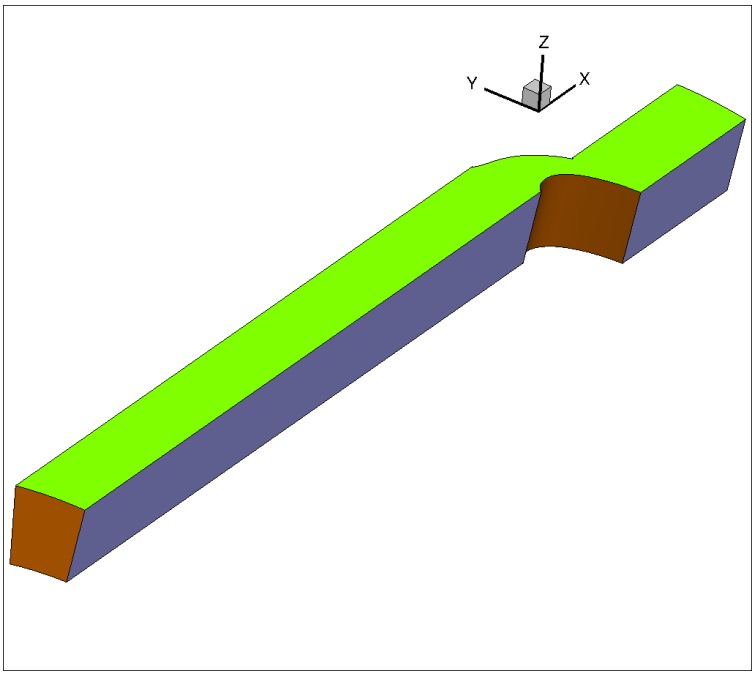

Figure 5-1: Schematic of the stator flow passage. An extended upstream bulkhead is used for growing the stage inlet boundary layers over the stator hub and casing walls. The flow runs in the positive x-direction.

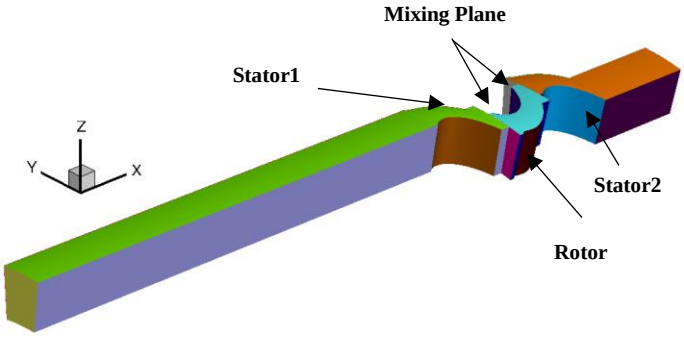

Figure 5-2: Schematic of the 1.5 stage turbine flow passage. An extended upstream bulkhead is used for developing the stage inlet boundary layers. The flow runs in the positive x-direction.

5.2.1 Turbine stator grid independence test

A grid independence test is performed with three different levels of mesh refinement. The details of these three unstructured meshes are listed in Table 5-1. The mesh quality index in all cases is 0.85. The uniformity of the mesh quality was investigated by evaluating the cell volume skewness using the normalised equiangle deviation method by Moraes et al. (2013). Figure 5-3 shows the frequency plot of the cell volume skewness, which indicates that 90% of the cell volumes have a skewness of less than 0.2. The radial profiles of circumferential velocity component and of yaw angle are selected to compare the CFD output from the three meshes. The results are shown in Figure 5-4 and Figure 5-5 respectively. The boundary conditions used are the one listed in Table 5-2 and denoted as Stator 1. This is referred to as the first validation test case, in which the turbine stator 1 modelled flow is validated against the Aachen Turbine experimental measurements.

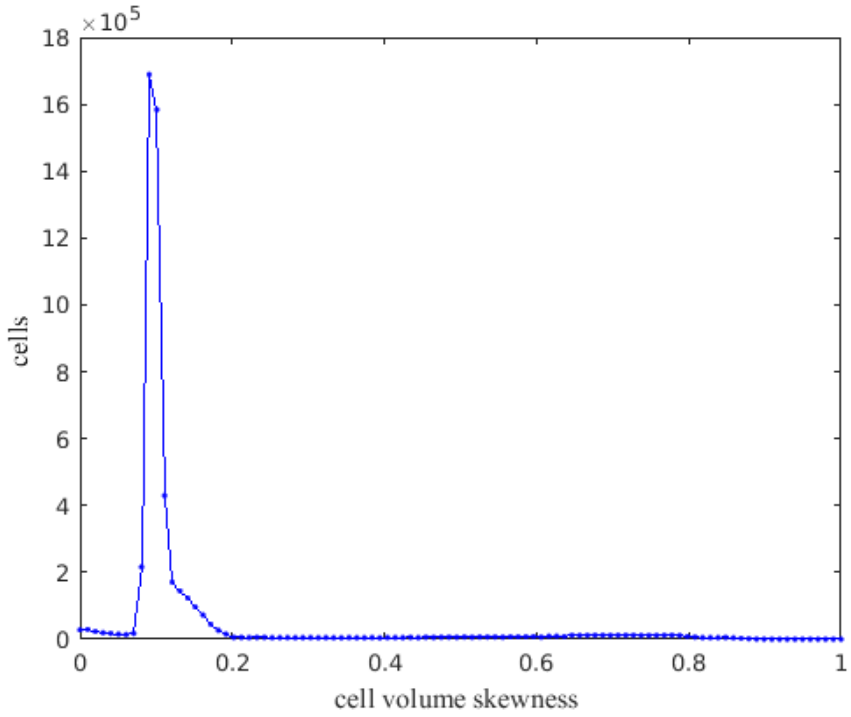

Figure 5-3: Frequency plot of cell volume skewness.

Table 5-1: Grid independence test results using three meshes of increasing spatial resolution.

Mesh type	*Nodes*	*Aspect Ratio*	*Average Circumferential Velocity*	*Average Yaw angle*
Mesh A	5,656,782	42.5	140.6915	70.11922
			(0.28988 %)	(1.86 %)
Mesh B	11,313,564	34.4	140.1354	69.8638
			(0.6839 %)	(2.22 %)
Mesh C	22,126,128	34.4	140.9426	70.12715
			(0.1119 %)	(1.85 %)

Figure 5-4 and Figure 5-5 show that the difference between meshes B and C is small compared to the difference between the coarse mesh A and the intermediate mesh B. This change with the mesh resolution gives confidence that the resolution of the intermediate mesh B is appropriate for the purposes of this study. The remainder of the CFD simulations is based on the spatial discretization of mesh B. These are shown later on Section 5.3.1.

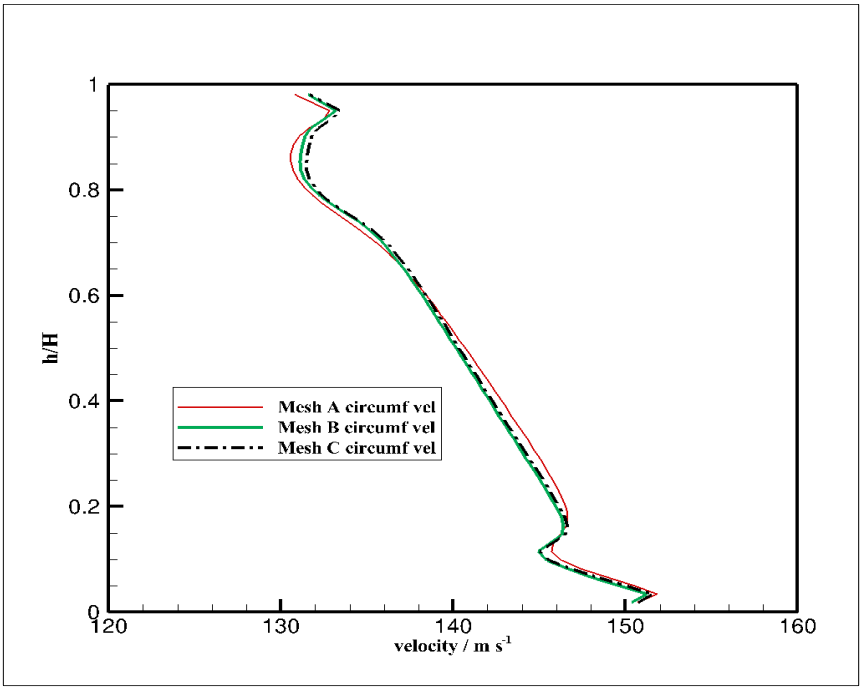

Figure 5-4: Spanwise profile of the circumferential velocity component traversed 8.8 mm chords downstream of the stator 1 trailing edge. Predictions using three progressively refined computational meshes.

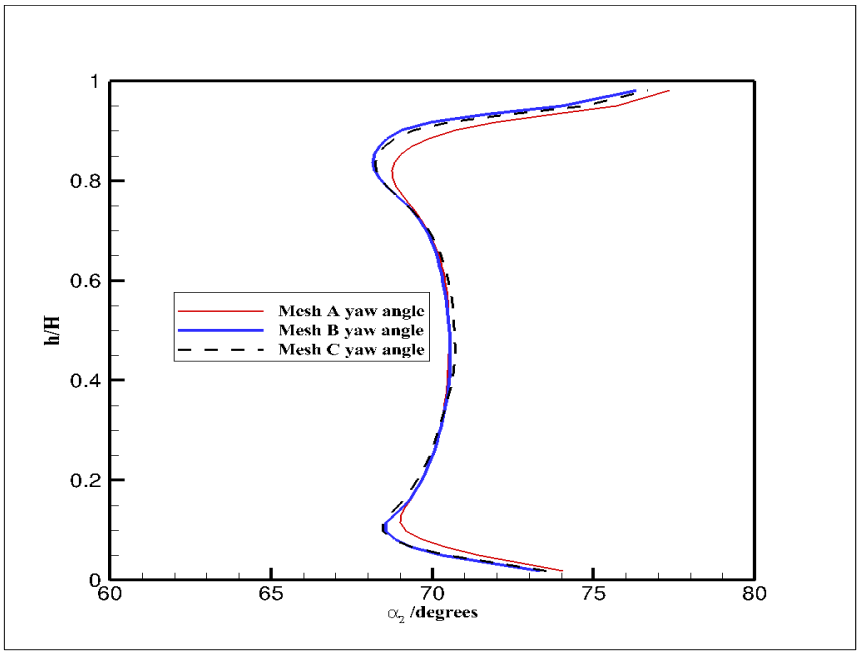

Figure 5-5: Yaw angle distribution along blade span, traversed 8.8 mm axial chords downstream of the stator 1 trailing edge. CFD predictions using three incremental levels of meshes refinement.

5.2.2 1.5 stage turbine CFD mesh convergence test

A second independent grid convergence test is performed with three different levels of mesh refinement for the 1.5 stage turbine model. The mesh quality index in all cases is 0.85. The uniformity of the mesh quality is as reported in section 5.2.1. The predicted radial profiles of the circumferential velocity component and of the meridional velocity component downstream of the rotor exit plane are shown in Figure 5-6, using progressively refined meshes, denoted as mesh A, mesh B, and mesh C. Mesh A is the coarsest mesh, with 4,007,940 nodes and an aspect ratio of 58.8. Mesh B is a mesh of intermediate spatial resolution. It is made by 8,808,228 nodes and has an aspect ratio of 41.1. Mesh C is the most spatially refined mesh. It has 19,242,318 nodes and has an aspect ratio of 27.9. The mesh-refinement ratio is 1.3 in each linear dimension.

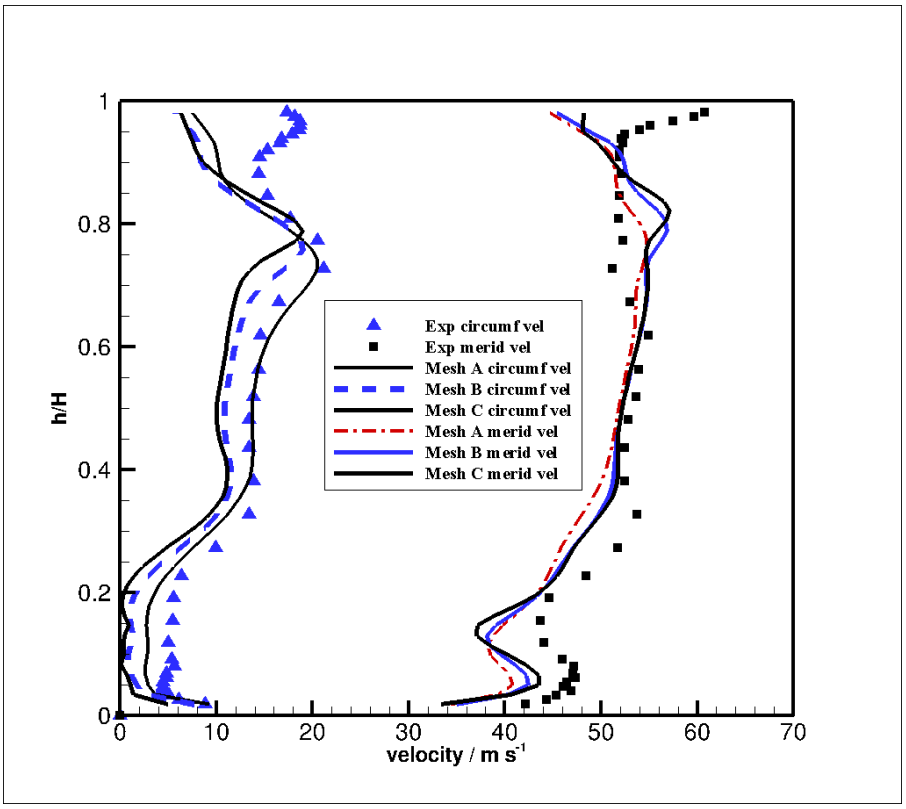

Figure 5-6: Spanwise profiles of circumferential and meridional velocity components traversed 8.8 mm downstream of the rotor trailing edge. Predictions using three progressively finer computational meshes.

Figure 5-6 shows that the discrepancy in the radial distributions of circumferential velocity obtained with mesh B and mesh C is smaller than the one between the velocity predictions obtained with the coarser mesh A and mesh B. The same trend is displayed by the predicted distributions of meridional velocity profiles 8.8 mm downstream of the rotor exit plane. This indicates qualitatively that the spatial resolution provided by mesh B is adequate for predicting the main aerodynamic performance characteristics of the 1.5 stage turbine with an appropriate mesh independence, for the purpose of the current study. This is confirmed quantitatively by computing the grid convergence index based on the circumferential velocity component at 8.8 mm downstream of the rotor exit. The grid convergence index for mesh A and B is 0.15461% while for mesh B and C is 0.35076%. The mesh convergence index gives further confidence that the spatial resolution provided by mesh B is appropriate and the remainder of the numerical predictions presented in this thesis is obtained using the spatial resolution of mesh B. The boundary conditions used for performing the grid convergence test reported in Figure 5-6 are the ones of the 'Rotor' measurements listed in Table 5-2.

Table 5-2: Boundary conditions of the validation test case.

VALIDATION TEST CASE	INLET TOTAL PRESSURE	OUTLET STATIC PRESSURE	ROTOR SHAFT SPEED
STATOR 1	152776.55 Pa	99000 Pa	3505.24 r.p.m.
ROTOR	155055.45 Pa	105000 Pa	3628.73 r.p.m.
STATOR 2	153846.05 Pa	110100 Pa	3498.24 r.p.m.

5.3 Numerical Method and Model Validation

5.3.1 Turbine stator with OpenFOAM/2.3.0

The selected structured mesh from the grid independence test is mesh type B. The mesh is imported in OpenFOAM 2.3.0 by transforming it from ANSYS FLUENT to OpenFOAM. The use of OpenFOAM instead of ANSYS FLUENT as the solver for CFD enables to increase the number of threads used in a parallel flow computation beyond 16, which is in the current limit of the ANSYS FLUENT academic license. This enables to increase the number of elements in the CFD mesh in order to improve the flow predictions. The CFD solver inside OpenFOAM/2.3.0 used in this study is rhoSimplecFoam. This was run on the University of Leicester 4800-core High Performance Computer (HPC) cluster Alice2, using Message Passing Interface (MPI) software and domain decomposition. The OpenFOAM MPI implementation enabled computations to complete within an acceptable wall time. rhoSimplecFoam is a compressible RANS flow solver based on realizable k-ε turbulent model. The inlet stator pressure boundary condition is set to total pressure with the inlet value of 152761.8625 Pa. The outlet stator pressure boundary condition is set to static pressure with the outlet value of 133793.64 Pa. These numerical inputs were converted from measurements and up to four additional figures were carried forward for numerical accuracy. The stator inlet velocity is set in the x-direction, which gives an axial inflow with the absolute inlet flow angle $\alpha_1 = 90^0$. The stator outlet velocity boundary condition is set as the InletOutlet boundary condition, which is by default zeroGradient for an outflow and changes to a fixedValue where the velocity vector direction aims inside the computational domain. The pitchwise stator boundaries are taken as a periodic rotational about the x-axis. Stationary walls for the axisymmetric hub, the casing, and the stator blades are used.

The inflow turbulence quantities were specified in terms of the turbulence intensity (I) and of the hydraulic diameter (L). Empirical correlations for fully developed pipe flow (Adebayo, 2012) estimate the turbulent intensity, the specific turbulent kinetic energy, and the dissipation rate and the specific dissipation rate of specific turbulent kinetic energy as:

$$I = 0.16(Re_L)^{-\frac{1}{8}} \tag{5.1}$$

$$k = \frac{3}{2}(U_b I)^2 \tag{5.2}$$

$$\varepsilon = C_M^{3/4} \frac{k^{3/4}}{l} \tag{5.3}$$

$$\omega = \frac{k}{\varepsilon} \tag{5.4}$$

where U_b is the bulk flow speed, C_M is equal to 0.09, and $l = 0.07\,L$ is the mixing length scale, based on the hydraulic diameter of the stator. The hydraulic diameter of the stator is estimated as:

$$L = \frac{2Hs_s}{H + s_s} \tag{5.5}$$

Where H = 55 mm is the blade span (height) and s_s = 47.6 mm is the blade spacing (pitch) at the blade mid-span. The value of the turbulence intensity estimated according to equation (5.1**)** is 0.027333. The inlet values of k and ε are 1.925203 m^2/s^2, and 131.6523 m^2/s^3, respectively. The SIMPLEC pressure-velocity coupling scheme estimates the pressure field and the velocity vector field.

The convergence criterion used in this computation is the reduction of the residuals by five orders of magnitude from their values at the start of the computation. The converged CFD solution takes 11 hours of CPU time with 50 processors. After the solution is converged, it is post-processed by OpenFOAM 2.3.0 and by Tecplot 2015 in two stages. The 3D geometry

and the flow solution in this validation were solved in Cartesian coordinates and then projected in cylindrical coordinates by post-processing. The first stage of post-processing was done inside the OpenFOAM 2.3.0 using the Sample dictionary. The Sample dictionary extracted 17 circumferential probe lines in the axial plane located at Δx_i = 8.8 mm behind the stator 1 blade trailing edges. Each probe line has 38 radial positions starting from $(y_1 , z_1) = (y_{hub} , z_{hub})$ at 246 mm radius to $(y_{38} , z_{38}) = (y_{tip} , z_{tip})$ at 299 mm as stated in Table 5-3. The 38 radial position are evenly spaced in r between (y_{hub} , z_{hub}) and (y_{tip} , z_{tip}). The change from the Cartesian coordinates to cylindrical coordinates was done by the coordinates transformation matrix:

$$\begin{bmatrix} U_x \\ U_r \\ U_\theta \end{bmatrix} = A_2 \begin{bmatrix} U_x \\ U_y \\ U_z \end{bmatrix} \tag{5.6}$$

where:

$$A_2 = \begin{bmatrix} 1 & 0 & 0 \\ 0 & \cos\theta & \sin\theta \\ 0 & -\sin\theta & \cos\theta \end{bmatrix} \tag{5.7}$$

Table 5-3: Pitchwise distribution of flow monitoring points on the axial plane 8.8 mm downstream of the turbine stator 1 blade trailing edges.

$\theta\ /\ rad$	**1**	**2**	**3**	**4**	**5**	**6**	**7**	**8**	**9**	**10**	**11**	**12**	**13**	**14**	**15**	**16**	**17**
	1.571	1.581	1.592	1.603	1.613	1.624	1.634	1.645	1.656	1.666	1.677	1.688	1.698	1.709	1.719	1.730	1.741
$y_1\ /mm$	0	-2.61	-5.22	-7.83	-10.44	-13.05	-15.65	-18.26	-20.86	-23.47	-26.06	-28.65	-31.24	-33.83	-36.41	-38.99	-41.57
$z_1\ /mm$	246	245.98	245.94	245.87	245.77	245.65	245.50	245.32	245.11	244.8	244.6	244.3	244.0	243.6	243.2	242.8	2424.6
⋮	⋮	⋮	⋮	⋮	⋮	⋮	⋮	⋮	⋮	⋮	⋮	⋮	⋮	⋮	⋮	⋮	⋮
⋮	⋮	⋮	⋮	⋮	⋮	⋮	⋮	⋮	⋮	⋮	⋮	⋮	⋮	⋮	⋮	⋮	⋮
$y_{38}\ /mm$	0	-3.17	-6.34	-9.52	-12.68	-15.85	-19.03	-22.19	-25.35	-28.52	-31.67	-34.83	-37.97	-41.12	-44.26	-47.40	-50.53
$z_{38}\ /mm$	299	298.98	298.93	298.8	298.7	298.5	298.3	291.7	297.9	297.6	297.3	296.9	296.5	296.1	295.7	295.2	294.6

Figure 5-7 and Figure 5-8 compare respectively the turbine stator 1 pitch-averaged exit velocity components and the flow angle between the experimental measurements on the Aachen Turbine stator 1 and the predications from the converged CFD solution obtained by using the unstructured mesh B. The velocity profiles show a dominant circumferential velocity component across the blade span and the end-wall boundary layer thickness is lower at the hub.

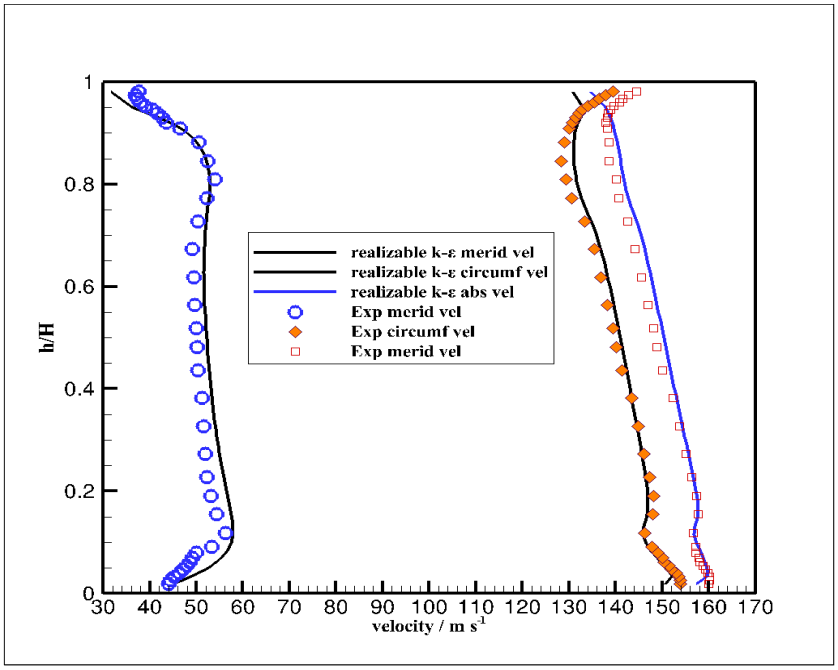

Figure 5-7: Radial distribution of meridional, circumferential, and absolute velocity components 8.8 mm behind the stator 1 blade row.

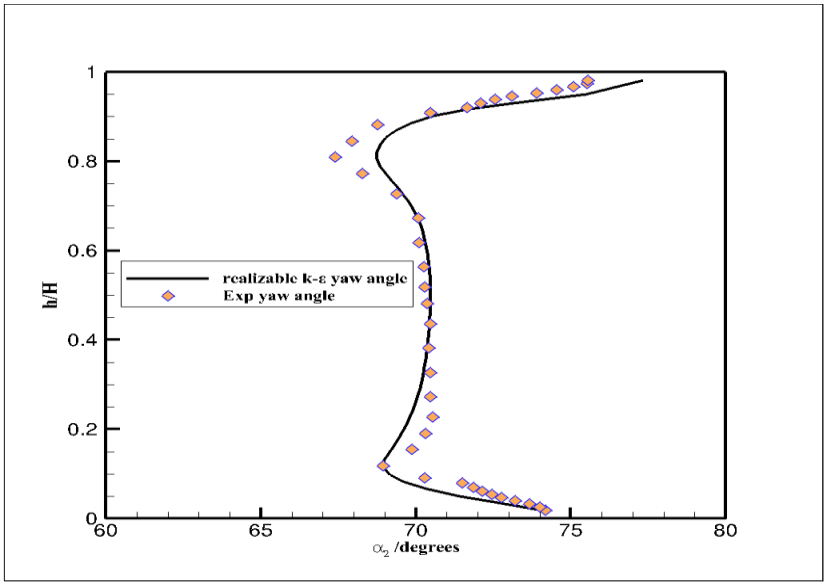

Figure 5-8: Radial distribution of yaw angle at 8.8 mm behind the stator 1 blade row.

The 1.5 stage turbine CFD model requires defining mixing planes between the stator 1 outlet and the rotor inlet and between the rotor outlet and the stator 2 inlet. OpenFOAM /2.3.0 does not include any mixing plane model. To build a full 1.5 turbine stage CFD model, OpenFoam/3.2 –extend version is used. The flow conditions across stator 1 were monitored to compare the results from OpenFOAM/3.2 against the ones from the first validation test case, which was solved by OpenFoam/2.3.0. The details are presented in the next section.

5.3.2 1.5 stage turbine with OpenFOAM-Extend/3.2

The OpenFoam-3.2-extend version software is the main CFD solver for the rest of the validation and optimisation processes. SteadyCompressibleMRFFoam is a compressible RANS flow solver inside OpenFOAM that uses the realizable k-ε and the k-ω SST turbulence closure models. Both models were tested for this simulation.

The rotor CFD model assumes a sealed rotor with zero tip gap. This is because the aim of the thesis is the optimisation of the non-axisymmetric stator 1 hub wall, which mainly affects the near-hub region. As such, the tip leakage flow is considered to be sufficiently remote not to influence significantly the loss change observed with and without the contoured hub end wall. This geometrical simplification is desirable for keeping the computational cost of modelling hub end wall modifications within the limits of the computational resources available to the author. The 1.5 turbine stage was tested in dry air, which enables modelling the flow as an ideal gas with the constant property specific heat ratio 1.4 and the specific gas constant 287 J kg^{-1} K^{-1}. The computational domain inlet upstream of the first stator row is set as a total pressure boundary condition. The computational domain outlet downstream of the second stator row is defined as a static pressure boundary condition. At the computational domain inlet, the velocity is set in the x-direction to give an axial inflow and an absolute inlet flow angle $\alpha_1 = 90°$. Figure 5-9 shows the radial distributions of the meridional velocity component 143 mm upstream of the stator 1 blade row. The velocity distributions obtained from both the realizable k-ε and the k-ω SST turbulence closure models show a good agreement with the experimental measurements from RWTH Aachen Turbine. The passage inflow boundary layer is clearly shown in Figure 5-9 over the height fraction range $0.018 \leq h/H \leq 0.165$ near the hub and $0.84 \leq h/H \leq 0.98$ near the tip.

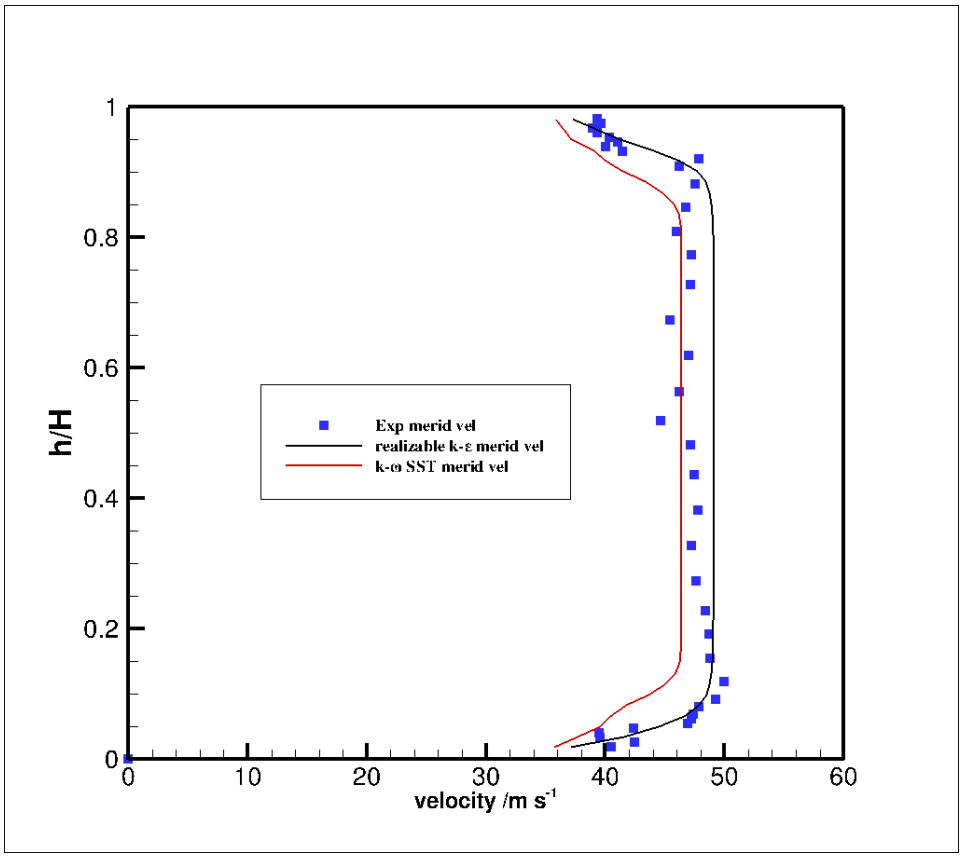

Figure 5-9: Radial distribution of meridional velocity component 143 mm upstream of the stator 1 blade row

The computational domain outlet velocity is set as the OpenFOAM InletOutlet boundary condition, which is by default zeroGradient. The pitchwise boundaries upstream of the first stator, downstream of the second rotor, and between blade rows are taken as a rotational periodic about the x-axis. Stationary walls for the axisymmetric hub, the casing, and the stator blades are used. The rotor blades are modelled as walls that are stationary in the rotor frame of reference, which rotates at the rotor shaft speed. Mixing planes are defined between the outlet of the first stator and the inlet of the rotor, 10 mm downstream of the stator exit, and also between the outlet of the rotor and the inlet of the second stator, 10 mm downstream of the rotor exit (Jasak and Beaudoin, 2011). At each mixing plane, the flow is averaged in the pitchwise direction according to Beaudoin et al. (2014). Area averages of the pressure, of the specific kinetic energy, of the specific kinetic energy dissipation rate, and of the temperature are performed over circumferential rings one unit cell wide in the radial direction. The mixing planes are located closer to the downstream blade row to enable the monitoring of the exit flow at the same axial location as at RWTH Aachen.

Measurements are reported in the RWTH Aachen validation data from three experiments, documenting respectively the first stator, rotor, and the second stator exit flow. Small changes in the ambient conditions and in the rig set-up resulted in three different sets of the inlet total pressure, rotor speed, and exit pressure recorded in experiment. Each experiment therefore provides a separate validation test case for the CFD model. The boundary conditions of the validation test cases are listed in Table 5-2.

The CFD solutions for the validation test case, converged to 10^{-5} of the initial value of the residuals, typically take 10 hours of computer wall time with 50 HPC cores. After the solution is converged, it is analysed using the OpenFOAM 2.3.0 post-processing tools and rendered graphically by Tecplot 2015. The 3D geometry and the flow solution, which are defined in Cartesian coordinates, are projected in cylindrical coordinates by the Sample dictionary of OpenFOAM 2.3.0. The Sample dictionary allows exporting 17 circumferential probe lines in the axial plane located 8.8 mm behind the stator 1 trailing edges. Two additional identical sets of probe lines are exported at the same axial distance of 8.8 mm, respectively behind the rotor trailing edges and behind the stator 2 trailing edges. Each probe line has 38 radial positions, ranging from 246 mm radius to 299 mm radius as stated in Table 5-4 and Table 5-5 respectively.

The first validation test case is Stator 1. Both the realizable k-ε turbulence model and k-ω SST model showed good agreement in the predicted circumferential, meridional, and absolute velocity components with corresponding experimental measurements from RWTH downstream of the stator 1, as in the OpenFoam/2.3.0 simulation. These results are shown in Figure 5-10. The same trend is shown in Figure 5-11 for the predicted yaw angle downstream of the stator 1.

Table 5-4: Pitchwise distribution of flow monitoring points on the axial plane 8.8 mm downstream of the turbine rotor blade trailing edges.

$\theta\ /\ rad$	**1**	**2**	**3**	**4**	**5**	**6**	**7**	**8**	**9**	**10**	**11**	**12**	**13**	**14**	**15**	**16**	**17**
	1.524	1.533	1.543	1.552	1.561	1.571	1.583	1.589	1.599	1.608	1.618	1.627	1.636	1.646	1.655	1.664	1.673
$y_1\ /mm$	11.50	9.20	6.90	4.60	2.30	0.01	-2.95	-4.59	-6.89	-9.19	-11.49	-13.79	-16.08	-18.38	-20.67	-22.96	-25.20
$z_1\ /mm$	245.70	245.80	245.87	245.93	245.96	245.97	245.96	245.93	245.87	245.80	245.70	245.58	245.44	245.28	245.10	244.90	244.67
⋮	⋮	⋮	⋮	⋮	⋮	⋮	⋮	⋮	⋮	⋮	⋮	⋮	⋮	⋮	⋮	⋮	⋮
⋮	⋮	⋮	⋮	⋮	⋮	⋮	⋮	⋮	⋮	⋮	⋮	⋮	⋮	⋮	⋮	⋮	⋮
$y_{38}\ /mm$	7.47	4.67	1.88	-0.92	-3.71	-6.51	-9.30	-12.10	-14.89	-17.68	-20.47	-23.26	-26.05	-28.83	-31.61	-34.39	-37.00
$z_{38}\ /mm$	298.91	298.96	298.99	299.00	298.98	298.93	298.86	298.76	298.63	298.48	298.30	298.09	297.86	297.61	297.32	297.02	296.68

Table 5-5: Pitchwise distribution of flow monitoring points on the axial plane 8.8 mm downstream of the turbine stator 2 blade trailing edges.

$\theta\ /\ rad$	**1**	**2**	**3**	**4**	**5**	**6**	**7**	**8**	**9**	**10**	**11**	**12**	**13**	**14**	**15**	**16**	**17**
	1.624	1.633	1.644	1.655	1.665	1.676	1.687	1.697	1.708	1.718	1.729	1.740	1.750	1.761	1.771	1.782	1.793
$y_1\ /mm$	-12.98	-15.43	-18.04	-20.65	-23.25	-25.85	-28.45	-31.05	-33.64	-36.23	-38.81	-41.39	-43.96	-46.53	-49.10	-51.66	-54.21
$z_1\ /mm$	246.00	245.85	245.67	245.47	245.23	244.97	244.69	244.37	244.03	243.66	243.26	242.83	242.38	241.90	241.39	240.86	240.29
⋮	⋮	⋮	⋮	⋮	⋮	⋮	⋮	⋮	⋮	⋮	⋮	⋮	⋮	⋮	⋮	⋮	⋮
⋮	⋮	⋮	⋮	⋮	⋮	⋮	⋮	⋮	⋮	⋮	⋮	⋮	⋮	⋮	⋮	⋮	⋮
$y_{38}\ /mm$	-15.70	-18.87	-22.04	-25.21	-28.38	-31.54	-34.70	-37.85	-41.00	-44.15	-47.29	50.42	-53.55	-56.68	-59.79	-62.90	-65.90
$z_{38}\ /mm$	299.00	298.82	298.60	298.35	298.06	297.75	297.39	297.01	296.59	296.14	295.65	295.14	294.58	294.00	293.38	292.73	292.05

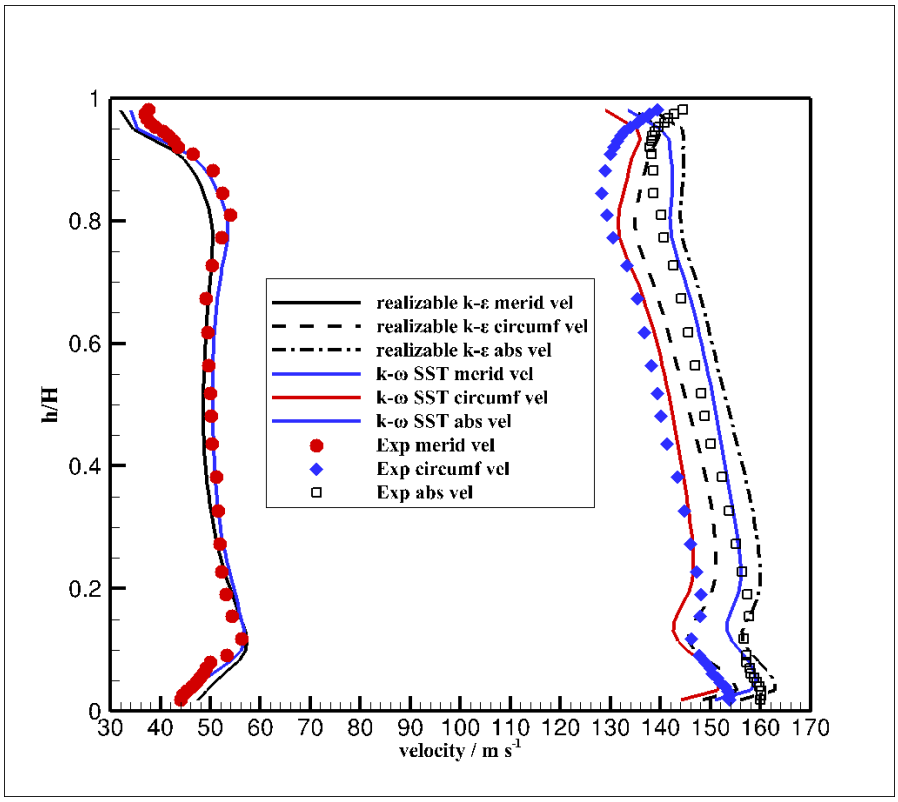

Figure 5-10: Radial distribution of meridional, circumferential, and absolute velocity components 8.8 mm behind the stator 1 blade row.

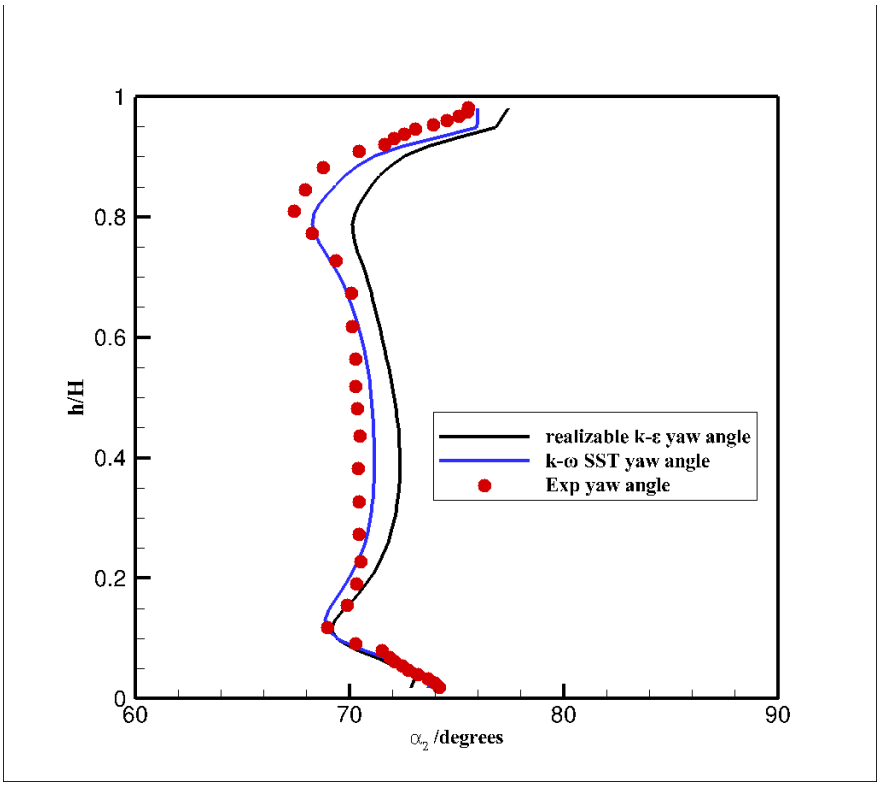

Figure 5-11: Radial distribution of yaw angle 8.8 mm behind the stator 1 blade row.

The second validation test case described in this section is the Rotor case. The $k-\omega$ SST model showed a better agreement with experiment for the rotor exit flow than the realizable $k-\varepsilon$ turbulence model, as shown in Figure 5-12 and Figure 5-13. Figure 5-12 and Figure 5-13 compare respectively the pitch-averaged rotor exit velocity components and the flow angle between the measurements from RWTH Aachen and the predications from the converged CFD solution. The velocity profiles show a dominant circumferential velocity component across the blade span. In the experiment, the end wall boundary layer thickness is lower at the hub than at the casing. In the simulation, the rotor tip leakage flow is not resolved as the rotor is modelled with zero tip clearance. This simplification leads to different velocity and yaw angle trends between experiment and computation over the blade height fraction range $0.9 \leq h/H \leq 1$, close to the casing. As this thesis focuses on evaluating a new end wall contouring technique at the hub, which mainly affects the near-hub region, the tip leakage flow is considered sufficiently remote not to influence significantly the loss change observed with and without the contoured hub end wall. A similar difference in trends between the measured and modelled yaw angle distributions is observed in Figure 5-13.

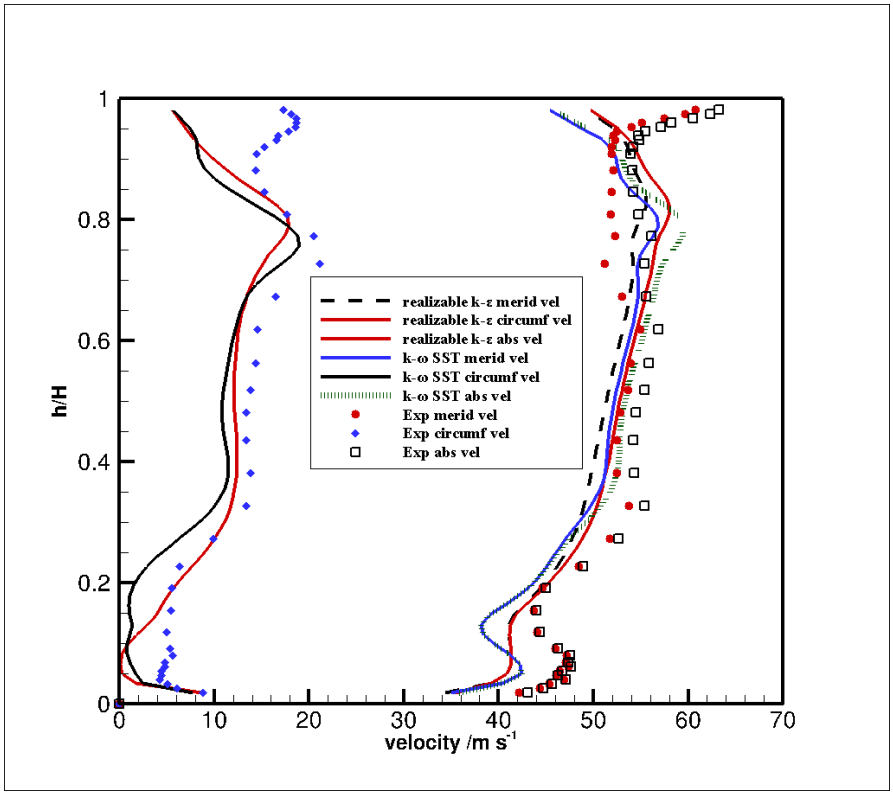

Figure 5-12: Radial distribution of meridional, circumferential, and absolute velocity components 8.8 mm behind the rotor blade row.

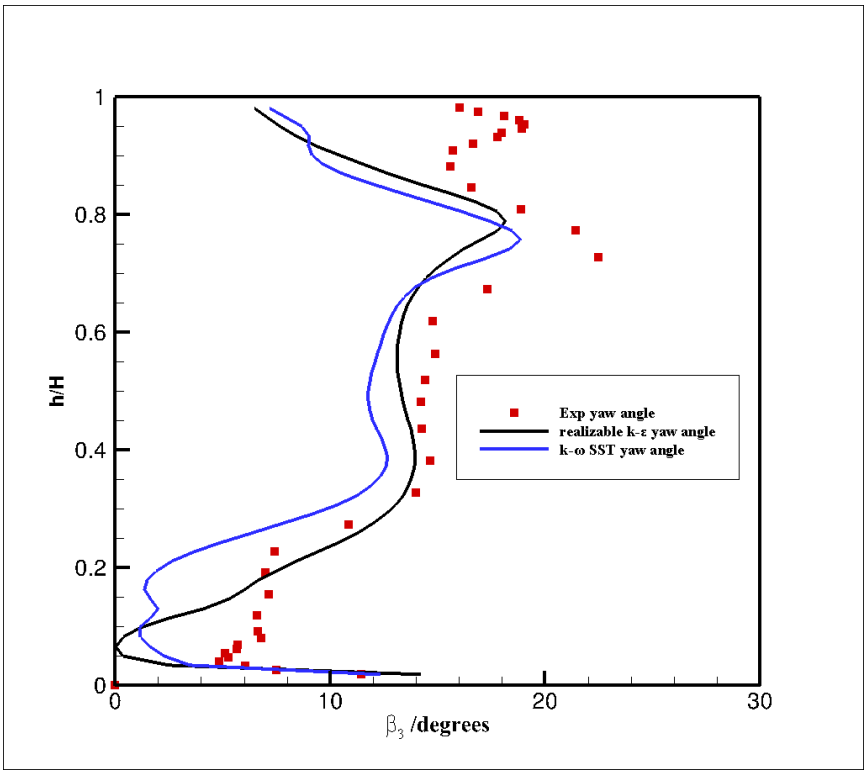

Figure 5-13: Radial distribution of yaw angle at 8.8 mm behind the rotor blade row.

The third validation test case in this section is the Stator 2 case. Figure 5-14 and Figure 5-15 compare the predicted stator 2 downstream velocity components and the yaw angle against the corresponding experimental data from RWTH Aachen Turbine. The *k*-ω SST model show a better agreement with experiment for the stator 2 exit flow rather than the realizable *k*-ε turbulence model. The remainder of the CFD simulations will therefore be performed with the *k*-ω SST model. The optimisation task uses the Rotor validation test case as the baseline flow prediction. From this, it computes the stage pressure loss and the stage isentropic efficiency with different hub geometries.

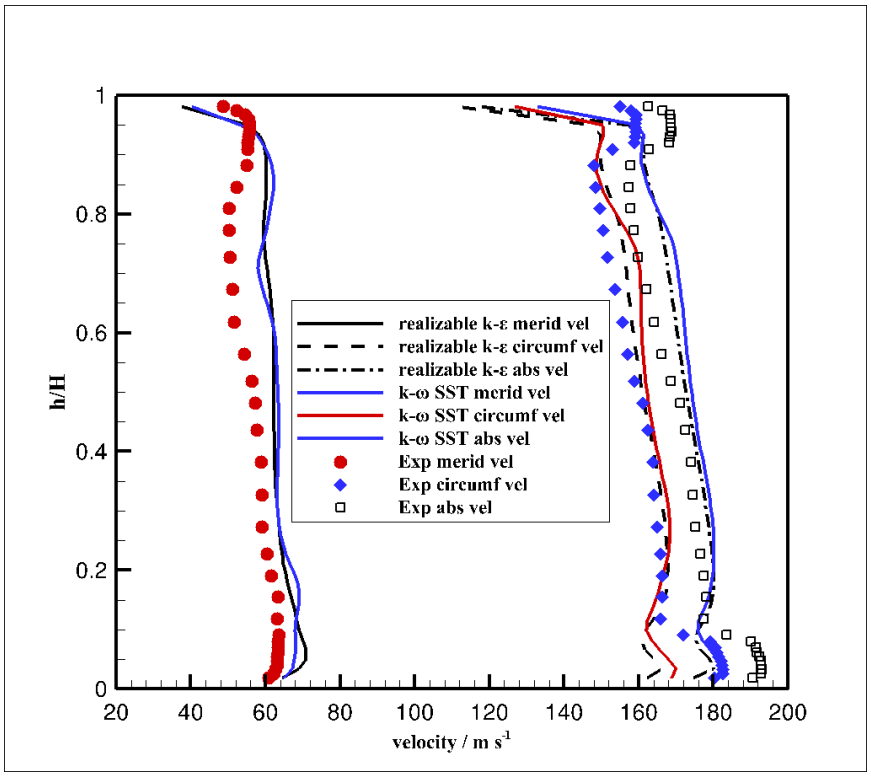

Figure 5-14: Radial distribution of meridional, circumferential, and absolute velocity components 8.8 mm behind the stator 2 blade row.

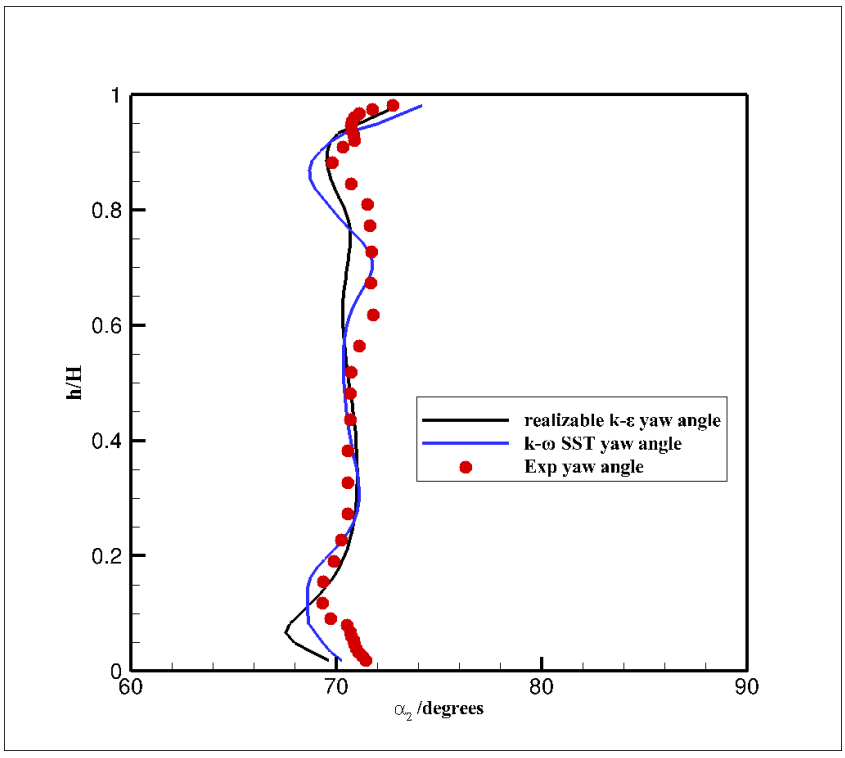

Figure 5-15: Radial distribution of yaw angle at 8.8 mm behind the stator 2 blade row.

Notwithstanding the difference between the experiment and the computation close to the casing, Figure 5-12 and Figure 5-13 show that the experimental and the numerical profiles both display a central region, about the blade mid-height, where the velocity and the yaw angle change slowly with the radial distance. This is located between near-casing and near-hub regions that feature larger radial gradients in velocity and in yaw angle. This is suggestive of a more complex flow pattern developing through the 1.5 stage turbine along the hub. To investigate this inference, limit streamlines were generated from the numerical solution over the hub, approaching the upstream stator blade leading edge, in the area indicated by the inset on the top left of Figure 5-16.

Figure 5-16 shows these near-surface limit streamlines together with iso-colour levels of the axial velocity component. These streamlines are broadly equivalent to a surface (oil) flow visualisation in an experiment. The streamlines show that the boundary layer, which grows along the 486 mm long passage leading edge, approaches the stator 1 blade towards the leading edge pressure side, in the direction indicated by the arrows on the bottom left of Figure 5-16. The boundary layer separates before it reaches the blade surface, as indicated by the cruciform saddle point of streamlines centred approximately at $x = -0.0008$ mm and $y = 0.0412$ mm. The boundary layer separation line is the vertical branch of the cluster of streamlines stemming from the cruciform saddle point. Downstream of this line, the boundary layer rolls up, forming a horseshoe vortex that wraps around the blade leading edge. The downstream trajectories of the horseshoe vortex pressure side and suction side branches are shown in Figure 5-17, by near-surface ribbons through the stator vane passage. The ribbons show that, whereas the suction side branch of the horseshoe vortex runs tightly around the blade suction surface, the pressure side branch moves across towards the suction side, driven by the pitchwise pressure gradient. The two branches combine from about 0.5 axial chords downstream of the blade leading edge, forming a larger structure, denoted as the passage vortex. The passage vortex is shown in Figure 5-17 to lift off the hub surface and move progressively towards the blade mid-height with increasing axial distance. The passage vortex, by size and position, appears to affect a larger area of the main passage flow than the individual branches of the horseshoe vortex.

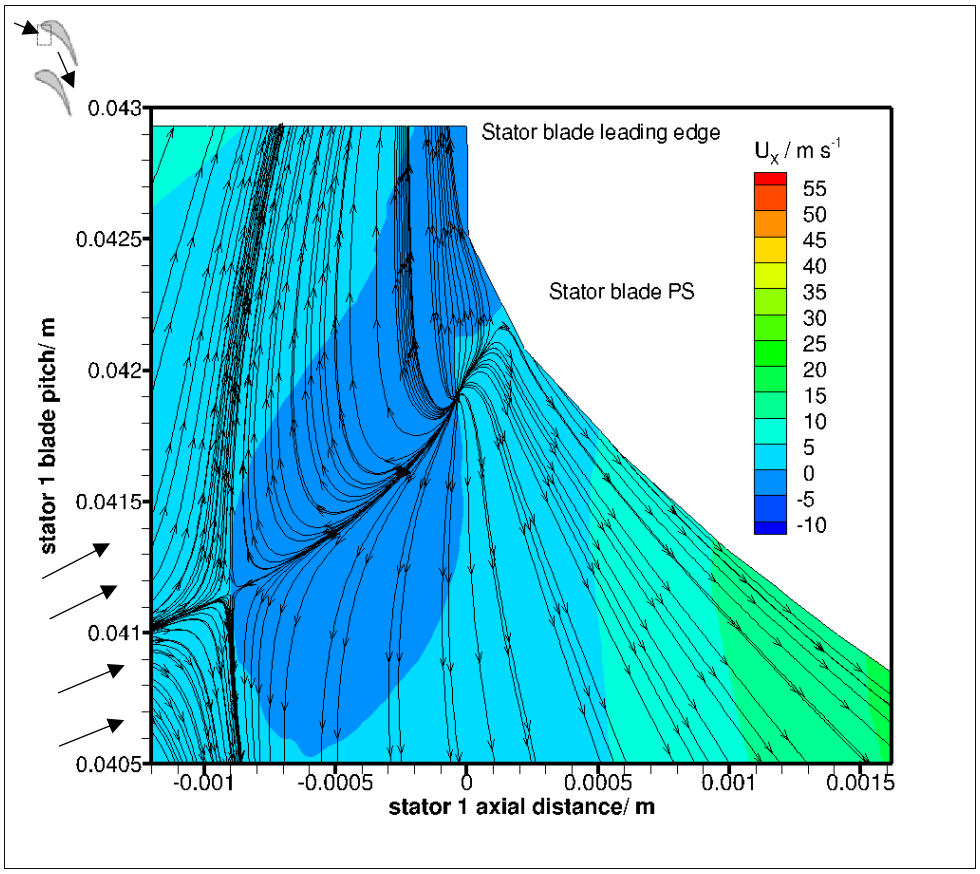

Figure 5-16: Flow visualisation near the stator blade pressure side leading edge showing the separation of the oncoming hub wall boundary layer on approach to the blade.

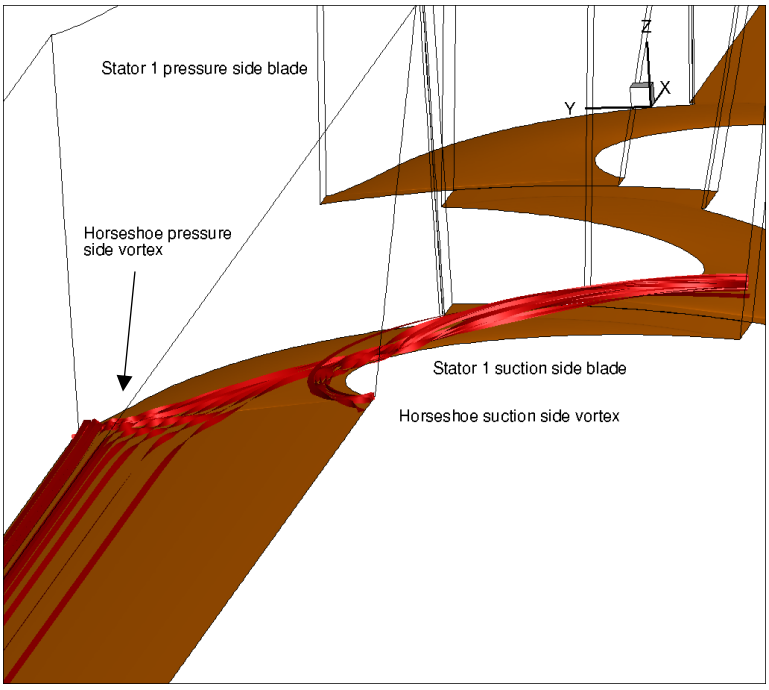

Figure 5-17: Flow visualisation over the stator 1 axisymmetric hub showing by the ribbons the horseshoe vortex pressure side branch combining with its suction side branch.

At the casing, the pattern of secondary flows described in Figure 5-16 and Figure 5-17 is essentially repeated, mirrored about the blade mid-height. These vortices are shown at the turbine stator 1 blade suction side near hub and tip in Figure 5-18.

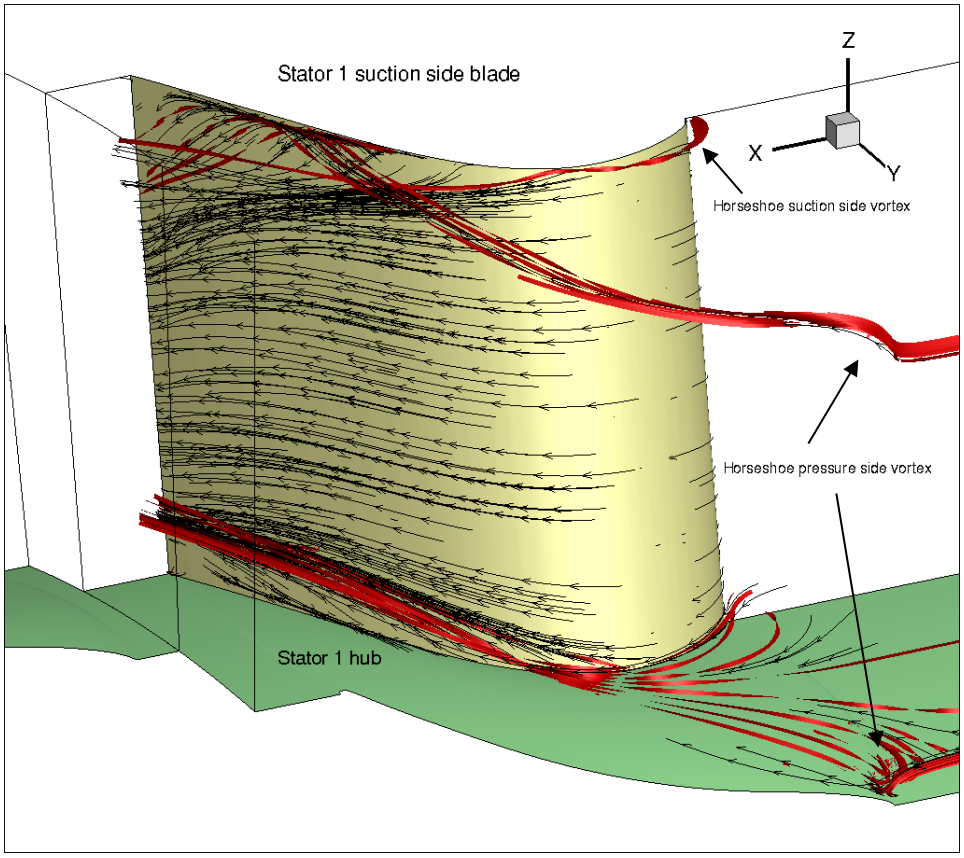

Figure 5-18: Flow visualisation over the stator 1 blade suction side showing by the ribbons and streamlines the horseshoe vortex pressure side branch combining with its suction side branch, on the hub (bottom) and on the casing (top).

The main aim of the thesis is to reduce the total pressure loss that results from these secondary flows. This is pursued by delaying the merger between the suction and pressure sides of the horseshoe vortex over the hub, by introducing a non-axisymmetric stator hub as shown in Figure 4-12. The non-axisymmetric hub is characterized by a groove running between the stator 1 blades. The hub groove starts from the turbine stator 1 blade leading edge and ends at the turbine stator 1 passage trailing edge, where the end wall regains its axial symmetry. The end-wall groove aims to guide the horseshoe vortex pressure side branch farther away from the blade suction side and thereby reduce the secondary flow losses.

5.4 Optimisation of the Grooved Hub Geometry with APOW

A non-axisymmetric hub is designed by cutting a groove through the passage running from the stator 1 leading edge to the stator 1 passage trailing edge. The workflow for designing the non-axisymmetric hub is created in the Alstom Process and Optimisation Workbench (APOW) software environment, available through the industrial partner GE. This workflow is shown in Figure 5-19. APOW includes the Optimal Latin Hypercube method for the designing of experiments (DoE) with a well-sampled parameter space. The hub groove is optimised on three free parameters, which are the groove width at the stator 1 blade leading edge, d_{le}, the position of the maximum groove depth, h_o, and the groove width at the stator 1 passage trailing edge, d_{te}. Two optimisation tasks are defined to permute among the three parameters. In each task, two parameters in the optimiser are changed and the third parameter is kept constant, as shown in Figure 5-20. The object of the optimisation is the stage total pressure loss coefficient, which is the cost function that is minimized.

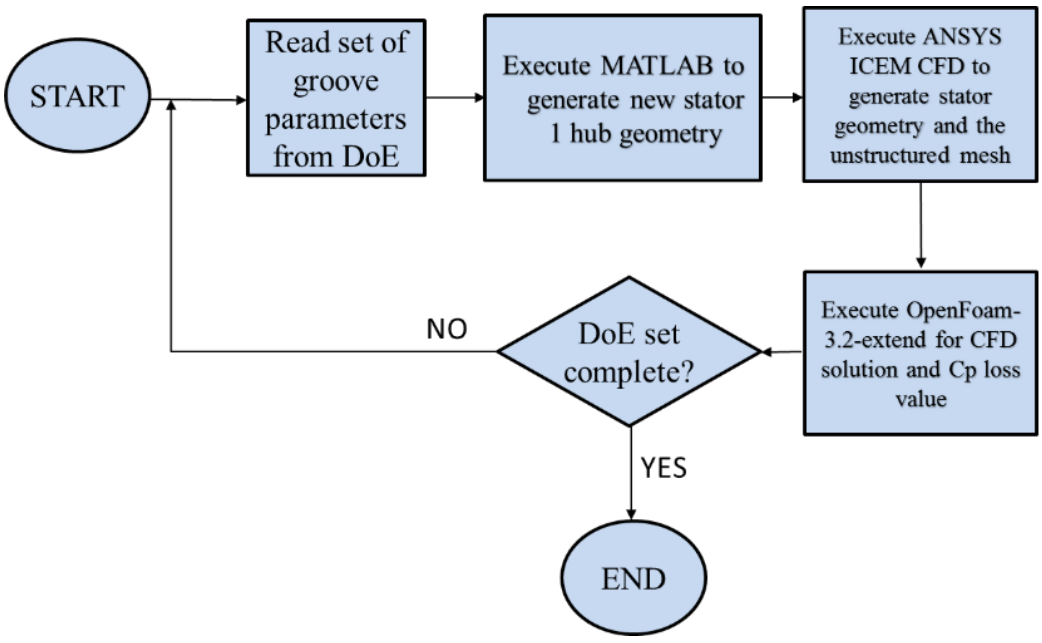

Figure 5-19: APOW flow diagram.

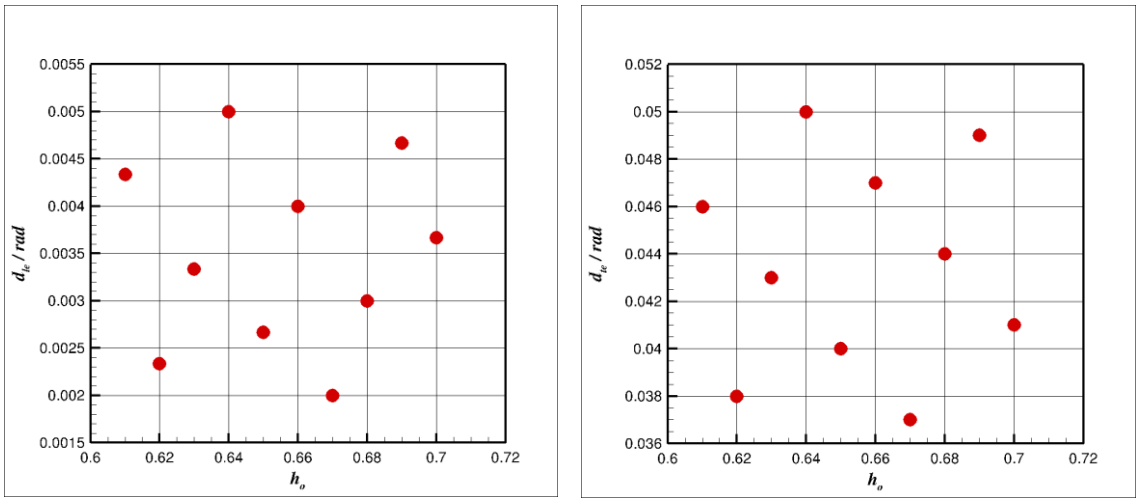

(a) (b)

Figure 5-20: (a) DoE for optimisation task one. (b) DoE for optimisation task two.

The first step of the workflow entails loading a fresh set of groove parameters from the DoE matrix. In the second step, MATLAB is used to translate these parameters into a parametrised stator 1 hub surface $s(u_s, v_s)$ for the Aachen Turbine, as a continuous function in $\mathbb{R}3$, where s designates stator 1. The corresponding contoured hub surface with groove is then defined by the procedure in Section 4.4.

The contoured variant s_c of the parameterised hub surface $s(u_s, v_s)$ is exported as three non-uniform rational B-spline (NURBS) surfaces without any additional surface re-approximation. These are imported directly in ANSYS ICEM CFD via an IGES file. There, they are mated to the remainder of the 1.5 stage turbine domain as shown by Figure 5-21. The three surfaces are labelled ABCD, CDEF, and EFGH in Figure 4-9.

The third step in the APOW workflow uses the mated domain with the grooved hub and generates/re-generates a computational mesh by ANSYS ICEM CFD, saving it as an ANSYS FLUENT unstructured mesh. The fourth step changes the format of the mesh from ANSYS FLUENT to OpenFOAM, applies the boundary conditions, solves the flow by OpenFOAM 3.2-extend to a converged solution, and finally post-processes the solution to compute the stage total pressure loss coefficient.

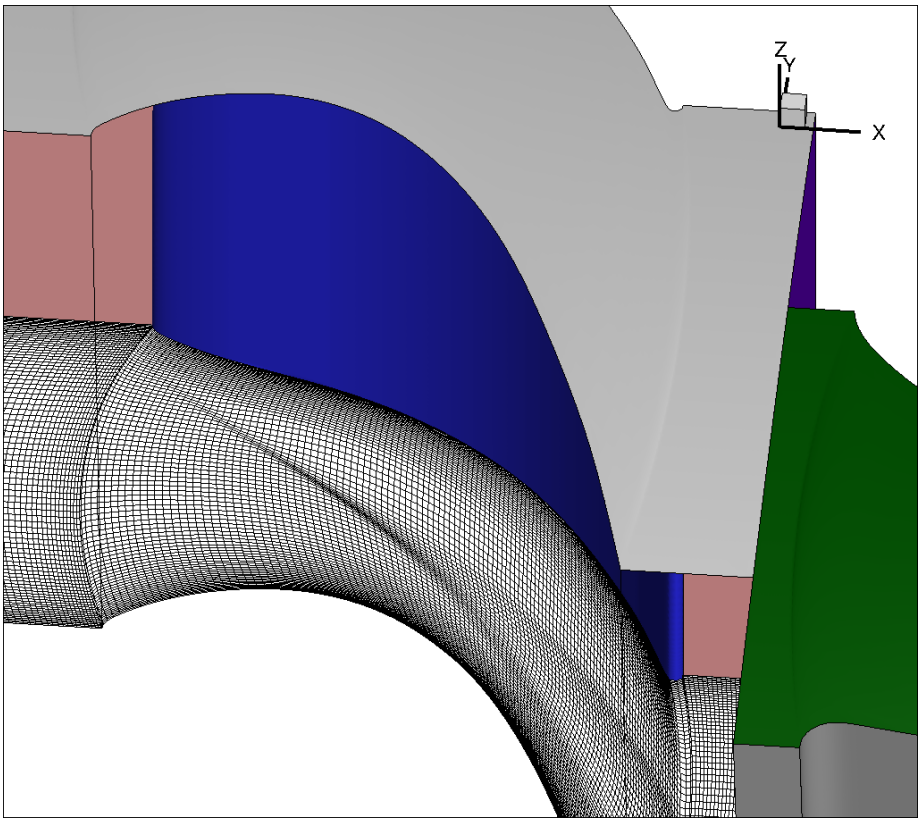

Figure 5-21: Non-axisymmetric upstream stator hub surface imported in ICEM CFD as a NURBS surface.

In the first task of the DoE optimisation, d_{le} is varied over the range 0.002 rad to 0.005 rad, d_{te} is varied over the range 0.037 rad to 0.05 rad, and h_o is kept constant as 68 % of the total groove length. Within this envelope of parameters, CFD predictions indicate the largest reduction in the stage total pressure loss coefficient is 2.67 % by using d_{le} = 0.005 rad and d_{te} = 0.05 rad. The second task of the DoE optimisation considered d_{te} ranging between 0.037 rad and 0.05 rad, h_o ranging between 60 % and 70 % of the total groove length, and a constant d_{le} = 0.005 rad. Within this second envelope of parameters, the highest reduction in the stage total pressure loss coefficient is predicted to be 2.36 %, by using d_{te} = 0.05 rad and h_o = 64 % of the total groove length.

The automatic optimisation process outcome is a contoured hub with groove of d_{le} = 0.005 rad, d_{te} = 0.05 rad, and h_o = 70 %. With this configuration, the stage total pressure loss coefficient is reduced by 2.72 % compared to the benchmark axisymmetric hub CFD prediction.

5.5 Cryogenic Cycle Analysis

The author's research sponsor requirement for developing techniques for improving cryogenic cycles is captured by a specific application to a LNG cycle. Improvements to any LNG cycle are achieved either by improving the heat exchangers used, by improving the efficiency of the compressors, or by improving the gas turbine stage isentropic efficiency. A change in the stage isentropic efficiency of the turbines used in a cryogenic cycle will reduce the amount of natural gas burnt for driving the cycle. This fuel consumption is necessary to generate mechanical power output from the gas turbines that is used to drive the refrigeration axial compressors. Reducing this fuel burn will reduce the cost of producing LNG.

The optimised stator 1 hub is used for the cryogenic cycle gas turbines to increase the $C.O.P._{LNG}$. A LNG plant was modelled using the Cycle-Tempo software to perform a cryogenic cycle analysis. The Conoco-Philips cycle was used, as representative of current industry practice. The schematic cycle generated by Cycle-tempo is shown in Figure 5-22. The modified gas turbines are labelled as items 23, 32, and 38 in the schematic of Figure 5-22. The three gas turbines worked with a stage isentropic efficiency of 84.82 % and a mechanical efficiency of 95 %. All the refrigeration cycle axial compressors worked with an optimistic 95 % mechanical efficiency. The Conoco-Philips LNG cycle consists of three main refrigeration cycles, the Propane refrigeration cycle, the Ethylene refrigeration cycle, and the Methane refrigeration cycle. Each refrigeration cycle axial compressor is driven by a gas turbine. The natural gas, NG, is cooled and liquefied from an inlet temperature of 37 °C to a liquefied temperature of -162 °C. Three main heat exchangers are used. The Propane refrigeration cycle job is to absorb heat from three fluids, the superheated Ethylene, the superheated Methane, and the NG by heat exchangers (12), (13), and (6) respectively. The Ethylene refrigeration cycle job is to remove heat by heat exchangers (25), from the superheated Methane, and (19), from the NG that outflows from heat exchanger (6). The methane refrigeration cycle is the final process of heat removal. Heat is removed from the NG and the outlet from the third heat exchanger (8) is a LNG with an outlet temperature of -162 °C. The standard natural gas components are listed in Table 5-6.

Table 5-6: Standard natural gas components.

Natural gas component	*Chemical symbols*	*Mole fraction (%)*
Nitrogen	N_2	*14.32*
Oxygen	O_2	*0.01*
Carbon dioxide	CO_2	*0.89*
Methane	CH_4	*81.29*
Ethane	C_2H_6	*2.87*
Propane	C_3H_8	*0.38*
i-Butane	C_4H_{10}	*0.15*
n-Butane	C_5H_{12}	*0.04*
i-Pentane	C_6H_{14}	*0.05*

To evaluate the $C.O.P._{LNG}$, three Cycle-tempo simulations are performed at the off-design operating conditions for the gas turbines. The first simulation is the part-load with a turbine stage isentropic efficiency of 94.62 %. The second simulation is the design point with an 84.82 % turbine stage isentropic efficiency. The third simulation is the turbine choking with an 82.54 % turbine stage isentropic efficiency. The $C.O.P._{LNG} = \frac{\sum Q_{heat\ exchanger}}{\dot{m}_{fuel} \times LCV_{fuel}} \times \eta_{Turbine\ stage\ isentropic}$, where LCV_{fuel} is the net calorific value of the fuel. Therefore, this expression shows that the $C.O.P._{LNG}$ can be improved by increasing the turbine stage isentropic efficiency. The gas turbine fuel is NG and it is labelled as pipeline numbers 28, 34, and 40 in Figure 5-22. Label 10 in Figure 5-22 designates the NG inlet to the LNG cryogenic cycle.

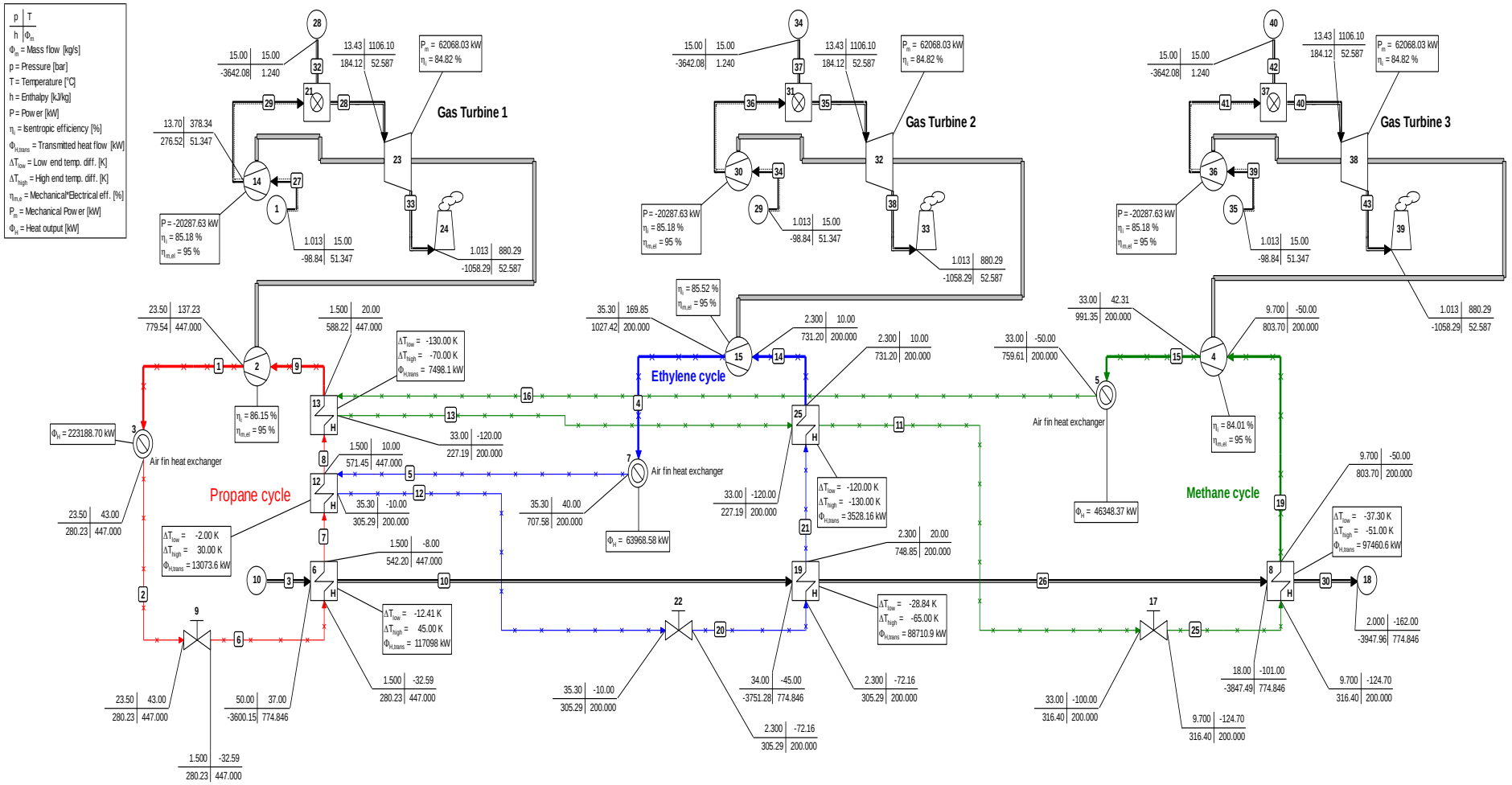

Figure 5-22: LNG cycle.

5.6 Summary

A numerical model was built to investigate the effectiveness of end-wall contouring for improving the aerodynamic performance of a 1.5 stage axial turbine. Four validation test cases were used. Mesh convergence testes were used to select an appropriate level of mesh refinement to use for the hub optimisation process. The Rotor validation test case was used as the benchmark for the optimisation process. A 1.5 stage axial turbine from RWTH Aachen was modelled for testing the effectiveness of contouring the upstream stator hub with the surface definition method of Section 4.4. The workflow of generating the geometry, meshing it, applying the boundary conditions, solving the flow, and analysing the results for pressure loss was successfully automated using APOW. The turbine stage total pressure loss coefficient and the stage isentropic efficiency were estimated as the target functions for the optimised contoured turbine stator 1 hub task. A complete LNG cryogenic cycle was modelled using Cycle-Tempo software. This software allows estimating the $C.O.P._{LNG}$ of the cryogenic cycle with the modified gas turbine that used the optimised contoured stator 1 hub. A positive correlation between the turbine stage isentropic efficiency and the $C.O.P._{LNG}$ was identified. This indicates that a cycle performance improvement can be achieved by using a modified gas turbine with an optimised contoured stator 1 hub in the cycle. In the next chapter, the numerical models from Chapter 5 are used to quantify these performance improvement indications.

6. RESULTS AND DISCUSSION

6.1 Introduction

In this chapter, the non-axisymmetric turbine stator 1 hub, imported in ANSYS ICEM CFD as an IGES file, replaces the axisymmetric turbine stator 1 hub of the validation test case. Flow simulations are then obtained using the same procedure detailed for the validation test case, using the same boundary conditions, flow solver, and post-processing. Flow predictions are obtained in terms of three parameters for the hub contoured by the guided groove technique: the groove width at the stator 1 blade leading edge, d_{le}, the position of the maximum groove depth, h_o, and the groove width at the stator 1 passage trailing edge, d_{te}. Numerical visualisations of the near-hub flow are obtained using ribbons to render the near-surface streamlines, as for the validation test case. The use of ribbons aim to explore whether the channelling groove captures the horseshoe vortex near the blade pressure side and continues to guide it until the maximum groove depth position h_o. Optimised values of the three hub groove parameters are sought from two optimisation tasks using a Kriging surrogate model. The best performing contoured stator hub is then used in a 1.5 stage simulation. The radially mass-averaged flow downstream of the rotor row is used to estimate the blade row total pressure loss, the stage total pressure loss coefficient, and the stage isentropic efficiency. Another set of flow predictions are obtained with the stator 1 hub contoured by the bump technique from Praisner et al. (2013) and from Kim et al. (2016), which is taken to represent the current industry best practice. Two optimisation tasks are performed to obtain the optimal values of the bump parameters using a Kriging surrogate model. The predicted flow and the stage performance are compared to the guide groove ones. Part-load design conditions are modelled with the hub geometry that gives the highest stage efficiency at the design point. A thermodynamic cycle analysis is finally used to estimate the effect of the stage isentropic efficiency changes on the performance of gas turbines in a representative LNG cycle, in which turbines are used for driving the axial compressors of Propane, Ethylene, and Methane refrigerants.

6.2 Flow Predictions with a Hub Contoured by a Guiding Groove

Flow predictions are obtained by the workflow shown in Figure 5-19. The execution of this workflow was automated by APOW. The workflow starts by defining the non-axisymmetric turbine stator 1 hub by MATLAB. It then imports the new stator 1 hub NURBS in ANSYS ICEM CFD 18. It joins it with the rest of the 1.5 stage turbine geometry, re-meshes it, and

exports the computational mesh into OpenFoam 3.2-extend. It applies the boundary conditions, it solves the flow by OpenFoam 3.2-extend to a converged solution, and post-processes the results. Automating the workflow enables a parametric study on the effect of the groove geometry on the flow predictions.

Two parameters were tested for defining the non-axisymmetric turbine stator 1 hub. These parameters were the groove pitchwise width and the maximum groove depth axial position. Two cases with different groove width configurations were tested. The first one used a constant groove width. The second one used a groove that started as pitchwise-narrow near the stator leading edge and expanded monotonically up to the end of the turbine stator 1 tailing edge. The position of the groove maximum depth in both cases was set to 40 % of the total groove path length. Figure 6-1 shows the flow predicted near the hub with a constant groove width equivalent to a pitchwise angle of 0.00146 rad, using the same flow visualization technique as for the validation test case in Figure 5-17. The viewpoint is set with the flow running from right to left, as indicated by the white arrow, to enable a better view of the vortex filament paths. The groove appears to be capturing the pressure side branch of the horseshoe vortex at the turbine stator 1 blade leading edge, as indicated by the clustering of the ribbons. These vortex filaments tend to follow the groove path until the groove maximum depth. Then individual vortex strands appear to leak out of the groove towards the trailing edge and move towards the blade suction side, driven by the pitchwise pressure gradient. With a d_{le} = 0.00146 rad pitchwise wide groove, the total pressure loss coefficient is predicted to decrease by 0.39 %. Figure 6-2 shows the corresponding result using a wider groove of d_{le} = 0.01 rad constant pitchwise width. Perhaps counter-intuitively, with the wider groove, there appears to be an earlier departure of vortex filaments from the groove, starting from about 25 % axial chord. These vortex strands are predicted to move towards the blade suction side, like in Figure 6-1, but they appear also to lift up more prominently from the hub surface, towards the centre of the main flow passage. The combination of this earlier departure from the groove and this greater interaction with the main passage flow is thought to be responsible for a lower reduction in the total pressure loss coefficient of 0.30 % compared to the hub with the d_{le} = 0.00146 rad narrower groove.

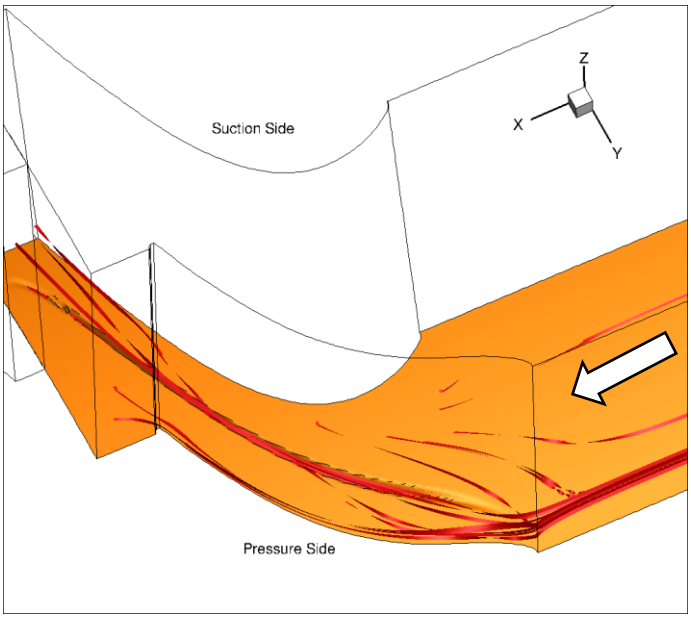

Figure 6-1: Flow visualisation over the non-axisymmetric stator 1 hub showing the pressure side branch of the horseshoe vortex running through a 0.00146 rad wide hub groove.

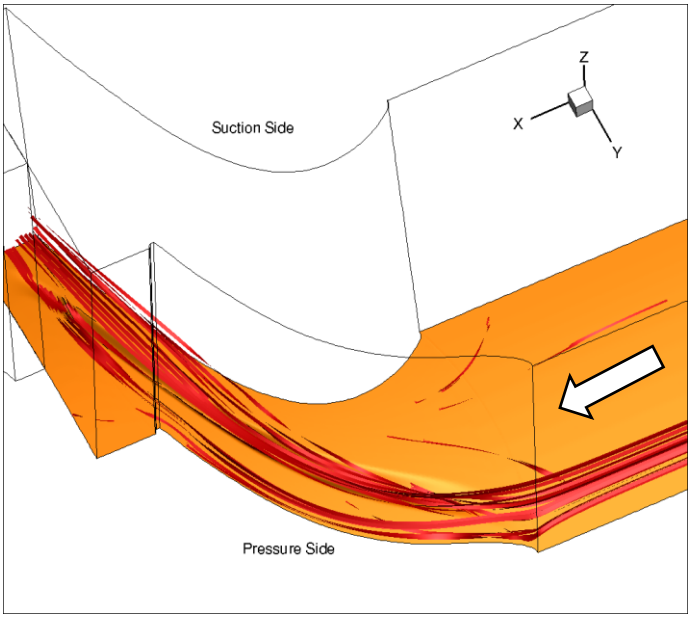

Figure 6-2: Flow visualisation over the non-axisymmetric stator 1 hub showing the pressure side branch of the horseshoe vortex running partially through a 0.01 rad wide hub groove.

The current flow predictions indicate that adding a pitchwise-narrow groove to the stator 1 hub surface is effective for capturing and channelling the pressure side branch of the horseshoe vortex away from the pitchwise consecutive blade suction side. This conclusion

led to adopting the d_{le} = 0.00146 rad pitchwise-narrow groove as the starting groove width at the leading edge for the variable groove test case, which is the second test case reported in the next paragraph.

The second test case uses a d_{le} = 0.00146 rad starting groove width at the turbine stator 1 blade leading edge and expands the groove monotonically towards the stator 1 passage trailing edge. The groove width at the turbine passage trailing edge is limited to d_{te} = 0.05 rad. This limitation prevents the corner vortex on the pressure side from slipping inside the groove and combining with the pressure side branch of the horseshoe vortex, as shown by the near-hub surface flow visualization in Figure 6-3. This test case predicts a reduction in the stage total pressure loss coefficient of 1.76 %. Figure 6-3 suggests that gradually extending the groove width towards the stator 1 passage trailing edge may accommodate the growth by entrainment of the pressure side branch of the horseshoe vortex, so that vortex filaments can be contained more inside the groove. This is thought to delay their interaction with the suction side branch of the horseshoe vortex, which runs along the blade suction side, which in turn delays the generation the passage vortex. The lower strength of the resulting secondary flows appears to be reflected by the reduction of the total pressure loss coefficient that reduces more than by using a groove of constant pitchwise width.

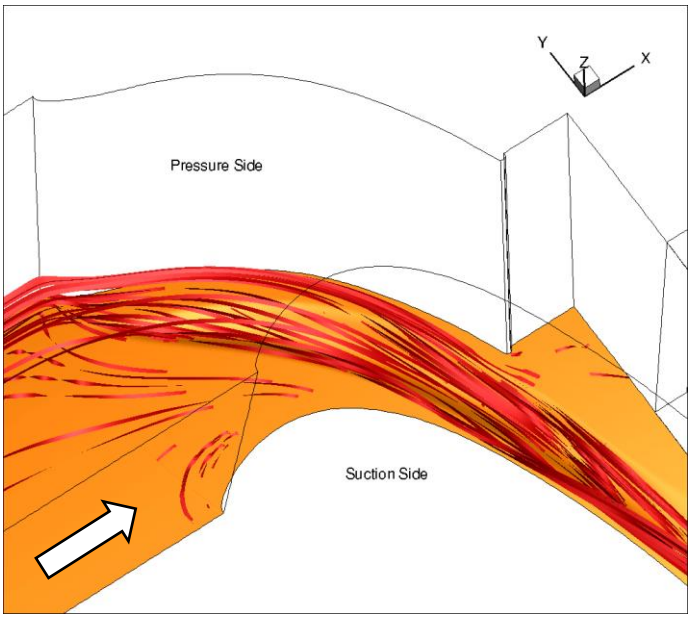

Figure 6-3: Flow visualisation of non-axisymmetric stator 1 hub showing the pressure side branch of the horseshoe vortex running through a hub groove widening from 0.00146 rad to 0.05 rad.

In the first and second test cases, the position of the groove maximum depth was kept constant at h_o = 40 % of the total groove path length. It is therefore of interest to investigate whether further reductions in the total pressure loss can be achieved by changing the location of the maximum groove depth. This change can be implemented in the current parametrisation of the hub surface by changes in the shape and scale factors of the Beta probability density function. The numerical results indicate that locating the groove maximum depth at about h_o = 60% of the total groove length further reduces the stage total pressure loss coefficient to 2.23% below the axisymmetric hub prediction.

6.3 Optimisation of the Guiding Groove

APOW has the ability to automate the optimisation process. The APOW software minimises a user-defined cost function evaluated on a Kriging surrogate model. In this application, the Kriging surrogate model is built from two main inputs and one output. The output variable is the stage total pressure loss coefficient. Two optimisation tasks are preformed. The input variables of task one are d_{le} and d_{te}. The second task input variables are d_{te} and h_o. 10 numerical experiments in each task are used to create the Kriging surrogate surface, each numerical experiment consisting of one evaluation of the stage total pressure loss coefficient by CFD. Figure 6-4 and Figure 6-5 show the two 3D Kriging surrogate surfaces for the two optimisation tasks. The response function obtained from the first task is essentially one-dimensional and the predicted loss appears to be broadly insensitive to changes in d_{le}. The second task shown in Figure 6-5 produced a more two-dimensional response surface, indicating that changes in d_{te} and in h_o are both significant in determining the loss. The Kriging surrogate surface of this second task predicts that the maximum reduction in the stage total pressure loss coefficient occurs at d_{te} = 0.05 rad and at h_o = 70 %.

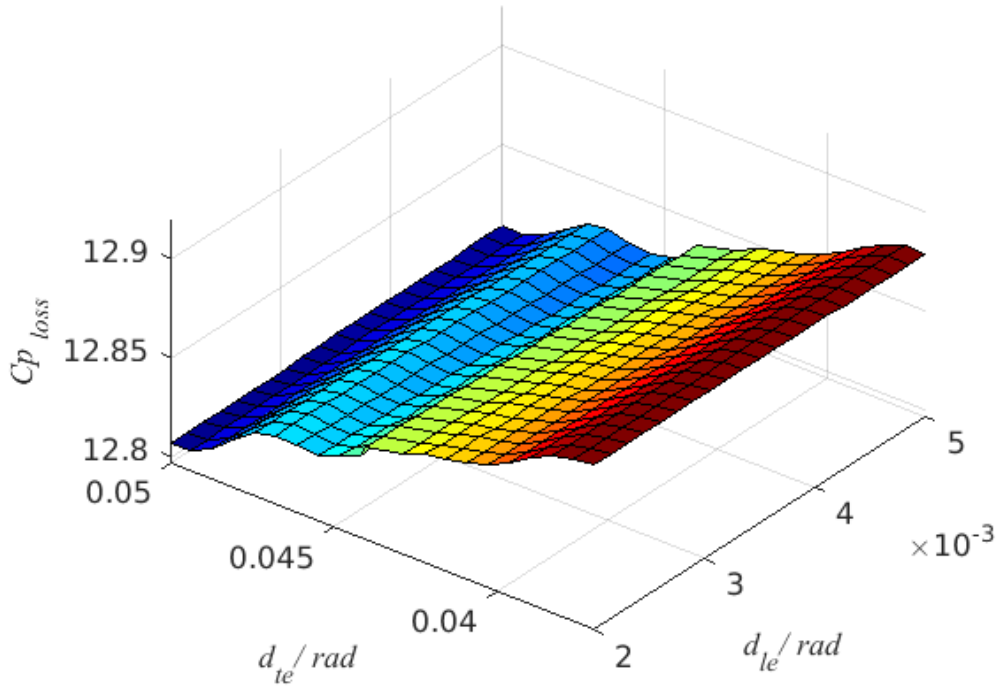

Figure 6-4: Kriging surrogate surface from optimisation task 1.

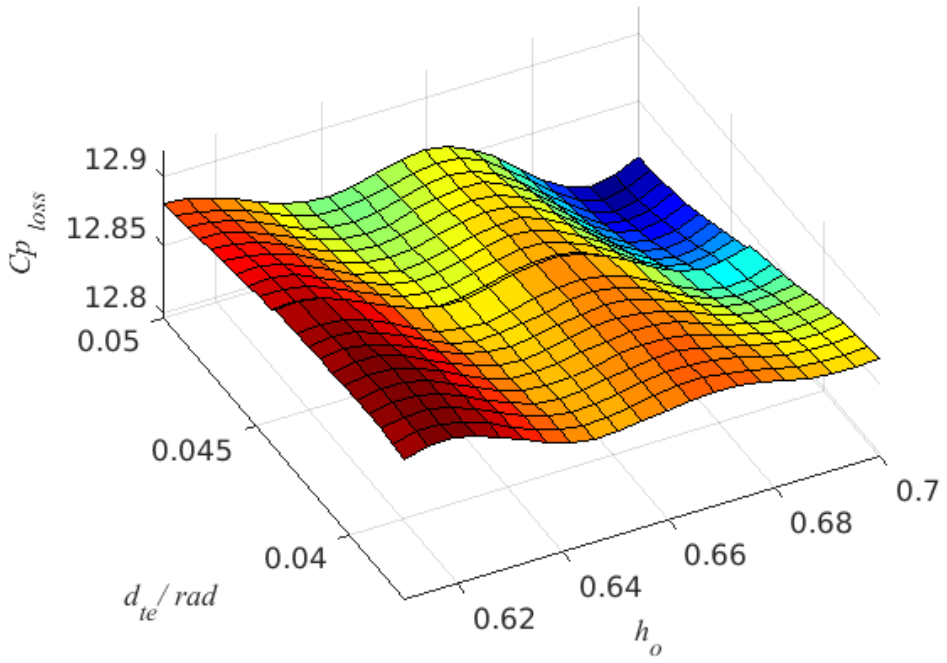

Figure 6-5: Kriging surrogate surface from optimisation task 2.

The accuracy of the Kriging surrogate model was tested by CFD modelling the flow though the passage with a groove of d_{te} = 0.05 rad, h_o = 70 %, and d_{le}= 0.005 rad. The difference in the pressure loss predicted by the Kriging model and that verified from this CFD simulation was evaluated as:

$$\psi = \frac{C_{p\ loss\ Kriging} - C_{p\ loss\ CFD\ exp}}{C_{p\ loss\ CFD\ exp}} \tag{6-1}$$

where $C_{p\ loss\ Kriging}$ is the stage total pressure loss coefficient from the Kriging surrogate model and $C_{p\ loss\ CFD\ exp}$ is the stage total pressure loss coefficient from the CFD prediction. $C_{p\ loss\ Kriging} = 12.805$ and $C_{p\ loss\ CFD\ exp} = 12.803$ give $\psi = 1.78 \times 10^{-4}$, which is less than 1% and it therefore confirms the good numerical accuracy of the magnitude of the stage pressure loss coefficient predicted by the surrogate model.

To check the sensitivity of the reconstruction of the Kriging surrogate model, 90 % of the test data were selected to regenerate the Kriging surrogate surface of task two. The relative difference between the original Kriging surrogate and new regenerated Kriging surrogate surface with 90 % of the test data is shown in Figure 6-6. This relative difference is computed as

$$\psi_2 = \frac{C_{p\ loss\ full\ Kriging} - C_{p\ loss\ 0.9\ Kriging}}{C_{p\ loss\ full\ Kriging}} \tag{6-2}$$

Figure 6-6 shows that this difference is below 1%, indicating that the Kriging model is relatively insensitive to a one-off data omission. This builds confidence in the relative independence of the Kriging model from the way in which the parameter space is sampled in the design of experiment (DoE).

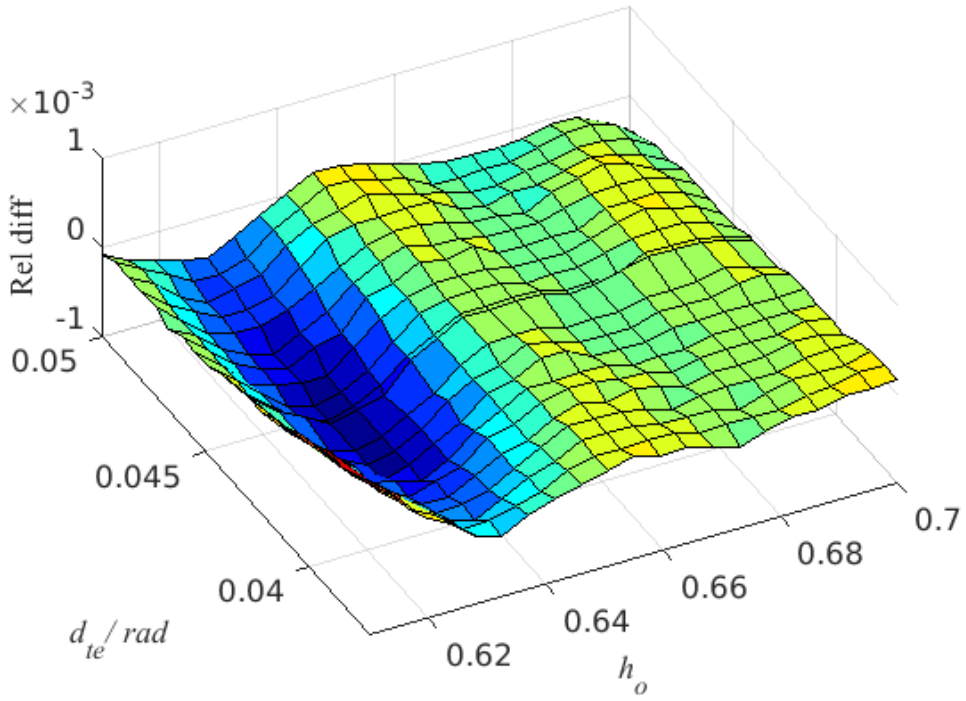

Figure 6-6: Relative difference between Kriging surrogate surface with 100% of the test data and regenerated Kriging surrogate using 90% of the test data.

The automatic optimisation process outcome is a predicted reduction in the stage total pressure loss coefficient of 2.72 % by using a groove of d_{te} = 0.05 rad, h_o = 70 %, and d_{le}= 0.005 rad, compared to an axisymmetric hub. It is of interest to investigate the flow field predicted using the hub with groove of optimised shape (d_{te} = 0.05 rad, h_o = 70 %, and d_{le}= 0.005 rad) and compare it against the benchmark axisymmetric flow. The aim is to identify the changes in the flow field that this geometrical feature generates and to find evidence of the physical process that is thought as being responsible for the loss reduction, namely the delay in the formation of the passage vortex.

Figure 6-7 shows the flow predicted near the stator 1 hub with groove using the same flow visualisation technique as for the axisymmetric hub test case in Figure 5-17. The pressure side branch of the horseshoe vortex at the turbine stator 1 blade leading edge is captured by the channelling groove, as indicated by the clustering of the ribbons at this location. These vortex filaments appear to follow the groove path up to the groove maximum depth location. Thereafter, they continue towards the trailing edge, following approximately the blade camber line, and exit through the mixing plane between the upstream stator and the rotor.

The post-processing using the OpenFoam sample dictionary shows an increase in the turbine stage isentropic efficiency of 1.60 %. The new design shows both a reduction in the average stage total pressure loss coefficient and an improvement in the stage isentropic efficiency compared to the axisymmetric hub configuration. The stage performance is computed based on the stage outflow located 8.8 mm downstream of the rotor exit row.

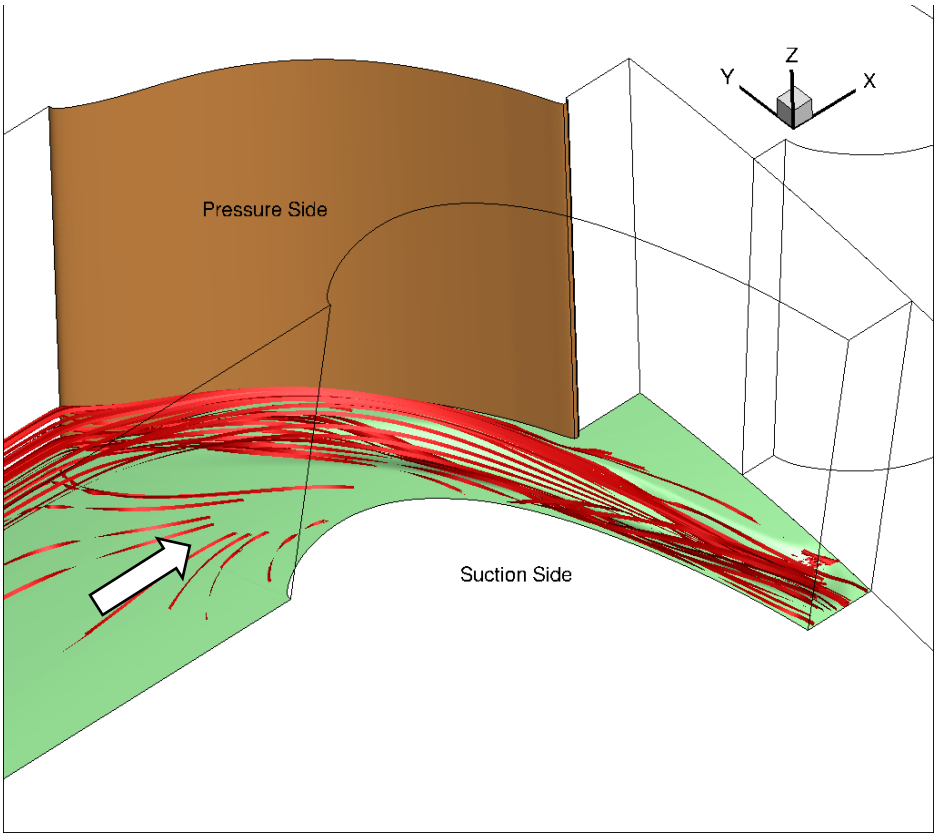

Figure 6-7: Visualisation of near-surface flow over the upstream stator hub showing the pressure side branch of the horseshoe vortex running through the APOW optimised hub groove.

Further insight into these bulk stage performance gains is sought by examining the stage discharge on the axial plane 8.8 mm behind the rotor. Figure 6-8 and Figure 6-9 show the predicted radial distribution of the mass-averaged total pressure p_{03} and of the mass-averaged stage isentropic efficiency with and without an axisymmetric hub, respectively. In this context, the mass-averaged stage isentropic efficiency is the stage isentropic efficiency computed using the flow state estimated at constant blade height.

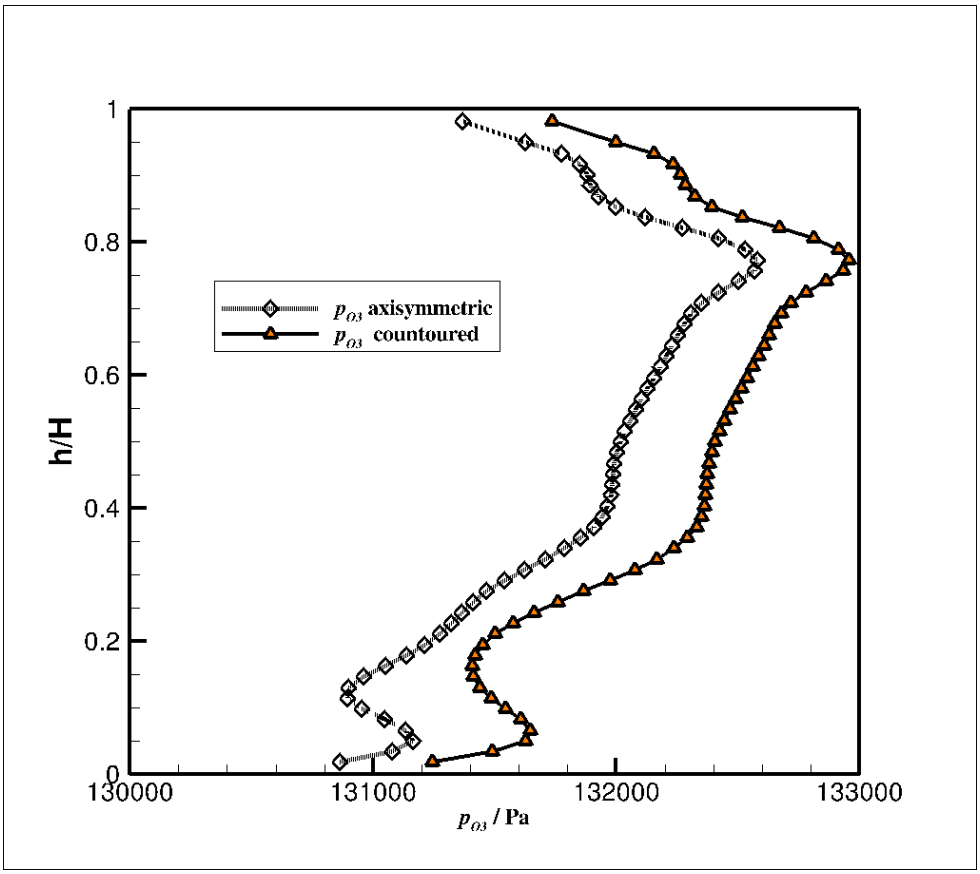

Figure 6-8: Radial distribution of mass-averaged total pressure at 8.8 mm behind the rotor blade row, with an axisymmetric and a contoured upstream stator hub.

As the stage isentropic efficiency is obtained from passage cross-section flow averages, the distribution in Figure 6-9 can be interpreted as the contribution to the stage isentropic efficiency from the flow at different radial heights. Contouring the upstream stator hub is beneficial to the flow as it increases the mass-averaged p_{03} over the full blade span, as shown in Figure 6-8. Near the hub, the local p_{03} minimum located approximately at $h/H = 0.1$ appears to be raised to $h/H = 0.2$, indicating a milder and more diffused near-hub secondary flow structure that transports more of the incoming flow total pressure. The mass-averaged stage isentropic efficiency also increases over the blade span fraction range $0 \leq h/H \leq 0.8$, as shown in Figure 6-9. A reduction is the mass-averaged stage isentropic efficiency is predicted over the narrower range $0.8 \leq h/H \leq 1.0$. This latter prediction has to be treated with some caution, due to the omission in the model of the rotor tip clearance.

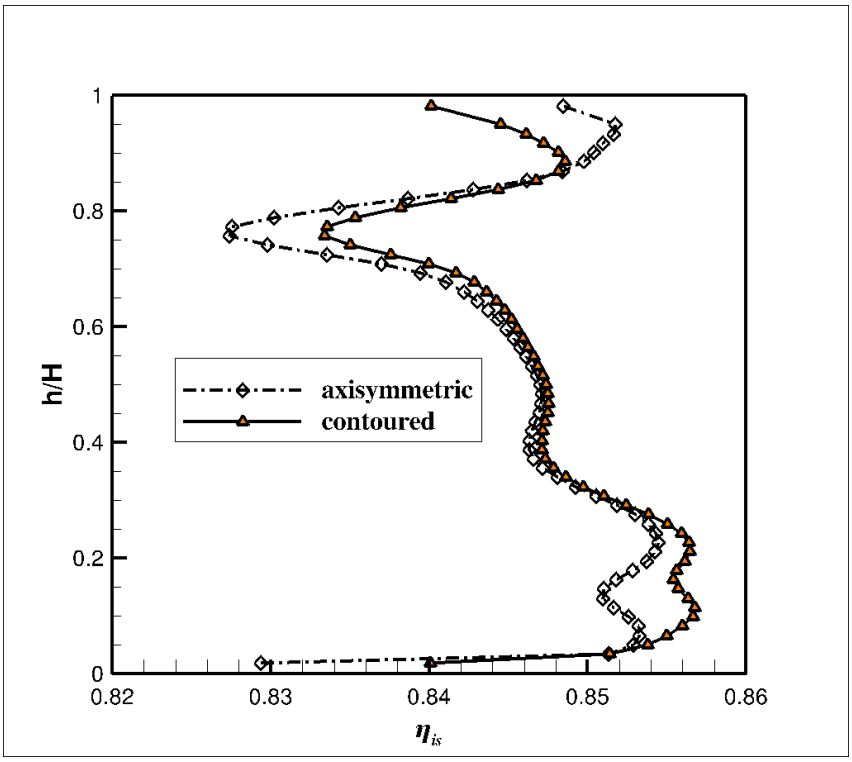

Figure 6-9: Radial distribution of mass-averaged stage isentropic efficiency at 8.8 mm behind the rotor blade row, with an axisymmetric and a contoured upstream stator hub.

Figure 6-10 and Figure 6-11 show the distribution of the predicted stage total pressure loss coefficient on the axial plane 8.8 mm behind the rotor with and without an axisymmetric hub, respectively. By contouring the hub, the flow passes the rotor with a suppressed secondary flow from the upstream stator and this changes the flow behaviour above the rotor blade root. Due to this change, the rotor exit flow seems to have a suppressed secondary flow near the hub region as shown in Figure 6-11. Specifically, the colour iso-levels of Cp loss display a reduction in the magnitude and size of the Cp loss compared to Figure 6-10, which is indicative of a reduction in the rotor suction side horseshoe vortex over the rotor hub. Near the rotor tip, the reduction of a local Cp loss maximum at $r \simeq 0.292$ m suggests a reduction in the blade tip vortex. Further inspection of these predictions shows that the hub modification is felt across the full blade span and has changed the rotor bulk flow. This is confirmed in Figure 6-12, which shows the predicted mass-averaged radial distribution of the stage total pressure loss coefficient at the same axial plane as Figure 6-10 and Figure 6-11. Contouring the upstream stator hub is shown to reduce the mass-averaged stage total pressure loss coefficient over the blade height fraction $0 \leq h/H \leq 0.18$, close to the hub, as well as over the range $0.23 \leq h/H \leq 1.0$. Loss is predicted to increase over the narrower range $0.18 \leq h/H \leq 0.23$, close to the main bulk

flow. The net effect is a decrease in the secondary flow losses, leading to the predicted increase the stage isentropic efficiency.

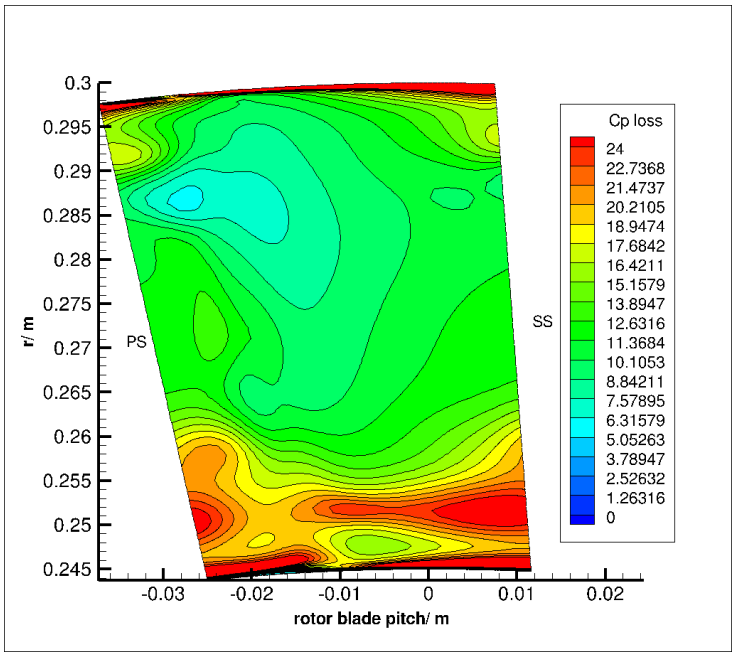

Figure 6-10: Iso-levels of total pressure loss coefficient predicted with an axisymmetric hub, 8.8 mm downstream of the rotor exit.

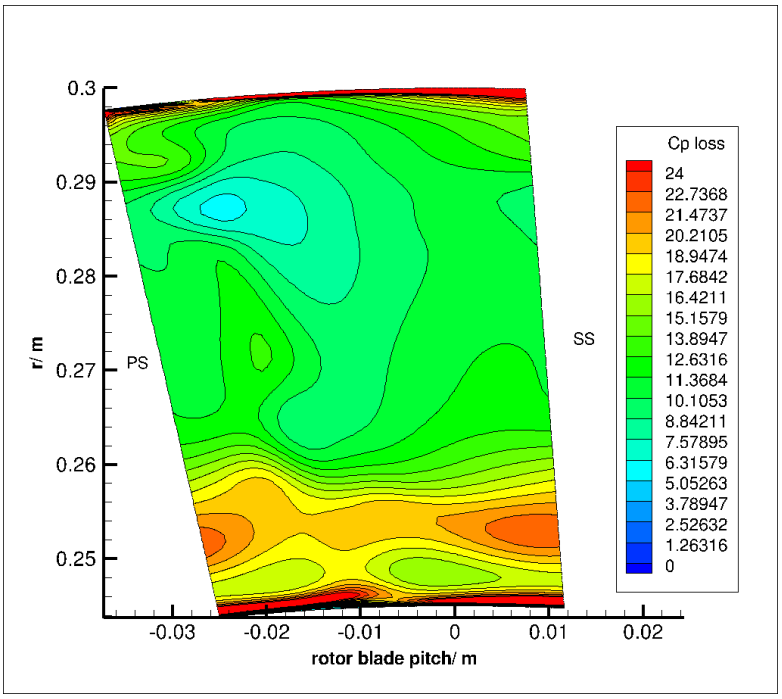

Figure 6-11: Iso-levels of total pressure loss coefficient predicted with a contoured hub, 8.8 mm downstream of the rotor exit.

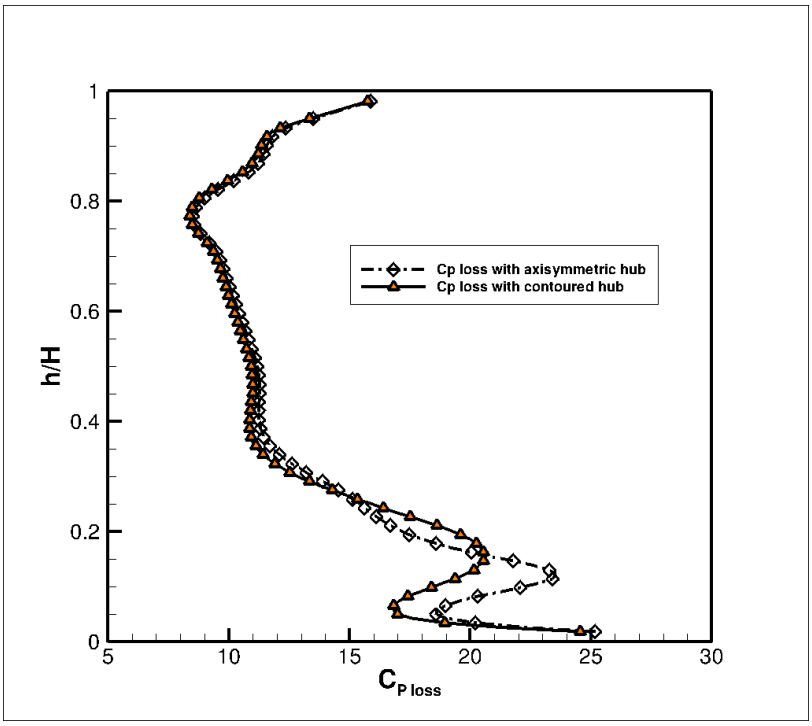

Figure 6-12: Radial distribution of mass averaged total pressure loss coefficient at 8.8 mm behind the rotor blade row, with an axisymmetric and a contoured upstream stator hub.

6.4 Flow Predictions with a Hub Contoured by Bumps

The axisymmetric stator 1 hub of Section 5.3.2 was replaced by a surface with bumps generated using the Praisner et al. (2013) and the Kim et al. (2016) parameterisation method described in Chapters Three and Four. The radial height of three points controlling the geometry of the bumps was optimised using APOW by performing two optimisation tasks. The first control point r_{SS} is located on the middle spline P_2 of Figure 3-2 near the blade suction side. The second and third control points r_{PS_1}, r_{PS_2} are defined on the spline P_4 of Figure 3-2 near the blade pressure side. The input variables of optimisation task one are r_{SS} and r_{PS_2}. The second optimisation task input variables are r_{PS_1} and r_{PS_2}. A Kriging surrogate model was generated from each task using the same procedure of Section 6.3, driven by the same aerodynamic loss definition. Figure 6-13 and Figure 6-14 show the two 3D Kriging surrogate surfaces from the two optimisation tasks. The response function obtained from the first task is essentially one-dimensional, the predicted loss appears to be mainly dependent on r_{SS} and the lowest loss is predicted at r_{SS} = -3 mm. In the second task, r_{SS} was kept constant at r_{SS} = -3 mm. The response function from the second task shown in Figure 6-14 is more two-dimensional, indicating that changes in r_{PS_1} and in r_{PS_2} are both significant in determining the loss. The Kriging surrogate surface of this second task predicts that the

maximum reduction in the stage total pressure loss coefficient occurs at r_{PS_1} = -3 mm and r_{PS_2} = 1 mm. The accuracy of the Kriging surrogate model was tested by CFD modelling using the optimal bump parameters (r_{SS} = -3 mm, r_{PS_1} = -3 mm and r_{PS_2} = 1 mm). The relative difference $\psi = 3.29 \times 10^{-4}$, which shows that the accuracy of the Kriging model in predicting the loss from the hub contoured by bumps is well within the acceptable loss prediction uncertainty typically used in industry.

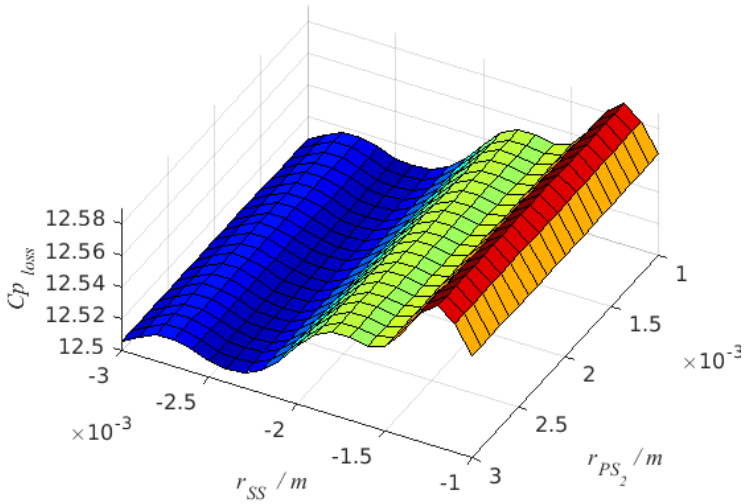

Figure 6-13: Kriging surrogate surface from bump optimisation task 1.

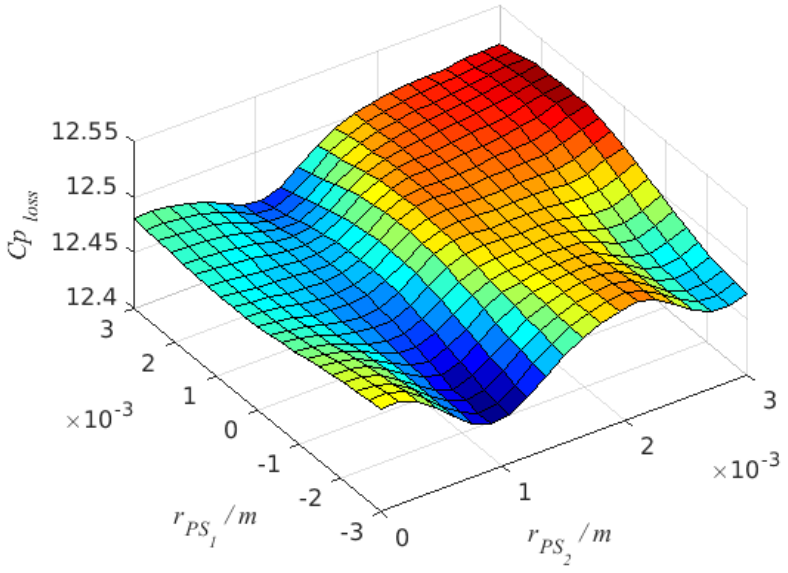

Figure 6-14: Kriging surrogate surface from bump optimisation task 2.

The automatic optimisation outcome using Praisner et al. (2013) and Kim et al. (2016) parameterisation method was a reduction in the stage total pressure loss coefficient by 5.48 %, compared to the benchmark turbine with an axisymmetric hub. The stage isentropic efficiency was evaluated by post-processing the flow predictions using OpenFOAM. The stage isentropic efficiency is predicted to increase by 0.19 % by using the hub with humps compared to the axisymmetric hub simulation. This increase is lower than the 1.60 % increase from the optimisation of the guide groove in Section 6.3. The main aim of the thesis is to decrease the stage total pressure loss coefficient with an increase in the stage isentropic efficiency. An improvement in the stage isentropic efficiency is preferable for an application to a cryogenic cycle, since this improves the cycle coefficient of performance, as discussed in Section 5.5.

It is of interest to go beyond the estimation of bulk aerodynamic performance parameters for the test turbine and explore more in details the changes in the flow field that are responsible for the predicted variations in stage isentropic efficiency and in stage total pressure loss. To this end, a comparison is performed of salient flow parameters from the optimised bump hub surface (r_{SS} = -3 mm, r_{PS_1} = -3 mm and r_{PS_2} = 1 mm) with both the benchmark axisymmetric and optimised grooved hub (d_{te} = 0.05 rad, h_o = 70 %, and d_{le}= 0.005 rad). Figure 6-15 shows the predicted mass-averaged coefficient of secondary kinetic energy C_{SKE} at 8.8 mm downstream of the stator 1 exit plane. Both the optimised bump surface and the optimised guide groove hub give a reduction in the C_{SKE}. The optimised guide groove is predicted to reduce the C_{SKE} near the hub, over the range $0.018 \leq h/H \leq 0.3$, more than the benchmark axisymmetric and optimised bump hub. These improvements can be attributed to the groove delaying the combination of the pressure side arm of the horseshoe vortex with the suction side arm of the horseshoe vortex from the neighbouring blade. This is likely to produce a better outflow entering the rotor, from the suppressed passage vortex. This positive effect is particularly noticeable in Figure 6-15 over the blade span range $0.018 \leq h/H \leq 0.13$, where the secondary kinetic energy peak, which is possibly associated to the hub passage vortex, appears to have been eliminated in the contoured hub with a guide groove predictions. The optimised bump surface gives a reduction in the C_{SKE} which is relatively small compared with that from the optimised groove hub over the blade span range $0.018 \leq h/H \leq 0.13$ and performs better over the blade span range $0.3 \leq h/H \leq 0.84$, as shown in Figure 6-15.

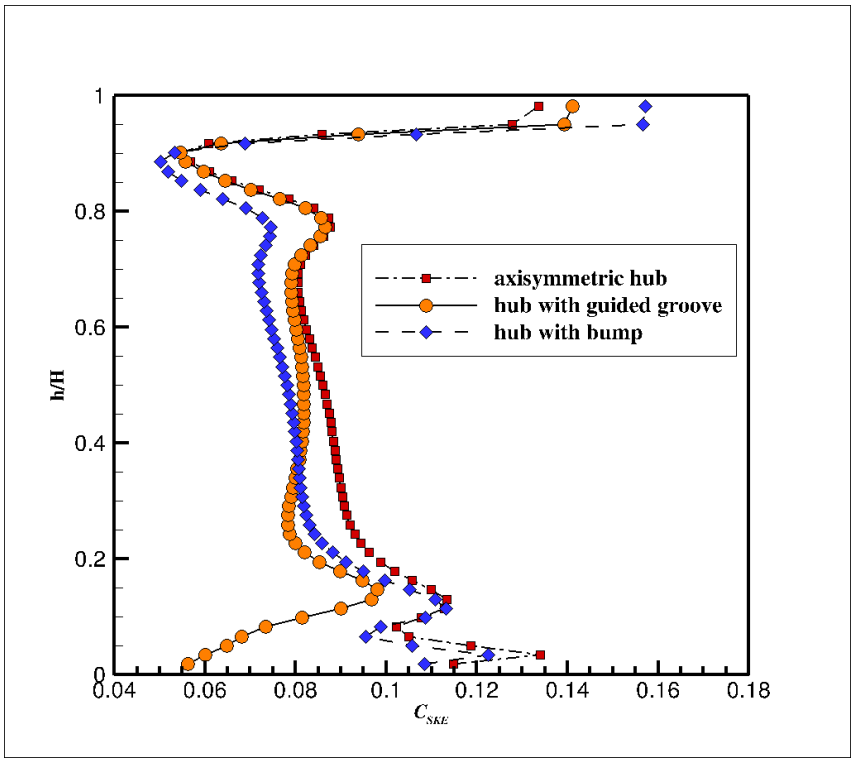

Figure 6-15: Radial distributions of mass averaged C_{SKE} at 8.8 mm behind the rotor blade row, with an axisymmetric and a contoured upstream stator hub.

Figure 6-16 shows the distribution of the predicted stage total pressure loss coefficient on the axial plane 8.8 mm behind the rotor with the hub contoured by bumps. The effect of the passage vortex is reduced as compared to the axisymmetric hub predictions shown in Figure 6-10. The corner vortices at the passage pressure side are also reduced in magnitude and size downstream of the rotor exit. The magnitude and size of the rotor vortices using the optimised bump parameterisation at the stator 1 hub seem to be higher than the rotor vortices shown in Figure 6-11 with the stator 1 hub contoured by the optimised guide groove. This is confirmed in Figure 6-17 by a lower stage total pressure loss coefficient over the blade range $0.018 \leq h/H \leq 0.14$ from the hub with groove than from the hub with bumps. This is probably due to the reduced interaction of the separated horseshoe vortex from the blade pressure side with the suction side horseshoe vortex, by using the guide groove. This leads to a reduction in the streamwise vorticity at the mixing plane between the stator 1 and the rotor. This reduction is shown in terms of the axial vorticity component Ω_x downstream of the rotor exit near the hub region, in Figure 6-18.

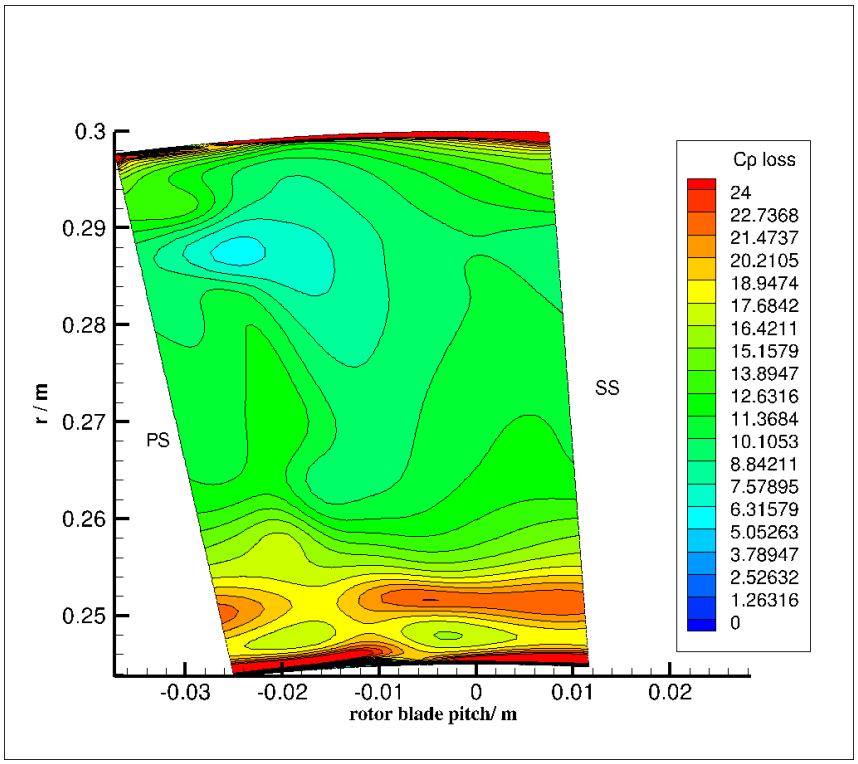

Figure 6-16: Colour iso-levels of total pressure loss coefficient predicted with a hub contoured by bumps, 8.8 mm downstream of the rotor exit.

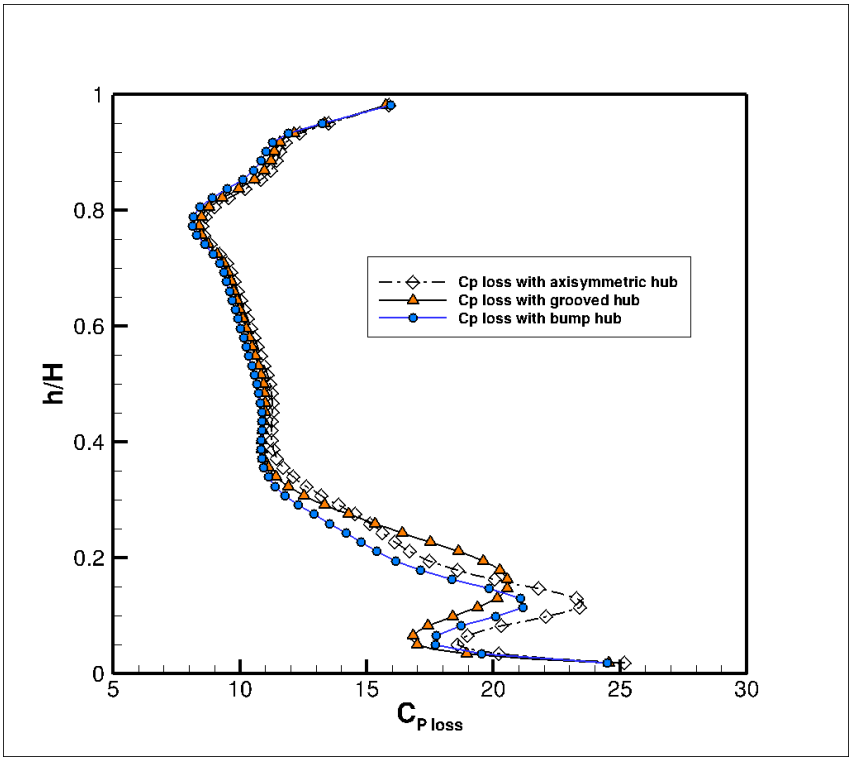

Figure 6-17: Radial distributions of mass-averaged total pressure loss coefficient at 8.8 mm behind the rotor blade row, with an axisymmetric and a contoured upstream stator hub.

Figure 6-18, Figure 6-19, and Figure 6-20 show respectively the iso-levels of the predicted axial vorticity component Ω_x with an axisymmetric hub, a hub contoured by the optimised guide groove, and a hub contoured by bumps, 8.8 mm downstream of the rotor exit plane. Figure 6-19 and Figure 6-20 show a reduction in the vorticity associated with the corner vortices at the pressure side and suction side blade root, compared to the axisymmetric hub predictions of Figure 6-18. The passage vortex seems to reduce more by contouring the hub with an optimised guide groove than with bumps. The guide groove is thought to sink the pressure side arm of the horseshoe vortex below its normal radial height, with respect to the axisymmetric hub configuration. The hub contouring also creates a longer path between the vortex initiation in the neighbourhood of the blade leading edge and the location at which it interacts with the suction side arm. This probably reduces the intensity of the cross-flow over the hub from the pressure side to the suction side, resulting in a weaker passage vortex. As the passage vortex of reduced strength passes through the mixing plane, from the stationary to the rotating frame of reference, less of the non-uniform pitchwise velocity distribution is turned in specific turbulent kinetic energy. This process models the passage vortex of reduced strength being chopped up by the rotor to produce unsteady wakes of reduced strength, in the time-resolved flow. This process may well have a role in reducing the strength of the in-plane motion near the hub downstream of the rotor exit. This reduction is shown in Figure 6-19 and Figure 6-20 over the blade radius range $0.248 \leq r \leq 0.255$.

Figure 6-21 and Figure 6-22 show the axial distribution of the specific turbulent kinetic energy predicted on the same axial plane as Figure 6-18 to Figure 6-20. The turbulent kinetic energy k near the rotor hub with the optimised groove is less than over the hub with the optimised bumps, confirming a probable weaker production of specific turbulent kinetic energy as the passage vortex goes through the mixing plane. This clearly shown in Figure 6-21 and Figure 6-22 over the blade radius range $0.248 \leq r \leq 0.255$.

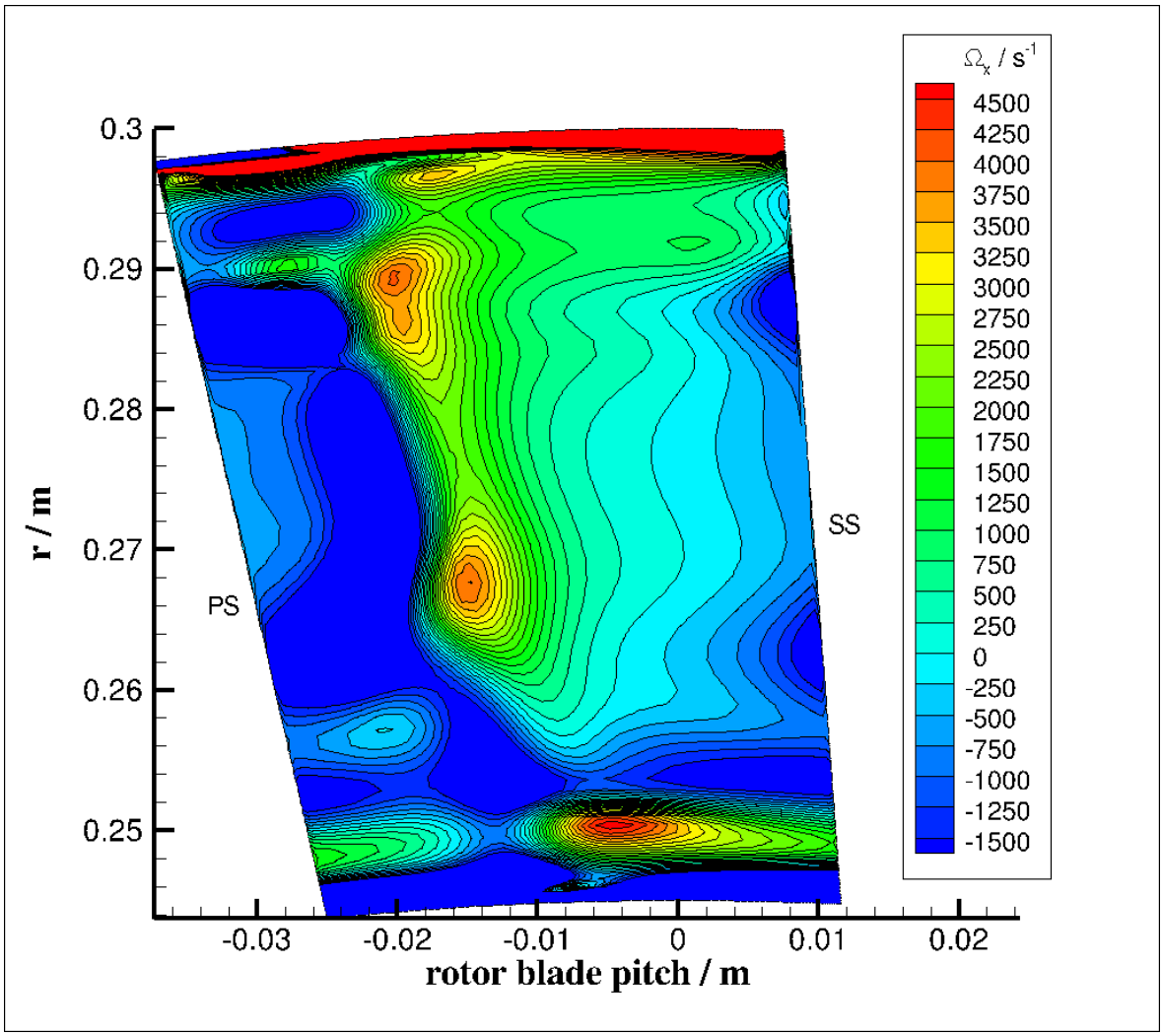

Figure 6-18: Colour iso-levels of x-vorticity component predicted with an axisymmetric hub, 8.8 mm downstream of the rotor exit.

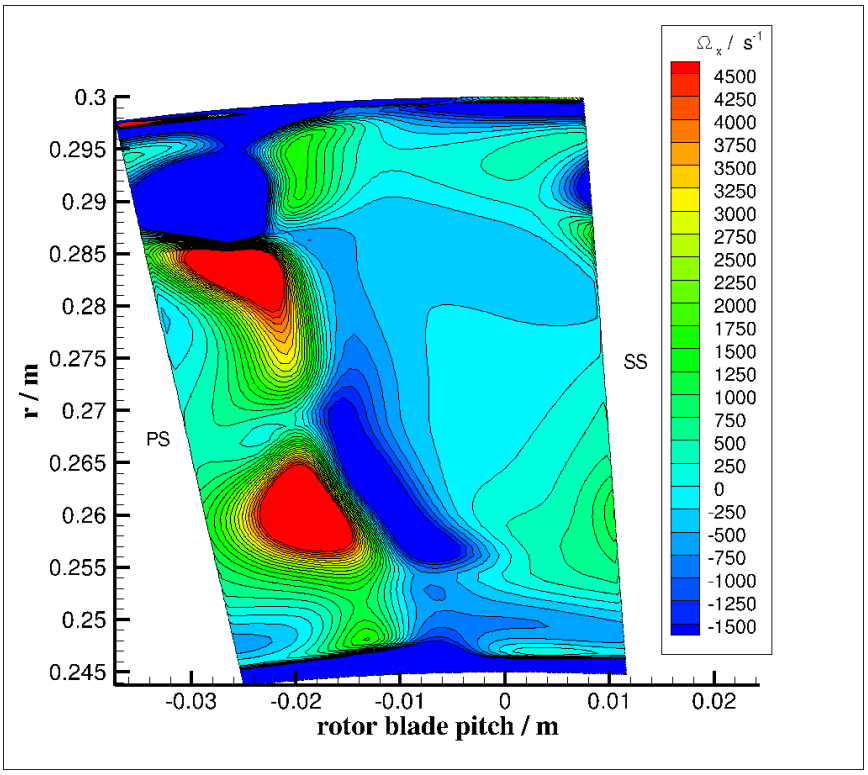

Figure 6-19: Colour iso-levels of x-vorticity component predicted with a hub contoured by a guide groove, 8.8 mm downstream of the rotor exit.

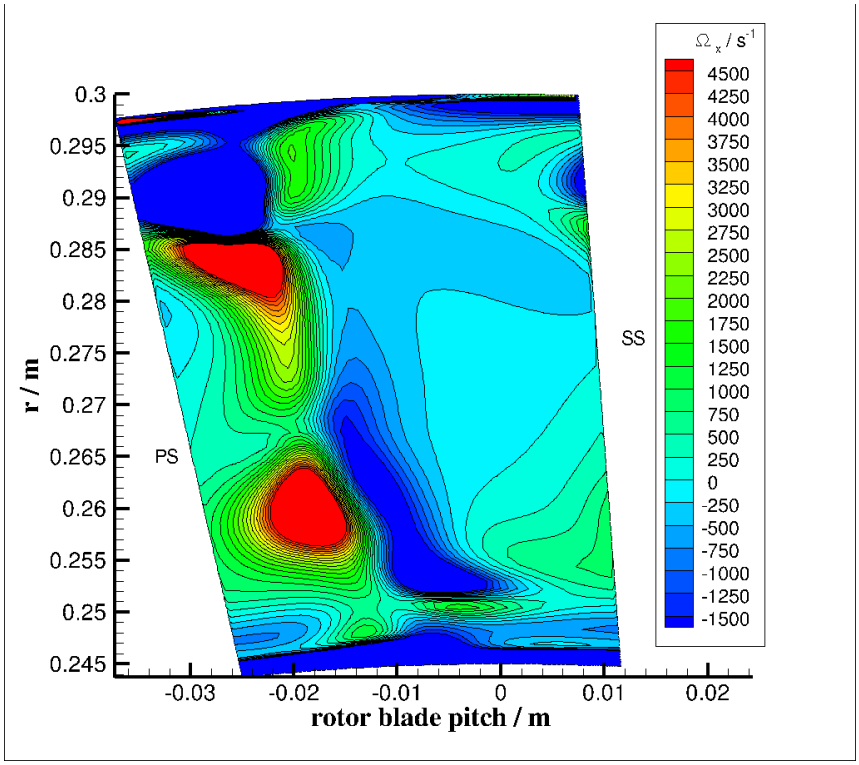

Figure 6-20: Colour iso-levels of x-vorticity component predicted with a hub contoured by bumps, 8.8 mm downstream of the rotor exit.

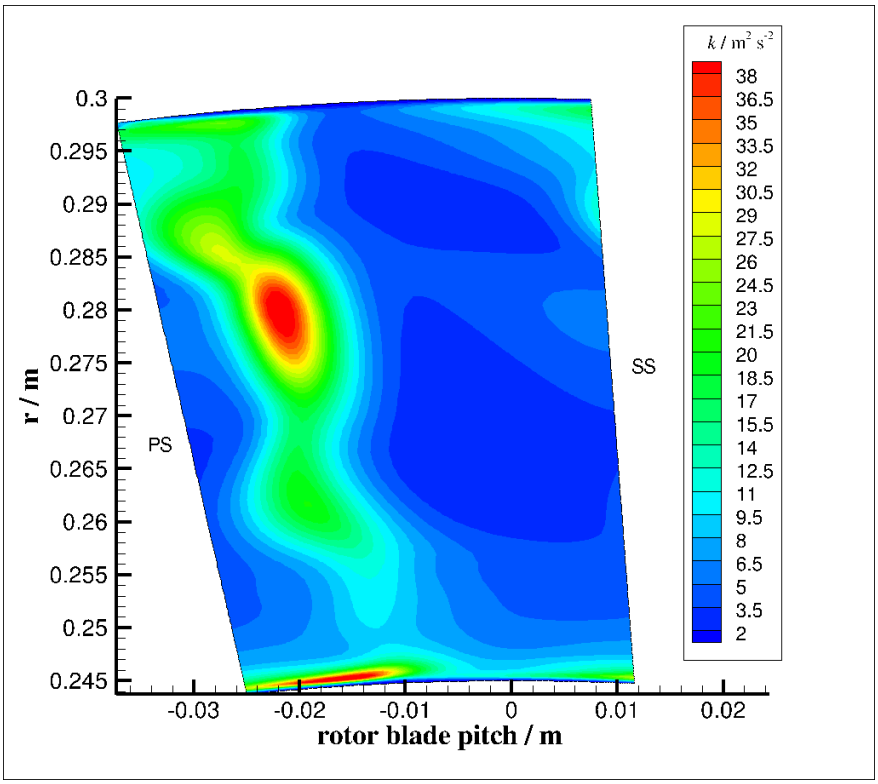

Figure 6-21: Colour iso-levels of specific turbulent kinetic energy predicted with a hub contoured by a guide groove, 8.8 mm downstream of the rotor exit.

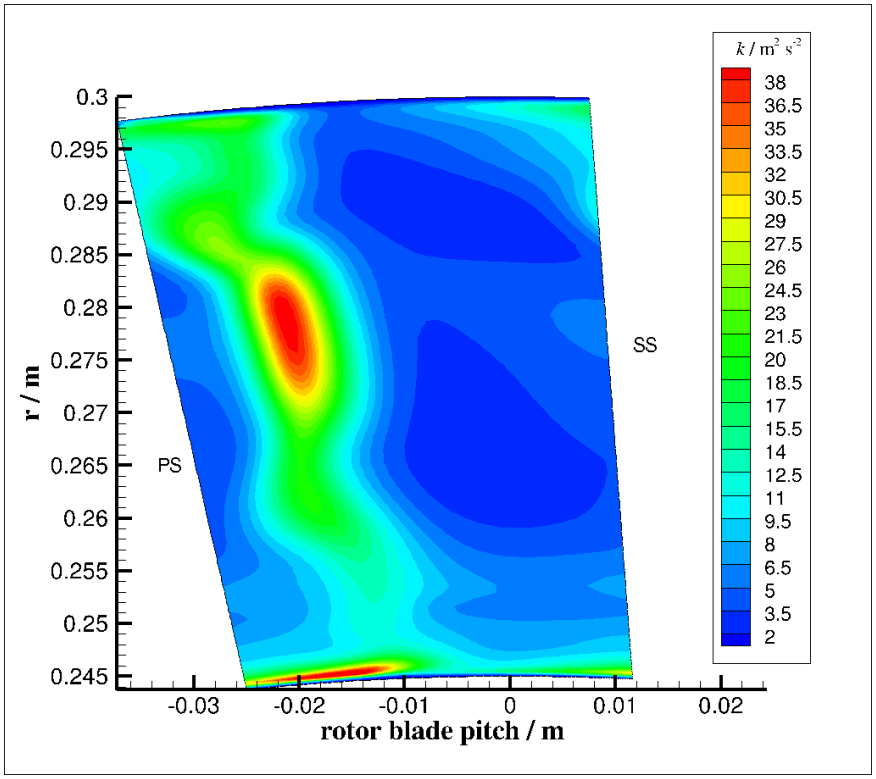

Figure 6-22: Colour iso-levels of specific turbulent kinetic energy predicted with a hub contoured by bumps, 8.8 mm downstream of the rotor exit.

6.5 Performance at Part Load

The 1.5 axial stage turbine model with the optimised groove of d_{te} = 0.05 rad, h_o = 70 %, and d_{le} = 0.005 rad was tested at off-design conditions by varying the computational domain inlet total pressure p_{01} over the range 153555.5 Pa to 160631.6 Pa. The inlet total temperature, the outlet static pressure, and the axial inflow angle were kept constant.

Figure 6-23 shows the predicted characteristic line of the 1.5 stage turbine with the contoured hub. The design point is the condition at which the groove is optimised in section 6.3. The end points of the characteristic line are the 50 % part-load and the choking of the stator passage, as labelled in Figure 6-23. The 50 % part load is defined by the passage mass flow rate being half of that at choking. The choking condition is identified by computing the mass flow rate through the upstream stator and noting that, at an inlet total pressure of 157099 Pa, $(\dot{m}\, T_{01}^{\frac{1}{2}} p_{01}^{-1})$ attains the constant value of 1.2446. The part-load operating inlet total pressure is 154055.5 Pa. The extrema of the operating line were defined considering that the losses associated with operating an axial turbine for power generation above choking and below 50 % part-load typically make these regimes economically and environmentally unattractive for a typical industrial use. Eleven discrete inflow conditions were tested, at progressively increasing values of the inlet total pressure, which are shown by the dots in Figure 6-23. This figure shows that increasing the inlet total pressure monotonically increases the normalised passage mass flow rate up to the choking point, in agreement with classical compressible flow theory (Cengel and Boles, 2002).

Figure 6-24 compares the predicted stage total pressure loss coefficient from the axisymmetric and contoured hub configurations along the operating line. Over the full operating line, the stage pressure loss coefficient with a contoured hub is always lower than that from the baseline axisymmetric hub geometry. This $C_{p\,loss}$ reduction seems to improve from part-load operations towards the choking condition. This is likely due to the increase in the passage mass flow rate on approach to choking, which increases the secondary flow losses and the shock losses compared to the design point.

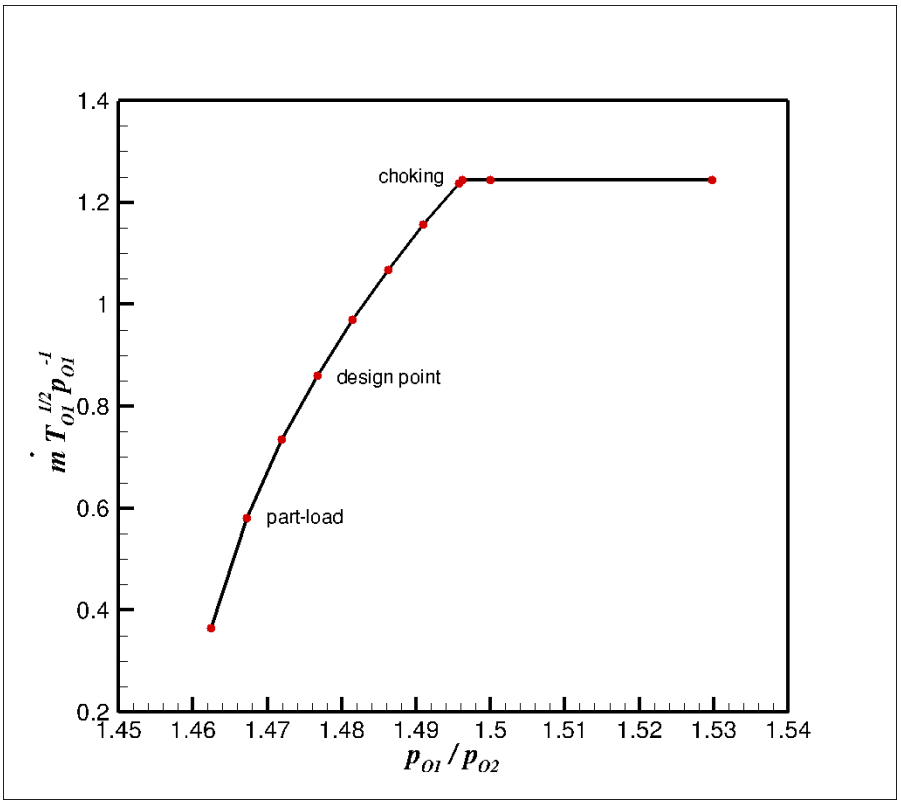

Figure 6-23: 1.5 stage turbine characteristic line with flow simulations shown by dots.

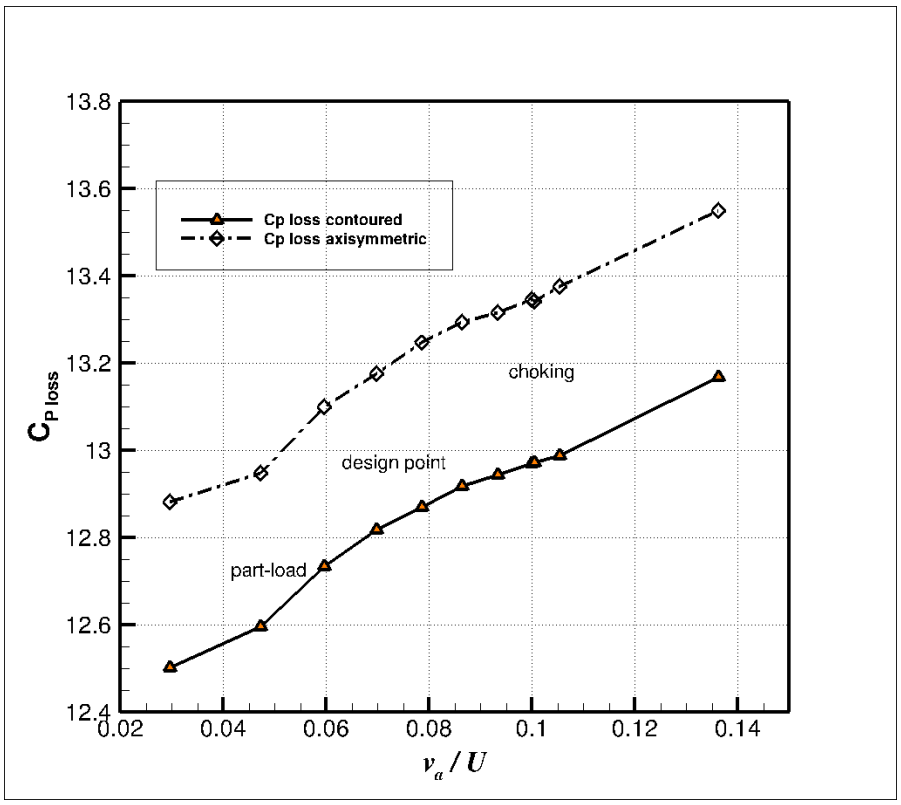

Figure 6-24: Predicted stage total pressure loss coefficient with an axisymmetric and a contoured upstream stator hub at design and off-design.

The performance improvement at off-design conditions obtained by implementing the hub groove is confirmed in Figure 6-25, where the predicted stage isentropic efficiency is shown over the same operating range of the 1.5 turbine stage shown in Figure 6-24. Adding the optimised groove to the upstream stator hub is predicted to increase the stage isentropic efficiency by 1.03 % at part-load operating conditions, by 1.60 % at the design point, and by 1.16 % in the choked turbine. Hence, performance gains are confirmed to occur over the full operating line.

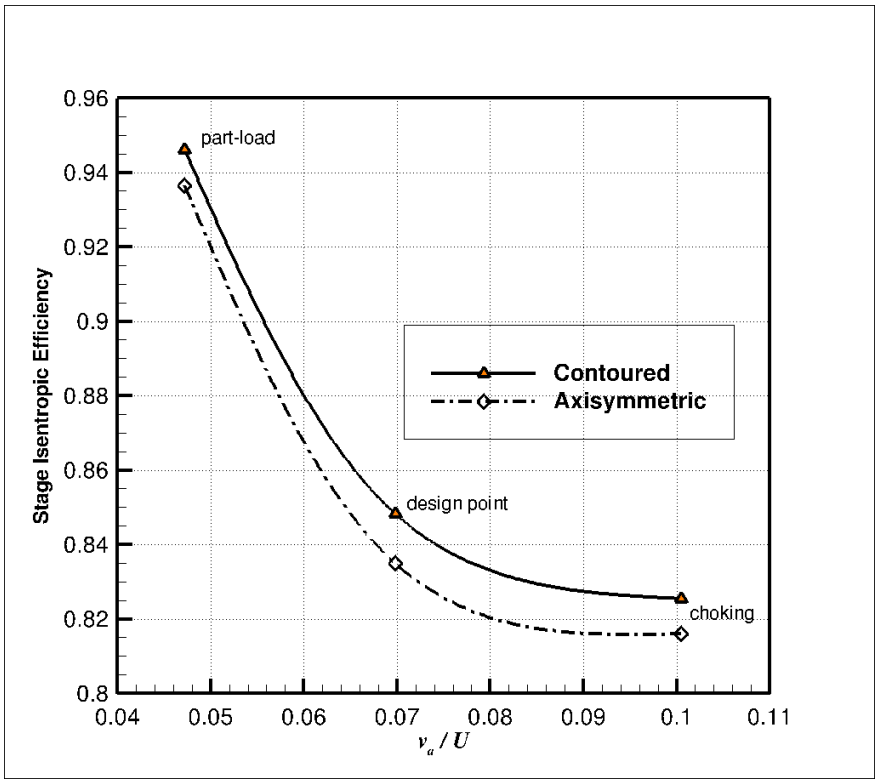

Figure 6-25: Predicted stage isentropic efficiency with an axisymmetric and a contoured turbine stator hub at design and off-design.

6.6 Cryogenic Cycle Performance Enhancement

The performance of a cryogenic cycle is determined by the Coefficient Of Performance (C.O.P.) of the complete cryogenic cycle, which includes any gas turbine. Changes in the stage isentropic efficiency of the gas turbine leads to changes in the C.O.P. of the cryogenic cycle. For the purpose of evaluating this change, the author has selected a cryogenic cycle from Conoco Phillips LNG, as discussed in Section 5.5. The cryogenic cycle by Conoco Phillips uses the three refrigerants propane, ethylene, and methane.

Figure 6-26 shows the LNG cooling curve, starting from NG at 37 °C inlet temperature. The first heat exchanger using a Propane cycle removes 33 % of heat from the NG and outputs it at -45 °C. The second heat exchanger using an Ethylene cycle absorbed about 50 % of the heat from the NG and outputs it -101 °C. 22% of the NG heat is removed by the third heat exchanger, by the Methane refrigeration cycle. The outlet temperature of the LNG at the exit of the third heat exchanger is -162 °C, which is the combined-cycle LNG output temperature.

Each refrigerant cycle is driven by separate gas turbine. The increase in the axial turbine stage isentropic efficiency leads to a reduction in the mass flow rate that is required to produce the mechanical power output from the turbine. The C.O.P. is defined as the ratio of the total heat absorbed by the three refrigerants to the total mechanical turbine power that is required to drive the axial compressors of the three refrigerant cycles.

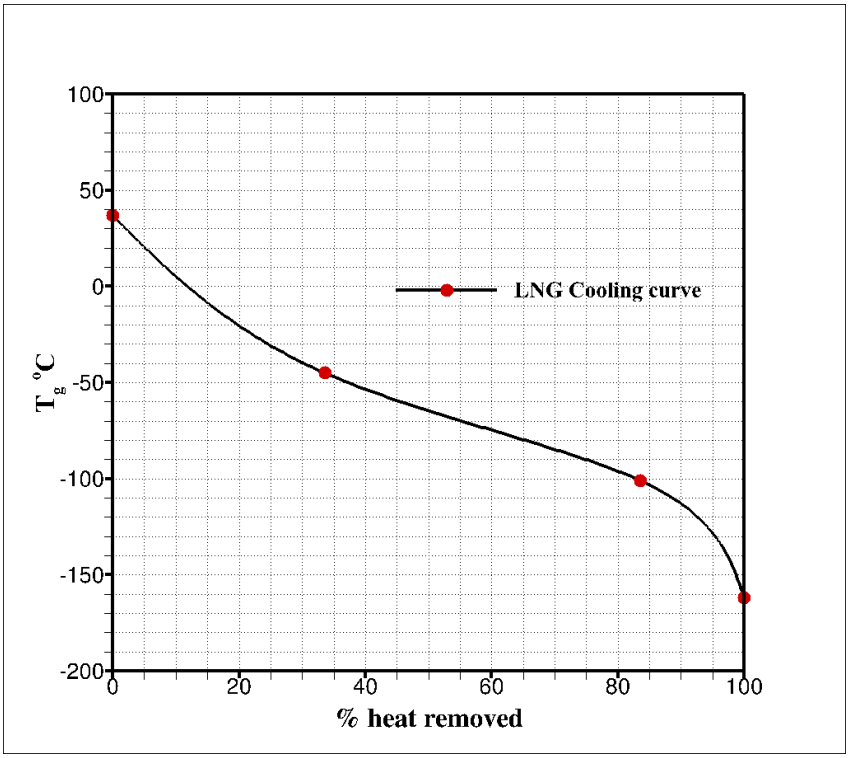

Figure 6-26: LNG cooling curve.

Figure 6-27 shows by a bar chart the C.O.P. predicted with an axisymmetric and a contoured turbine stator 1 hub at design and off-design conditions, with a constant natural gas flow rate feed to the gas turbines. The hub is contoured by the optimised guide groove of Section 6.3. The C.O.P. is predicted to increase with increasing turbine stage isentropic efficiency. This C.O.P. increase results from the increase in the mechanical power output from the gas turbines that drive the LNG cycle, due to the reduction in the secondary flow losses through

the turbine stage. The C.O.P. increased by 1.03 % at part-load, 1.60 % at design point, and 1.20 % at the choking condition of Section 6.3, as shown in Figure 6-27. The same trend is observed in Figure 6-28, which reports C.O.P predictions with a variable natural gas fuel mass flow rate, under the condition of a constant heat extraction from the LNG. The fuel mass flow rate is changed so to keep the same turbine mechanical power output value, as the turbine stage isentropic efficiency is changed by end-wall contouring. This reduces the turbine specific fuel consumption. The predicted C.O.P. gain reduces the cost of the natural gas burnt to drive the LNG cycle. In this case, The C.O.P. increased by 2.12 % at part-load, 3.15 % at design point, and 2.20 % at choking condition, as shown in Figure 6-28.

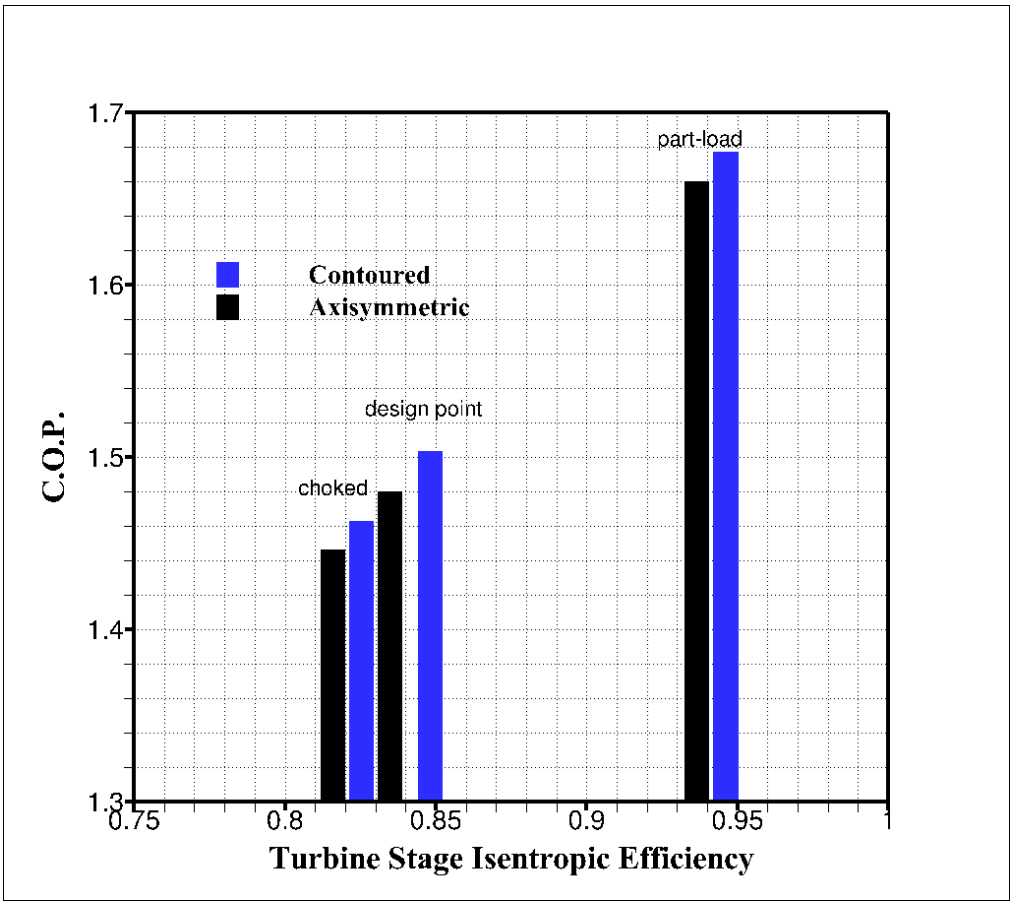

Figure 6-27: Predicted C.O.P. at constant mass flow rate of natural gas fuel with an axisymmetric and a contoured turbine stator hub, at design and off-design.

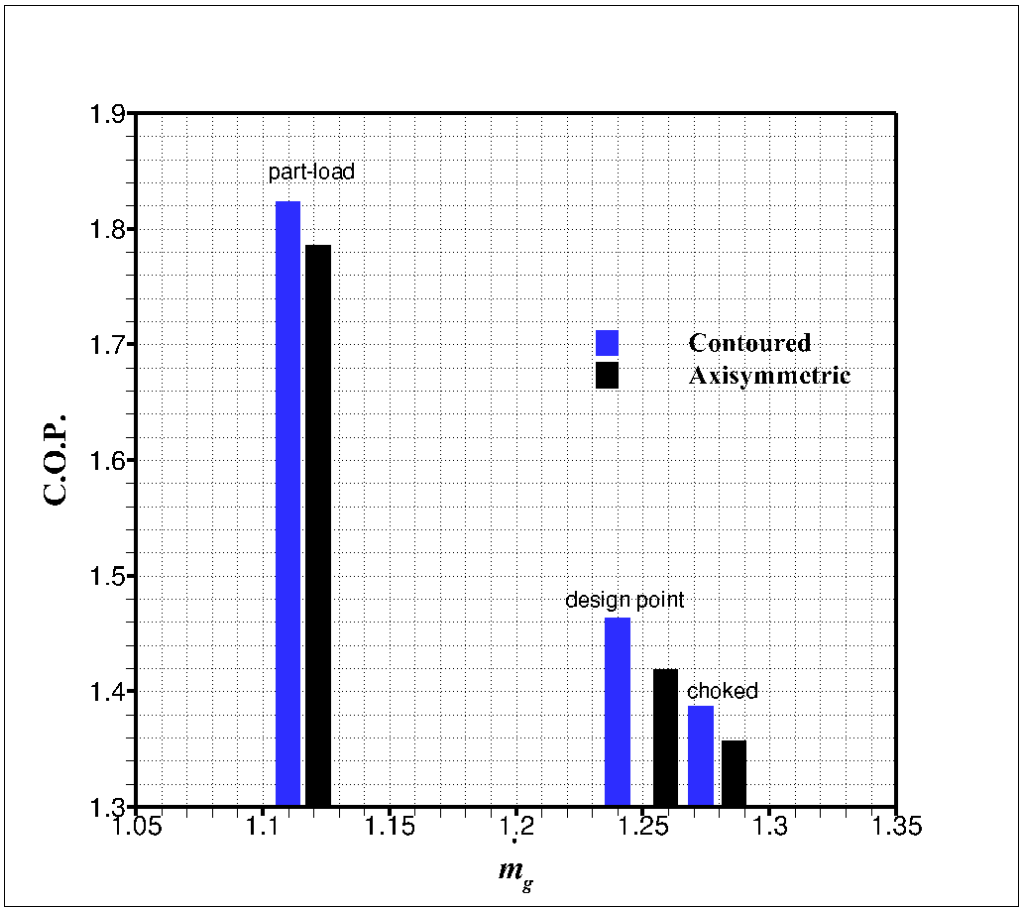

Figure 6-28: Predicted C.O.P. at variable natural gas fuel mass flow rate with an axisymmetric and a contoured turbine stator hub, at design and off-design.

The LNG cycle performance is predicted to improve by improving the stage isentropic efficiency of the axial turbines that drive the axial compressors for the three refrigerants (Propane, Ethylene, and Methane). This improvement reduces the cost of producing liquefied natural gas, based on the cycle inlet conditions of NG at 50 bar inlet pressure and 37 °C inlet temperature, and the cycle outlet conditions of LNG at 2 bar outlet pressure and -162 °C outlet temperature, at which LNG is ready for storage and shipping in cryogenic tanks. A reduction in the cost of liquefaction of natural gas can therefore be obtained by reducing the amount of NG that is burnt in the turbines.

The evaluation of environmental impact of retro-fitting turbines with the optimised contoured hub to the representative LNG cycle are evaluated using the stoichiometric chemistry detailed in Boyce (2011). One kmol of fuel generates 0.0332 kmol of CO_2 according to the following chemical balance:

$$
\begin{aligned}
0.0005\ C_6H_{14} + 0.0004\ C_5H_{12} + 0.0015\ C_4H_{10} + 0.0038\ C_3H_8 \\
+ 0.0287\ C_2H_6 + 0.8129\ CH_4 + 0.0089\ CO_2 + 0.0001\ O_2 \\
+ 0.1432\ N_2 + Y[0.79\ N_2 + 0.21\ O_2] \\
\rightarrow 0.0328\ CO_2 + 0.0724\ H_2O + 0.1364\ O_2 + 0.7496\ N_2
\end{aligned}
\tag{6-3}
$$

The molar weight of NG is 18.5978 kg/kmol and the molar weight of CO_2 44.0 kg/kmol. Therefore, the complete combustion of 1 kg of NG generates 0.078547 kg of CO_2. Giving that the LNG cycle uses 3.777 kg/s of fuel, it emits 0.098891 kg/s of CO_2, equivalent to 3118.613 tonnes of CO_2/year. By reducing the fuel consumption by 1.51 %, the corresponding reduction in CO_2 is 252.212 tonnes of CO_2/year.

This quantifies the direct environmental benefit of using the hub contouring technique in a representative cryogenic application. Further indirect benefits will arise from savings in the processing and transportation costs of the fuel burnt by the turbines as well as savings in the treatment of the exhaust gasses before are released into the atmosphere.

6.7 Summary

The new design of the turbine stator 1 hub from Chapter Five was imported in ANSYS ICEM CFD as an IGES file to replace the axisymmetric turbine stator 1 hub of the validation test case. A CFD mesh was regenerated and exported as an unstructured ANSYS FLUENT mesh. The same boundary conditions, flow solver, and post processing were used as in the validation teat case. A new turbine stator 1 hub design, using a guide curve, was predicted to reduce the stage total pressure loss coefficient. The turbine blade pressure side vortex followed the groove path from the turbine blade leading edge to the groove maximum depth position. The optimisation of the turbine stator 1 hub new design was obtained using three main parameters, the groove width at the stator 1 blade leading edge, d_{le}, the position of the maximum groove depth, h_o, and the groove width at the stator 1 passage trailing edge, d_{te}. Two tasks were used for optimising the groove parameters, using a Kriging surrogate model. The highest reduction in the stage total pressure loss coefficient was obtained at d_{te} = 0.05 rad, h_o = 70 %, and d_{le}= 0.005 rad. An alternative contoured hub surface definition was tested, from the literature, by which the surface was defined by bumps. This was taken as a representative industry best practice. The shape of the bumps was optimised using a Kriging surrogate model, by which the effect on loss of varying the radial heights r_{SS} , r_{PS_1}, r_{PS_2} of three control points that shape bumps was predicted. The highest reduction in the stage total

pressure loss coefficient was obtained at r_{SS} = -3 mm, r_{PS_1} = -3 mm and r_{PS_2} = 1 mm. A comparison between the two contouring techniques was obtained in terms of the stage total pressure loss coefficient, the stage isentropic efficiency, and of distributions of x-vorticity and of the specific turbulent kinetic energy, downstream of the rotor row. Ten off-design conditions highlighted the benefits of the new hub contouring technique. Aerodynamic performance gains from contouring the hub with a guide groove are predicted at all ten conditions. APOW was used to automate this numerical investigation by executing this workflow in batch mode. Cycle-tempo software was used for estimating the impact of the turbine stage re-design on a natural gas liquefaction process, representative of current commercial LNG operations. The reduction in the secondary flow losses of the gas turbines, which are used to drive the LNG refrigeration combined cycle, showed an increase in C.O.P. of the LNG cycle.

7. Conclusions

7.1 Design and Performance of Contoured Axial Turbine Hubs

Various treatments have been considered, by way of a literature review, for mitigating the adverse effects of the three-dimensional flows on the aerodynamic performance and on the operating range of axial turbines. Fences, grooves, suction and blowing slots, fillets, and other end-wall arrangements highlight a variable and open approach. Turbine end-walls have been parameterised using continuous statistical distributions and guide curves to define non-axisymmetric surfaces, by control points to define surface bumps, and using Bezier curves. Bezier curves offer broadly good surface properties in the hub interior but have limitations in smoothly matching the blade geometry along the perimeter. The polymorphism in the end-wall shapes used in past work points towards an opportunity for considering more common geometrical representations, driven by the flow morphology.

A preliminary exploration of the end-wall groove parameter space was reported in Chapters Three and Four. The author has explored the new idea of using the Beta probability density function as a depth guide curve with a novel blade inflation process for designing an original contoured hub. This was found to fit more naturally with the pitchwise periodicity of axial turbine blading than some of the other hub surface definitions from the literature. It provides a potentially easier to implement and geometrically smoother interface with the blading with respect to alternative analytical functions, including the Gauss or normal distribution, which was used in previous work.

This thesis has outlined the novelty and has presented the first application of the Beta probability density function to a three-dimensional axial turbine hub design, using the end-wall surface definition in Obaida et al. (2016). A 1.5 stage axial turbine from RWTH Aachen was used for testing the effectiveness of contouring the upstream stator hub with this new surface definition method. As the free parameters that define the contoured hub surface required tuning, the workflow for generating the geometry, meshing it, applying the boundary conditions, solving the flow, and analyzing the results for pressure loss was successfully automated using the Alstom Process Optimisation Workflow (APOW) software.

An important step in this process was finding a method for exporting a $s(u, v)$ parameterised surface from MATLAB to ANSYS ICEM CFD without loss of topological information or

excessive surface re-approximation. This work highlighted the benefit of using NURBS surfaces in the IGES format for this operation, as NURBS can represent exactly cylindrical and conical surfaces on the hub and casing.

Advances in the design process of axial turbines are achieved in this thesis by the application of OpenFOAM to a multi-row simulation, to demonstrate the effectiveness of the new contoured hub design technique, and by using surrogate modelling in a close-to-industry design workflow for optimising the design. The contoured hub design uses a channelling groove, shaped by parameters d_{te}, h_o, and d_{le} that are optimised using High Performance Computing (HPC) resources typically available in academia.

The positive results from the mesh independence test, the grid convergence test, and from the validation of the pitch-averaged velocity and yaw angle distributions against reference measurements from RWTH Aachen gave confidence in the OpenFOAM predictions and in their use in the design optimisation workflow. The outcome is an end-to-end design process for the contouring of the axial turbine stator hub that uses industry-standard software and has therefore good portability towards the turbomachinery industry.

The CFD predictions confirm the underlying working principle of the end-wall groove that the groove delays the formation of the passage vortex by influencing the path of the upstream horseshoe vortex. This channelling technique for the end-wall flow appeals to different aspects of the flow physics than the more established contoured end-wall design techniques, which mainly aim at mitigating the pitchwise pressure gradient by local accelerations and decelerations of the passage flow. This has provided a novel design angle to end wall contouring.

The preliminary set of end wall geometries gave promising performance improvements at the operating conditions of the RWTH Aachen experiment. Adding a groove of constant width along the groove path line was predicted to decrease the stage total pressure loss coefficient by 0.39 % for a narrow groove and by 0.30 % for a wider groove compared to the axisymmetric hub reference geometry. Tapering axially the groove width provided a better decrease in the stage total pressure loss coefficient of 1.76 %. Setting the position of the maximum groove depth rearwards of the blade mid-chord further decreased the predicted pressure loss coefficient to 2.23 % below the axisymmetric hub reference value.

An automated computer-based optimisation of the contoured grooved hub was implemented using a surrogate model, for computational efficiency. The optimised surface was predicted to reduce the stage total pressure loss coefficient by 2.72 % and increase the stage isentropic efficiency by 1.60 %. This outcome substantiates the effectiveness of this novel contoured hub design workflow.

A second automated computer-based optimisation of the Praisner et al. (2013) and Kim et al. (2016) contoured hub was implemented also using a Kriging surrogate model. The CFD modelled a reduction in the stage total pressure loss coefficient of 5.48 % and an increase in the stage isentropic efficiency of 0.19 % using this type of contoured hub with bumps. The Kriging surrogate surface for this type of contoured hub gave the combination of surface defining parameters that produces these performance gains. The radial height of the control point near the pressure side blade leading edge assumes a value higher than that of the control point at the pressure side mid-chord ($r_{PS_1} > r_{PS_2}$). With this hub surface definition, the horseshoe vortex arm near the pressure side edge joined earlier the horseshoe vortex arm from the suction side of the neighbouring blade, with respect to the hub contoured by a guide groove. This cross-flow leads to the formation of a passage vortex of increased size and magnitude compared to the hub contoured by a guide groove. The stage total pressure loss coefficient for this case was reduced by 3.50 %.

The new hub contouring surface definition with a guide groove introduced by the author has some attractive advantages compared to contouring the hub with bumps, which is representative of the current state of the art in industry. First, hub contouring by a guide groove is predicted to improve the stage isentropic efficiency by 1.60 % compared to a 0.19 % improvement by bumps. The guide groove gave a better stator 1 outflow in terms of reducing the axial vorticity component going through the mixing plane between the stator 1 and the rotor, compared to hub contouring with bumps. In terms of parameterisation, the guide groove technique has three free parameters, while the bump technique requires defining nine control points, leading to a more onerous optimisation task for the latter technique. Finally, in terms of manufacturing, the guide groove technique requires just one further machining process to implement the groove between blades, starting from an axisymmetric hub. It does not require the addition of material, for instance by an additive layer manufacturing process, which is instead required to form the bums, starting from an axisymmetric hub. As such, within limits, the hub contouring with a guide groove can be

retro-fitted to existing blading at a lower re-manufacturing cost. A further reduction in the stage total pressure loss coefficient an improvement in the stage isentropic efficiency was obtained by extending the guide groove widths d_{te}, and d_{le} with constant h_o = 70 %, therefore extending the parameter space boundaries beyond those of Chapter Six. These additional performance gains are detailed in Appendix A.

Performance gains with the stator hub contoured by an optimised guide groove were predicted along the operating line of the Aachen Turbine, starting from 50 % part-load up to choking. Ten off-design conditions highlighted the benefits and drawbacks of this hub contouring technique. Aerodynamic performance gains from contouring are predicted at all ten conditions. This good at design and off-design performance should deliver consistent reductions in fuel consumption and in CO_2 emissions in industrial applications. The author found no evidence of any performance penalty from contouring the hub surface, however the impact of the groove on the structural integrity as well as on the surface heat transfer have yet to be investigated.

The turbine stator hub design process introduced in this work, supported by its automated computer-based optimisation, has the promise for making a significant beneficial impact on the performance of turbo-engines, towards providing a more sustainable energy supply and more efficient air transport operations worldwide.

7.2 Potential for Enhancing the Performance of Industrial Cryogenic Cycles

The new grooved hub design and its automated optimisation workflow was shown by numerical modelling to have the potential for improving axial turbomachines for cryogenic applications, specifically for the production of liquefied natural gas (LNG). A gas turbine is typically used in a LNG cycle as the main drive component for the refrigerant axial compressors. Any reduction in the gas turbine secondary flow losses improves the turbine stage isentropic efficiency. The improvements in the turbine stage efficiency improve the efficacy of the LNG cycle. These improvements were quantified by modelling a representative LNG cycle using CycleTempo software, in which turbines with the hub contoured by the optimised guide groove were used. The higher turbine stage isentropic efficiency was predicted to increase in the C.O.P. of the LNG cycle by 1.03 % at part-load, 1.60 % at design point, and 1.20 % at the choking conditions for the turbines that power the cycle.

The second positive implication on the LNG cycle by using the new grooved turbine stator hub design was the reduction of the gas turbine specific fuel consumption. The predicted C.O.P. showed a reduction in the natural gas burnt in the gas turbine for the same power output. At part-load, design point, and choking conditions, the C.O.P. increased by 2.12 %, 3.15 %, and 2.20 % respectively.

The third positive implication was an expected reduction of the CO_2 emissions from the gas turbine. This makes a positive contribution towards making LNG more environmentally sustainable, by reducing the pollution from the LNG cycle to the atmosphere. The fourth positive implication on LNG cycle and the most important was the reduction in the LNG production cost as the amount of the burnt fuel per LNG output and the gas turbine losses were reduced. The author found no negative implication on the cryogenic LNG cycle by using the new optimised grooved turbine stator hub design.

7.3 Recommendation for Future Work

The new optimised grooved end-wall contouring in this thesis is applied only to the turbine stator 1 hub. A future study could consider the application of this novel non-axisymmetric surface to the turbine stator 1 casing, turbine rotor hub and casing, and turbine stator 2 hub and casing, with a tip leakage flow analysis. This will give a better estimate of the reduction in the stage total pressure loss coefficient and of the improvement in the stage isentropic efficiency in a one and 1.5 stage turbine that this new technique can deliver. A numerical study on the implementation of the guide groove technique to the casing of the Aachen Turbine stator 1 is on-going, by Hakim Kadhim at the University of Leicester. On completion of this study, the new optimised groove surface definition technique will be ready for testing in a low-speed test turbine, such as the test rig available at the University of Durham, so to provide further independent verification on its effectiveness, progressively de-risking this new design approach towards its adoption and use in industry.

The improvements on the LNG cycle in this thesis are implemented by the reduction of the turbine secondary flow losses. Further improvements in the LNG cycle could be obtained by using this new optimised groove hub in the axial flow compressors of the LNG refrigeration cycles. This may reduce the effects of the secondary flow losses and may also extend the stall margin. This reduction in compressor losses would reduce the compressor mechanical work input requirements, as well as the heat rejected from the refrigeration cycle condenser.

The use of the stage total pressure loss coefficient as the driver for the end-wall contouring optimisation was successfully shown in this thesis. Chapter Six has also shown the improvements in both the turbine rotor exit total pressure and in the stage isentropic efficiency at design conditions from this optimisation approach. Other parameters, such as the vorticity in the main passage flow direction and the surface heat transfer rate, might provide further insight into the optimised turbine flow characteristics. This may lead to further adjustments in the current selection of the three parameters that define the guide groove on the hub.

8. REFERENCES

ADEBAYO, D. S. 2012. *Annular flows and their interaction with a cylindrical probe. PhD thesis,* University of Leicester.

ADRIAN, B. & MOSHE, B. 1996. *MATLAB for Engineers,* Pearson Education Limited,United Kingdom.

ALABDULKAREM, A., MORTAZAVI, A., HWANG, Y., RADERMACHER, R. & ROGERS, P. 2011. Optimization of propane pre-cooled mixed refrigerant LNG plant. *Applied Thermal Engineering,* **31**, 1091-1098.

BAGSHAW, D., INGRAM, G., GREGORY-SMITH, D. & STOKES, M. 2005. An experimental study of reverse compound lean in a linear turbine cascade. *Proceedings of the Institution of Mechanical Engineers, Part A: Journal of Power and Energy,* **219**, 443-449.

BAGSHAW, D., INGRAM, G., GREGORY-SMITH, D., STOKES, M. & HARVEY, N. 2008. The design of three-dimensional turbine blades combined with profiled endwalls. *Proceedings of the Institution of Mechanical Engineers, Part A: Journal of Power and Energy,* **222**, 93-102.

BARMPALIAS, K. G. 2011. *Steam turbine aerodynamics and geometry optimization for effective reduction of leakage flow interactions. PhD thesis,* Aristotle University of Thessaloniki, Greece.

BEAUDOIN, M., NILSSON, H., PAGE, M., MAGNAN, R. & JASAK, H. Evaluation of an improved mixing plane interface for OpenFOAM. IOP Conference Series: Earth and Environmental Science. IOP Publishing, 022004.

BEHR, T., PORRECA, L., MOKULYS, T., KALFAS, A. & ABHARI, R. 2006. Multistage aspects and unsteady effects of stator and rotor clocking in an axial turbine with low aspect ratio blading. *Journal of turbomachinery,* **128**, 11-22.

BIESINGER, T. E. 1993. *Secondary flow reduction techniques in linear turbine cascades. PhD thesis,* Durham University.

BLOXHAM, M. J. & BONS, J. P. 2014. A Global Approach to Turbomachinery Flow Control: Passage Vortex Control. *Journal of Turbomachinery,* **136**, 041003.

BOYCE, M. P. 2011. *Gas turbine engineering handbook,* Elsevier,USA.

BUKHOLDIN, Y. S., SUKHOSTAVETS, S. & PETUKHOV, I. 2007. Cryogenic plant for natural gas liquefaction. *Chemical and Petroleum Engineering,* **43**, 212-220.

CANEPA, E., FORMOSA, P., LENGANI, D., SIMONI, D., UBALDI, M. & ZUNINO, P. 2007. Influence of aerodynamic loading on rotor-stator aerodynamic interaction in a two-stage low pressure research turbine. *Journal of Turbomachinery,* **129**, 765-772.

CENGEL, Y. A. & BOLES, M. A. 2002. *Thermodynamics: an engineering approach*, McGraw-Hill Education.

CHALUVADI, V., KALFAS, A. & HODSON, H. 2004. Vortex transport and blade interactions in high pressure turbines. *Journal of Turbomachinery,* **126**, 395-405.

CHEN, D., BO, L., LEI, W., NA, Z., CAO, Z. & HUANG, J. 2012. A Novel Nonaxisymmetric Endwall Contouring for Turbine Cascade Using Automated Optimization. *International Journal of Energy Science,* **2**, 89-93.

CHEN, Y., LI, J., TIAN, C., ZHONG, G., FAN, X. & KONG, X. Experimental and Numerical Investigations on the Aerodynamic Performance of the Three-Stage Turbine With Consideration of the Leakage Flow Effect. ASME Turbo Expo 2016: Turbomachinery Technical Conference and Exposition, Seoul, South Korea, 13-17 June, 2017. American Society of Mechanical Engineers, GT2016-56407.

CORRAL, R. & GISBERT, F. 2008. Profiled End Wall Design Using an Adjoint Navier–Stokes Solver. *Journal of Turbomachinery,* **130**, 021011.

COULL, J. D. 2017. Endwall Loss in Turbine Cascades. *Journal of Turbomachinery,* **139**, 081004-081004-12.

CUI, J. & TUCKER, P. 2016. Numerical Study of Purge and Secondary Flows in a Low-Pressure Turbine. *Journal of Turbomachinery,* **139**, 021007-021007-10.

DENTON, J. & PULLAN, G. A numerical investigation into the sources of endwall loss in axial flow turbines. ASME Turbo Expo 2012: Turbine Technical Conference and Exposition, Copenhagen, Denmark, 11-15 June 2012. American Society of Mechanical Engineers, GT2012-69173.

DENTON, J. & XU, L. 1998. The exploitation of three-dimensional flow in turbomachinery design. *Proceedings of the Institution of Mechanical Engineers, Part C: Journal of Mechanical Engineering Science,* **213**, 125-137.

DENTON, J. D. 1993. The 1993 IGTI scholar lecture: loss mechanisms in turbomachines. *Journal of Turbomachinery,* **115**, 621-656.

DEVORE, J. 2015. *Probability and Statistics for Engineering and the Sciences,* Cengage Learning,Boston, USA.

DORFNER, C., HERGT, A., NICKE, E. & MOENIG, R. 2011. Advanced Nonaxisymmetric Endwall Contouring for Axial Compressors by Generating an Aerodynamic Separator—Part I: Principal Cascade Design and Compressor Application. *Journal of Turbomachinery,* **133**, 021026.

DUNN, D., SNEDDEN, G. & VON BACKSTRÖM, T. Unsteady Effects of a Generic Non-Axisymmetric Rotor Endwall Contour on a 1½ Stage Turbine Test Rig at Off Design Conditions. ASME Turbo Expo 2014: Turbine Technical Conference and Exposition, Dusseldorf, Germany, 16-20 June 2014. American Society of Mechanical Engineers, GT2014-25524.

DUNN, D., SNEDDEN, G. & VON BACKSTRÖM, T. W. Experimental investigation into the unsteady effects on non-axisymmetric turbine endwall contouring. Pretoria, South Africa, 10-13 January 2010. South African Conference on Computational and Applied Mechanics.

DUNN, D. & VON BACKSTRÖM, T. Numerical investigation into the unsteady effects of non-axisymmetric turbine endwall contouring on secondary flows. International Society for Airbreathing Engines, Gothenburg, Sweden, 12-16 September 2011.

FUNAZAKI, K., ENDO, T. & TANUMA, T. Reduction of secondary flow effects in a linear cascade by use of an air suction from the endwall. American Society of Mechanical Engineers New York, USA, 05-07 November 1996. 96-TA-51.

GALLUS, H. E. 1995. ERCOFTAC Test Case 6 Axial Flow Turbine Stage, in: Seminar and Workshop on 3D Turbomachinery flow prediction III, Les Arcs, France.

GALLUS, H. E., ZESCHKY, J., WESKAMP, K. & ZEBNER, H. 1990. Experimental and Numerical Investigations on the Viscous Flow Through an Axial-Flow Turbine Stage. *Interfluid 1st International Congress on Fluid Handling Systems,* **10**, 856-869.

GERMAIN, T., NAGEL, M., RAAB, I., SCHUEPBACH, P., ABHARI, R. & ROSE, M. 2010. Improving Efficiency of a High Work Turbine Using Nonaxisymmetric Endwalls—Part I: Endwall Design and Performance. *Journal of Turbomachinery,* **132**, 021007.

GOLDSTEIN, R. & SPORES, R. 1988. Turbulent transport on the endwall in the region between adjacent turbine blades. *ASME J. Heat Transfer,* **110**, 862-869.

HAN, W., TAN, C., SHI, H., ZHOU, M. & WANG, Z. Effects of leaning and curving of blades with high turning angles on the aerodynamic characteristics of turbine

rectangular cascades. ASME 1993 International Gas Turbine and Aeroengine Congress and Exposition. American Society of Mechanical Engineers, 93-GT-296.

HARRISON, S. The influence of blade lean on turbine losses. ASME 1990 International Gas Turbine and Aeroengine Congress and Exposition. American Society of Mechanical Engineers, 90-GT-55.

HARTLAND, J., GREGORY-SMITH, D. & ROSE, M. Non-axisymmetric endwall profiling in a turbine rotor blade. ASME 1998 International Gas Turbine and Aeroengine Congress and Exhibition, New York, USA, 02-05 June 1998. American Society of Mechanical Engineers, 98-GT-525.

HARVEY, N., BRENNAN, G., NEWMAN, D. & ROSE, M. Improving turbine efficiency using non-axisymmetric end walls: Validation in the multi-row environment and with low aspect ratio blading. ASME Turbo Expo 2002: Power for Land, Sea, and Air, Amsterdam, the Netherlands, 03-06 June 2002. American Society of Mechanical Engineers, GT-2002-30337.

HARVEY, N. W., ROSE, M. G., TAYLOR, M. D., SHAHPAR, S., HARTLAND, J. & GREGORY-SMITH, D. G. Non-Axisymmetric Turbine End Wall Design: Part I—Three-Dimensional Linear Design System. ASME 1999 International Gas Turbine and Aeroengine Congress and Exhibition, Indiana, USA, 07-10 June 1999. American Society of Mechanical Engineers, 99-GT-337.

HECKLAU, M., GMELIN, C., NITSCHE, W., THIELE, F., HUPPERTZ, A. & SWOBODA, M. 2011. Experimental and numerical results of active flow control on a highly loaded stator cascade. *Proceedings of the Institution of Mechanical Engineers, Part A: Journal of Power and Energy*, **225**, 907-918.

HEINICHEN, F., GÜMMER, V., PLAS, A. & SCHIFFER, H. P. 2011. Numerical investigation of the influence of non-axisymmetric hub contouring on the performance of a shrouded axial compressor stator. *CEAS Aeronautical Journal*, **2**, 89-98.

HERGT, A., DORFNER, C., STEINERT, W., NICKE, E. & SCHREIBER, H.-A. 2011. Advanced Nonaxisymmetric Endwall Contouring for Axial Compressors by Generating an Aerodynamic Separator—Part II: Experimental and Numerical Cascade Investigation. *Journal of Turbomachinery*, **133**, 021027.

HODSON, H. & DAWES, W. On the interpretation of measured profile losses in unsteady wake-turbine blade interaction studies. ASME 1996 International Gas Turbine and

Aeroengine Congress and Exhibition, Birmingham, UK, 10-13 June 1996. American Society of Mechanical Engineers, 96-GT-494.

HU, S. & LUO, H. Endwall Contouring Optimization in a High Pressure Turbine Vane with Consideration of Rim Seal Flow. ASME Turbo Expo 2014: Turbine Technical Conference and Exposition, Dusseldorf, Germany, 16-20 June 2014. American Society of Mechanical Engineers, GT2014-26587.

HUANG, A. C., GREITZER, E. M., TAN, C. S., CLEMENS, E. F., GEGG, S. G. & TURNER, E. R. 2013. Blade Loading Effects on Axial Turbine Tip Leakage Vortex Dynamics and Loss. *Journal of Turbomachinery,* **135**, 051012.

INGRAM, G. L. 2003. *Endwall profiling for the reduction of secondary flow in turbines. PhD thesis*, University of Durham.

INOZEMTSEV, A. A., SAMOKHVALOV, N. Y. & TIKHONOV, A. S. 2012. Achieving more efficient operation of the nozzle vane and rotor blade rows of gas turbines through using nonaxisymmetric end wall surfaces of interblade channels. *Thermal Engineering,* **59**, 667-673.

JASAK, H. & BEAUDOIN, M. OpenFOAM turbo tools: From general purpose CFD to turbomachinery simulations. ASME-JSME-KSME 2011 Joint Fluids Engineering Conference, Hamamatsu, Shizuoka, JAPAN, 24-29 July 2011. American Society of Mechanical Engineers, 1801-1812.

KACHEL, C. E. & DENTON, J. D. 2006. Experimental and Numerical Investigation of the Unsteady Surface Pressure in a Three-Stage Model of an Axial High Pressure Turbine. *Journal of turbomachinery,* **128**, 261-272.

KADHIM, H. T., RONA, A., OBAIDA, H. M. & GOSTELOW, J. P. Numerical Study of the Flow past an Axial Turbine Stator Casing and Perspectives for Its Management. ASME Turbo Expo 2017: Turbomachinery Technical Conference and Exposition, Charlot, NC, USA, 26-30 June 2017. American Society of Mechanical Engineers, GT2017-63055.

KAWAI, T., SHINOKI, S. & ADACHI, T. 1989. Secondary flow control and loss reduction in a turbine cascade using endwall fences. *JSME international journal. Ser. 2, Fluids engineering, heat transfer, power, combustion, thermophysical properties,* **32**, 375-387.

KAWAI, T., SHINOKI, S. & ADACHI, T. 1990. Visualization study of three-dimensional flows in a turbine cascade endwall region. *JSME international journal. Ser. 2,*

Fluids engineering, heat transfer, power, combustion, thermophysical properties, **33**, 256-264.

KIM, I., KIM, J., CHO, J. & KANG, Y.-S. Non-Axisymmetric Endwall Profile Optimization of a High-Pressure Transonic Turbine Using Approximation Model. ASME Turbo Expo 2016: Turbomachinery Technical Conference and Exposition, Seoul, South Korea, 13-17 June 2016. American Society of Mechanical Engineers, GT2016-57970.

KLUXEN, R., BEHRE, S., JESCHKE, P. & GUENDOGDU, Y. 2017. Loss Mechanisms of Interplatform Steps in a 1.5-Stage Axial Flow Turbine. *Journal of Turbomachinery,* **139**, 031007.

LAMPART, P., GARDZILEWICZ, A., RUSANOV, A. & YERSHOV, S. 1999. The Effect of Stator Blade Compound Lean and Compound Twist on Flow Characteristics of a Turbine Stage: Numerical Study Based on 3D NS Simulations. *ASME-PUBLICATIONS-PVP,* **397**, 195-204.

LANGSTON, L. 2001. Secondary flows in axial turbines—a review. *Annals of the New York Academy of Sciences,* **934**, 11-26.

LI, D., CHEN, H., SONG, Y. & CUI, K. Numerical Investigation of the Non-Axisymmetric End Wall Application to the White Cascade. ASME Turbo Expo 2015: Turbine Technical Conference and Exposition, Montreal, Canada, 15-19 June 2015. American Society of Mechanical Engineers, GT2015-42261.

LIN, C., CHIU, P.-H. & SHIEH, S.-J. 2002. Characteristics of horseshoe vortex system near a vertical plate–base plate juncture. *Experimental Thermal and Fluid Science,* **27**, 25-46.

LIN, W., ZHANG, N. & GU, A. 2010. LNG (liquefied natural gas): A necessary part in China's future energy infrastructure. *Energy,* **35**, 4383-4391.

LUO, J., MCBEAN, I. & LIU, F. Optimization of endwall contours of a turbine blade row using an adjoint method. ASME 2011 Turbo Expo: Turbine Technical Conference and Exposition, Vancouver,British Columbia, Canada, 06-10 June 2011. American Society of Mechanical Engineers, 1335-1350.

LUO, J., XIONG, J., LIU, F. & MCBEAN, I. 2011b. Three-dimensional aerodynamic design optimization of a turbine blade by using an adjoint method. *Journal of Turbomachinery,* **133**, 011026.

LYNCH, S. P., SUNDARAM, N., THOLE, K. A., KOHLI, A. & LEHANE, C. 2011. Heat transfer for a turbine blade with nonaxisymmetric endwall contouring. *Journal of Turbomachinery,* **133**, 011019.

LYNCH, S. P. & THOLE, K. A. 2016. Comparison of the three-dimensional boundary layer on flat versus contoured turbine endwalls. *Journal of Turbomachinery,* **138**, 041008.

MA, H., JIANG, H. & QIU, Y. Visualizations of the unsteady flow field near the endwall of a turbine cascade. ASME Turbo Expo 2002: Power for Land, Sea, and Air, Amsterdam, The Netherlands, 03-06 June 2002. American Society of Mechanical Engineers, 233-240.

MA, Z. 2011. *Non-Gaussian statistical models and their applications. PhD thesis,* Diss. KTH Royal Institute of Technology.

MAFI, M., GHORBANI, B., SALEHI, G., AMIDPOUR, M. & NAYENIAN, S. M. 2014. The Mathematical Method and Thermodynamic Approaches to Design Multi-Component Refrigeration used in Cryogenic Process Part II: Optimal Arrangement. *Gas Process Journal* **1**, 21-30.

MATSUNUMA, T. 2007. Unsteady flow field of an axial-flow turbine rotor at a low Reynolds number. *Journal of turbomachinery,* **129**, 360-371.

MEHER-HOMJI, C., MESSERSMITH, D., HATTENBACH, T., ROCKWELL, J., WEYERMANN, H. & MASANI, K. Aeroderivative Gas Turbines for LNG Liquefaction Plants: Part 1—The Importance of Thermal Efficiency. ASME Turbo Expo 2008: Power for Land, Sea, and Air, Berlin, Germany, 09-13 June 2008. American Society of Mechanical Engineers, GT 2008-50839.

MENSCH, A. & THOLE, K. A. 2016. Overall effectiveness and flowfield measurements for an endwall with nonaxisymmetric contouring. *Journal of Turbomachinery,* **138**, 031007.

MOKHATAB, S., MAK, J. Y., VALAPPIL, J. V. & WOOD, D. A. 2013. *Handbook of liquefied natural gas,* Gulf Professional Publishing,Oxford, UK.

MOKHATAB, S. & WOOD, D. 2007. Breaking the offshore LNG stalemate. *World oil,* **228**, 139.

MOON, Y. J. & KOH, S.-R. 2001. Counter-rotating streamwise vortex formation in the turbine cascade with endwall fence. *Computers & fluids,* **30**, 473-490.

MORAES, A. D. O. S., DA CUNHA LAGE, P. L., CUNHA, G. C. & DA SILVA, L. F. L. R. Analysis of the non-orthogonality correction of finite volume discretization on

unstructured meshes. 22nd International Congress of Mechanical Engi-neering. Ribeir~ to Preto, SP. 3518-3530.

NAGEL, M. G. & BAIER, R.-D. 2005. Experimentally verified numerical optimization of a three-dimensional parametrized turbine vane with nonaxisymmetric end walls. *Journal of Turbomachinery,* **127**, 380-387.

NERGER, D., SAATHOFF, H., RADESPIEL, R., GÜMMER, V. & CLEMEN, C. 2012. Experimental investigation of endwall and suction side blowing in a highly loaded compressor stator cascade. *Journal of Turbomachinery,* **134**, 021010.

NICE, M. & HOOPER, R. 1977. Three-dimensional flow within a turbine cascade passage. *Journal of Engineering for Power,* **99(1)**, 21-28.

OBAIDA, H. M., KADHIM, H. T., RONA, A., LESCHKE, K. & GOSTELOW, J. P. Numerical Study of Secondary Flows in a 1.5 Stage Axial Turbine Guiding the Design of Non-Axisymmetric Hub. ASME Turbo Expo 2017: Turbomachinery Technical Conference and Exposition, Charlotte, NC, USA, 26-30 June 2017. American Society of Mechanical Engineers, ASME Paper GT2017-65251.

OBAIDA, H. M., KAWASE, M., RONA, A. & GOSTELOW, J. P. Some Perspectives on the Treatment of Three-Dimensional Flows on Axial Compressor Blading. ASME Turbo Expo 2016: Turbomachinery Technical Conference and Exposition, Seoul, South Korea, 13-17 June 2016. American Society of Mechanical Engineers, ASME Paper GT2016-57617.

PALMER, T. R., TAN, C. S., ZUNIGA, H., LITTLE, D., MONTGOMERY, M. & MALANDRA, A. 2016. Quantifying Loss Mechanisms in Turbine Tip Shroud Cavity Flows. *Journal of Turbomachinery,* **138**, 091006-091006-10.

PANIAGUA, G., DÉNOS, R. & ALMEIDA, S. 2004. Effect of the Hub Endwall Cavity Flow on the Flow-Field of a Transonic High-Pressure Turbine. *Journal of Turbomachinery,* **126**, 578-586.

PETER, S. 2009. *Influence of rim seal purge flow on the performance of an end wall profiled axial turbine. PhD thesis*, ETH, Zürich.

PHILIPP, J. 2012. *Interaction mechanisms between rim seal purge flow and profiled end walls in a low-pressure turbine. PhD thesis*, ETH, Zürich.

PIEGL, L. & TILLER, W. 1997. *The NURBS book. 1997,* Springer-Verlag Berlin Heidelberg GmbH,Berlin, Germany.

PIEGL, L. & TILLER, W. 2012. *The NURBS book,* Springer Science & Business Media,Berlin, Germany.

POLYNKIN, A., TOROPOV, V. & SHAHPAR, S. Multidisciplinary Optimization of Turbomachinery based on metamodel built by Genetic Programming. Proceedings of the 13th AIAA/ISMO Multidisciplinary Analysis and Optimization Conference, Fort Worth, TX, 13-15 September AIAA 2010-9397.

PRAISNER, T., ALLEN-BRADLEY, E., GROVER, E., KNEZEVICI, D. & SJOLANDER, S. 2013. Application of nonaxisymmetric endwall contouring to conventional and high-lift turbine airfoils. *Journal of Turbomachinery,* **135**, 061006.

PRAISNER, T. & SMITH, C. 2006a. The Dynamics of the Horseshoe Vortex and Associated Endwall Heat Transfer—Part I: Temporal Behavior. *Journal of Turbomachinery,* **128**, 747-754.

PRAISNER, T. & SMITH, C. 2006b. The dynamics of the horseshoe vortex and associated endwall heat transfer—part II: time-mean results. *Journal of Turbomachinery,* **128**, 755-762.

REMELJEJ, C. & HOADLEY, A. 2006. An exergy analysis of small-scale liquefied natural gas (LNG) liquefaction processes. *Energy,* **31**, 2005-2019.

REUTTER, O., HEMMERT-POTTMANN, S., HERGT, A. & NICKE, E. Endwall Contouring and Fillet Design for Reducing Losses and Homogenizing the Outflow of a Compressor Cascade. ASME Turbo Expo 2014: Turbine Technical Conference and Exposition, Dusseldorf, Germany, 16-20 June 2014. American Society of Mechanical Engineers, GT2014-25277.

REUTTER, O., HERVÉ, S. & NICKE, E. 2009. Automated Optimazation of the Non-Axisymmetric Hub Endwall of the Rotor of an Axial Compressor. *10th European Conference on Turbomachinery* pp. 1-11.

REZASOLTANI, M., SCHOBEIRI, M. & HAN, J. 2014. Experimental Investigation of the Effect of Purge Flow on Film Cooling Effectiveness on a Rotating Turbine With Nonaxisymmetric End Wall Contouring. *Journal of Turbomachinery,* **136**, 091009.

RONA, A., PACIORRI, R. & GERON, M. 2006. Design and testing of a transonic linear cascade tunnel with optimized slotted walls. *Journal of Turbomachinery,* **128**, 23-34.

ROQUE, C. & FERNANDO, G. 2005. Non Axisymmetric End-Wall Design Using an Adjoint Navier-Stokes Solver. *AIAA Paper,* **4025**, 1-17.

ROSE, M., FOMISON, N. & TAYLOR, M. 2003. Improving the efficiency of the trent 500-hp turbine using nonaxisymmetric end walls—part i: Turbine design.

ROSE, M., HARVEY, N., SEAMAN, P., NEWMAN, D. & MCMANUS, D. Improving the Efficiency of the Trent 500 HP Turbine Using Non-Axisymmetric End Walls: Part II—Experimental Validation. ASME Turbo Expo 2001: Power for Land, Sea, and Air, New Orleans, Louisiana, USA, 04-07 June 2001. American Society of Mechanical Engineers, 2001-GT-0505.

ROSE, M. G. Non-axisymmetric endwall profiling in the HP NGV's of an axial flow gas turbine. ASME 1994 International Gas Turbine and Aeroengine Congress and Exposition, The Hague, Netherlands, 13-16 June 1994. American Society of Mechanical Engineers, 94-GT-249.

ROSE, M. G. & HARVEY, N. W. Turbomachinery wakes: Differential work and mixing losses. ASME 1999 International Gas Turbine and Aeroengine Congress and Exhibition, Indianapofis, Indiana, 07-10 June 1999. American Society of Mechanical Engineers, 99-GT-25.

SANGSTON, K., LITTLE, J., ERIC LYALL, M. & SONDERGAARD, R. 2016. Effect of Blade Profile Contouring on Endwall Flow Structure in a High-Lift Low-Pressure Turbine Cascade. *Journal of Turbomachinery*, **139**, 021006-021006-11.

SCHIEGEL, J., LIU, H. & WATERMAN, W. 1976. Reduction of End-Wall Effects in a Small, Low-Aspect-Ratio Turbine by Radial Work Redistribution. *Journal of Engineering for Power,* **98**, 130-136.

SCHOBEIRI, M. & LU, K. 2014. Endwall contouring using continuous diffusion: a new method and its application to a three-stage high pressure turbine. *Journal of Turbomachinery,* **136**, 011006.

SCHUEPBACH, P., ABHARI, R., ROSE, M., GERMAIN, T., RAAB, I. & GIER, J. 2010. Improving Efficiency of a High Work Turbine Using Nonaxisymmetric Endwalls—Part II: Time-Resolved Flow Physics. *Journal of Turbomachinery,* **132**, 021008.

SCHWAB, S., WENDLAND, D. & WIRSUM, M. Numerical and Experimental Investigation of Tangential Endwall Contoured Blades in a 2-Stage Turbine. ASME Turbo Expo 2013: Turbine Technical Conference and Exposition, San Antonio, Texas, USA, 03-07 June 2013. American Society of Mechanical Engineers, GT2013-94169.

SHAHPAR, S., CALONI, S. & DE PRIEÃGLLE, L. 2017. Automatic Design Optimization of Profiled Endwalls including Real Geometrical Effects to Minimize Turbine Secondary Flows. *Journal of Turbomachinery,* **139**, 071010.

SHARMA, O. & BUTLER, T. Predictions of endwall losses and secondary flows in axial flow turbine cascades. ASME 1986 International Gas Turbine Conference and Exhibit, Dusseldorf, West Germany, 08-12 June 1986. American Society of Mechanical Engineers, 86-GT-228.

SIEVERDING, C. Recent progress in the understanding of basic aspects of secondary flows in turbine blade passages. American Society of Mechanical Engineers, International Gas Turbine Conference and Exhibit, 29th, Amsterdam, Netherlands.

SNEDDEN, G., DUNN, D., INGRAM, G. & GREGORY-SMITH, D. The application of non-axisymmetric endwall contouring in a single stage, rotating turbine. ASME Turbo Expo 2009: Power for Land, Sea, and Air, Orlando, Florida, USA, 08-12 June 2009. American Society of Mechanical Engineers, GT2009-59169.

SNEDDEN, G. C. 2011. *The application of non-axisymmetric end wall contouring in a 1 stage, rotating turbine. PhD thesis*, Durham University.

SUN, H., LI, J., SONG, L. & FENG, Z. Non-Axisymmetric Turbine Endwall Aerodynamic Optimization Design: Part I—Turbine Cascade Design and Experimental Validations. ASME Turbo Expo 2014: Turbine Technical Conference and Exposition, Dusseldorf, Germany, 16-20 June 2014. American Society of Mechanical Engineers, GT2014-25362.

SUN, H., SONG, L., LI, J. & FENG, Z. Non-Axisymmetric Turbine Endwall Aerodynamic Optimization Design: Part II—Turbine Stage Design and Unsteady Flow Characteristics Analysis. ASME Turbo Expo 2014: Turbine Technical Conference and Exposition, Dusseldorf, Germany, 16-20 June 2014. American Society of Mechanical Engineers, GT2014-25364.

TAHER, M. & MEHER-HOMJI, C. B. Cryogenic Turboexpanders in LNG Liquefaction Applications. ASME Turbo Expo 2016: Turbomachinery Technical Conference and Exposition, Seoul, South Korea, 13-17 June 2016. American Society of Mechanical Engineers, GT2016-57020.

TALNIKAR, C., WANG, Q. & LASKOWSKI, G. M. 2016. Unsteady Adjoint of Pressure Loss for a Fundamental Transonic Turbine Vane. *Journal of Turbomachinery,* **139**, 031001-031001-10.

TANG, H., LIU, S. & LUO, H. Design Optimization of Profiled Endwall With Consideration of Cooling and Rim Seal Flow Effects. ASME Turbo Expo 2016: Turbomachinery Technical Conference and Exposition, Seoul, South Korea, 13-17 June 2016. American Society of Mechanical Engineers, GT2016-57219.

TAREMI, F., SJOLANDER, S. A. & PRAISNER, T. J. 2013. Application of endwall contouring to transonic turbine cascades: Experimental Measurements at design conditions. *Journal of Turbomachinery*, **135**, 011031.

TURGUT, O. H. & CAMCı, C. A Nonaxisymmetric Endwall Design Methodology for Turbine Nozzle Guide Vanes and Its Computational Fluid Dynamics Evaluation. ASME 2011 International Mechanical Engineering Congress and Exposition, Denver, Colorado, USA, 11-17 November 2011. American Society of Mechanical Engineers, IMECE2011-64362.

TURGUT, Ö. H. & CAMCI, C. 2015. A nonaxisymmetric endwall design approach and its computational assessment in the NGV of an HP turbine stage. *Aerospace Science and Technology*, **47**, 456-466.

TURGUT, Ö. H. & CAMCI, C. 2016. Factors Influencing Computational Predictability of Aerodynamic Losses in a Turbine Nozzle Guide Vane Flow. *Journal of Fluids Engineering*, **138**, 051103.

VOLMAR, T., BROUILLET, B., BENETSCHIK, H. & GALLUS, H. E. 1998. Test Case 6: 1-1/2 Stage Axial Flow Turbine - Unsteady Computation, in: ERCOFTAC Turbomachinery Seminar and Workshop.

WALRAEVENS, R. & GALLUS, H. European Research Community On Flow Turbulence And Combustion. ERCOFTAC SIG on 3D Turbomachinery Flow Prediction. Testcase 6-1-1/2 Stage axial flow turbine. ERCOFTAC-APPACET Seminar and Workshop on Turbomachinery Flow Prediction VIII.

WALRAEVENS, R. & GALLUS, H. E. 1997. Testcase 6: 1-1/2 Stage Axial Flow Turbine. ERCOFTAC Testcase 6. IST-Report, Aachen University, 1997.

WANG, S.-S., SUN, H., DI, J., MAO, J.-R., LI, J. & CAI, L.-X. 2014. High-resolution measurement and analysis of the transient secondary flow field in a turbine cascade. *Proceedings of the Institution of Mechanical Engineers, Part A: Journal of Power and Energy*, **228**, 799-812.

WATANABE, H. & HARADA, H. 1999. Suppression of secondary flows in a turbine nozzle with controlled stacking shape and exit circulation by 3d inverse design method. *tc*, **1**, 1.

YOON, S., VANDEPUTTE, T., MISTRY, H., ONG, J. & STEIN, A. 2016. Loss Audit of a Turbine Stage. *Journal of Turbomachinery,* **138**, 051004-051004-9.

ZANGENEH, M. 1991. A compressible three-dimensional design method for radial and mixed flow turbomachinery blades. *International Journal for Numerical Methods in Fluids,* **13**, 599-624.

ZHONGQI, W., WANJIN, H. & WENYUAN, X. 1991. The effect of blade curving on flow characteristics in rectangular turbine stator cascades with different incidences. *ASME paper,* 60.

ZIMMERMANN, T. W., CURKOVIC, O., WIRSUM, M., FOWLER, A. & PATEL, K. 2017. Comparison of Two-Dimensional and Three-Dimensional Turbine Airfoils in Combination With Nonaxisymmetric Endwall Contouring. *Journal of Turbomachinery,* **139**, 061007.

APPENDIX A

A.1 Optimised Hub with Extended Groove Width

Further improvements in both the stage total pressure loss coefficient and in the stage isentropic efficiency were achieved. This was done by extending the groove width d_{le} over the range 0.02-0.025 rad, and d_{te} over the range 0.06-0.065 rad. The maximum groove depth position as fraction of groove length h_o was kept at the constant value of 70 %. The Kriging surrogate model was generated and the new optimal guided groove parameters were obtained with a relative difference $\psi = 5.03 \times 10^{-4}$. The OpenFOAM post processing showed a reduction in the $C_p\ loss$ by 3.38 % at d_{le} = 0.024 rad, d_{te} = 0.0638 rad, and h_o = 70 %. The η_{is} was improved by 2.50 % from using this new set of guide groove parameters. This is confirmed in Figure A-1.

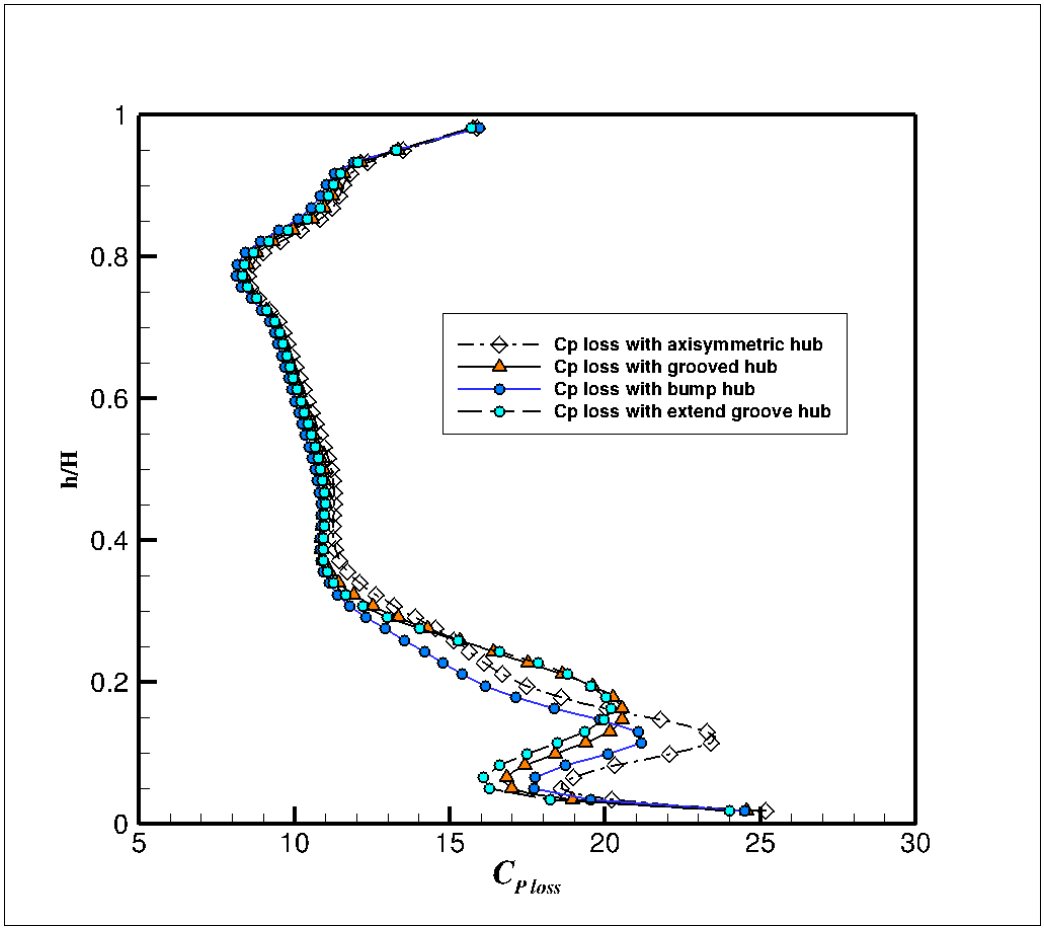

Figure A-1: Radial distribution of mass-averaged total pressure loss coefficient at 8.8 mm behind the rotor blade row, with an axisymmetric and a contoured upstream stator hub.

Figure A-1 shows the radial distribution of the mass-averaged stage total pressure loss coefficient at 8.8 mm downstream of the rotor exit flow. Contouring the hub by the extended guide groove reduced the stage total pressure loss coefficient over the blade span range $0.018 \leq h/H \leq 0.14$, close to the hub region.

Figure A-2 and Figure A-3 show the iso-levels of the predicted vorticity Ω_x and of the predicted turbulent kinetic energy k at 8.8 mm downstream of the rotor flow exit. The passage vortex reduced its size and magnitude, from which a reduction is expected in the in-plane vortex strength going through the mixing plane between stator and rotor. This is clearly shown in Figure A-2 over the blade radius $0.248 \leq r \leq 0.256$ as compared with the results in Chapter six. Figure A-3 shows the same positive outcome as the turbulent kinetic energy k near the rotor hub with the extended groove geometry is less than that from the optimised bump technique, due to the reduction of the in-plane vortex strength going through the mixing plane.

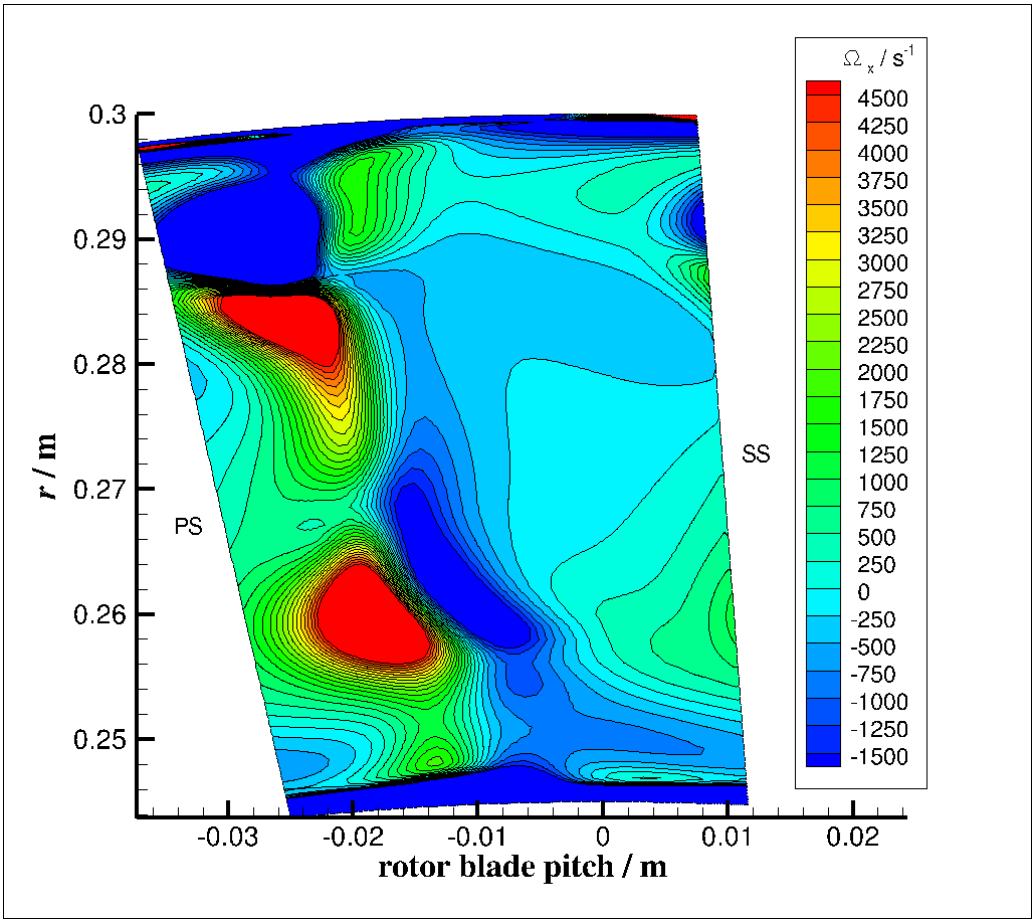

Figure A-2: Colour iso-levels of x-vorticity component predicted with contoured hub by the extended guide groove, 8.8 mm downstream of the rotor exit.

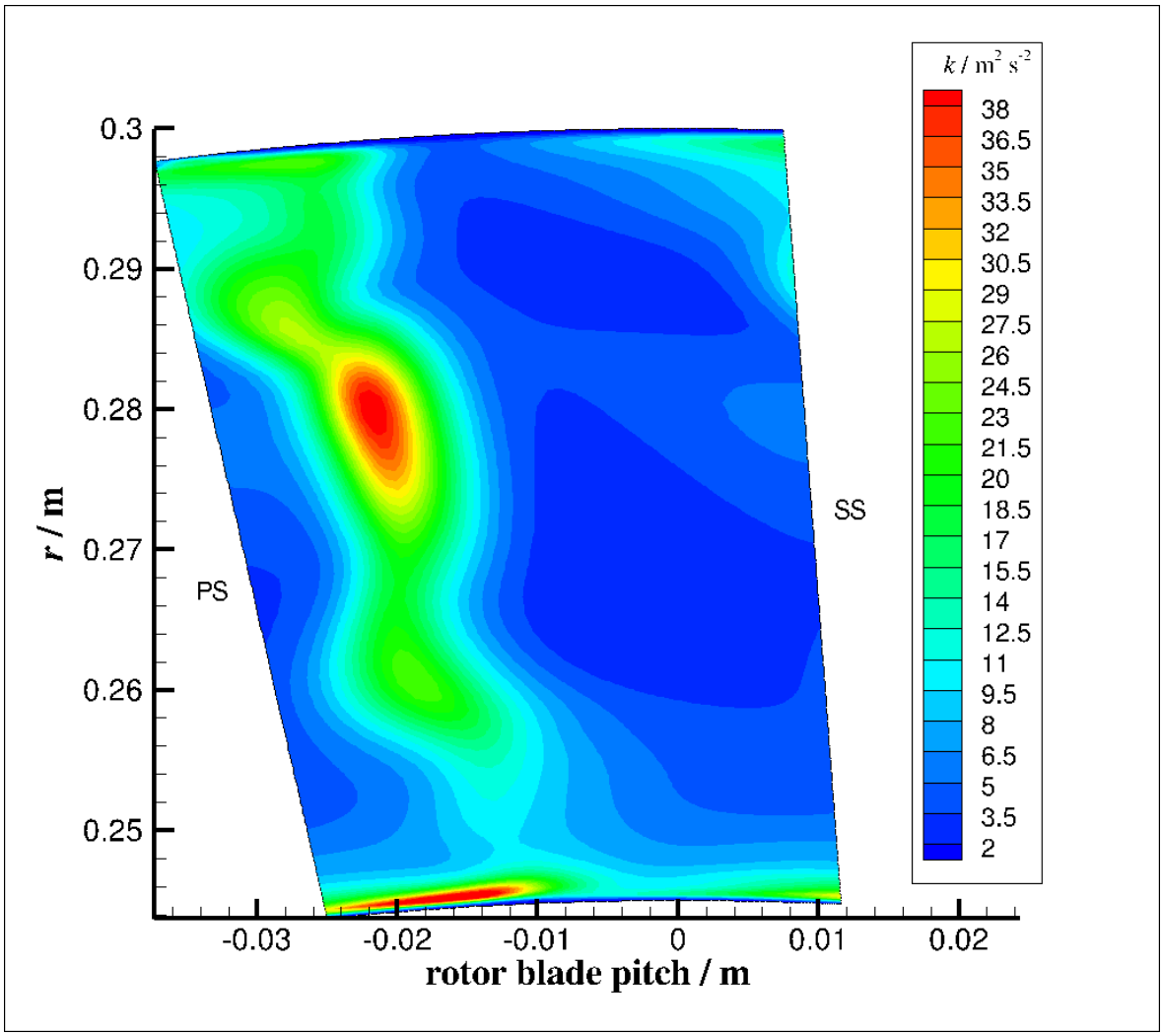

Figure A-3: Iso-levels of specific turbulent kinetic energy predicted with contoured hub by the extended guide groove, 8.8 mm downstream of the rotor exit.